**Doctoral Dissertation**

# Advanced study of coastal acoustic tomography with a focus on data assimilation

(データ同化法に注目した沿岸音響トモグラフィーの先進的研究)

March 2018

Graduate School of Engineering

Hiroshima University

陳 敏模

Contents

# CHAPTER I INTRODUCTION

## 1.1 Variable Environments in Coastal Seas

Coastal seas are transition zones between the continents and open ocean and characterized by variable dynamic phenomena which vary with time, such as coastal upwelling, tide and so on. Coastal seas are sometimes surrounded by lands and islands, forming estuaries and inland seas. About 40% of the world's population lives within 100 kilometers from coast. In coastal seas, environmental variations strongly interact with people's lives. Thus, coastal seas also face societal problems such as sea water pollution, red-tide, coastal erosion and loss of biodiversity. Similarly, sudden environmental changes in coastal seas can also cause significant damages to human activities, especially to ship traffic and marine farming. It is really an essential issue to monitor the present status of environments and predict the future environmental changes occurring in coastal seas to provide basic information for protecting coastal environments and human benefit. However, systemic monitoring of coastal environments is so difficult owing to heavy fisheries activity and shipping traffic. Conventional mooring arrays are difficult to distribute over a wide range without disturbing fisheries activity and shipping traffic. Shipboard ADCP surveys are also difficult to obtain simultaneous snap shots of varying environments. Although high frequency (HF) ocean radars are applicable to deploy in coastal seas facing open ocean, it can get surface information of current alone.

Thus, coastal acoustic tomography (CAT) is proposed as an innovative technology to

enable the mapping of coastal-sea environments, using sound transmission from acoustic stations, arrayed at the periphery of observation domain. Structural mapping and long-term monitoring of varying environments are realized from acoustic stations placed outside fishing grounds and ship traffic routes.

## 1.2 Coastal Acoustic Tomography and Data Assimilation

Ocean acoustic tomography (OAT) was first proposed as a key technology to map the 3D mesoscale structure of temperature and current by using a long-range underwater sound transmission [Munk and Wunsch, 1979; Munk et al., 1995]. The tomography can make a snapshot of current and temperature over the observation domain because of the rapid spatial coverage by sound propagating from station to station. The first experiment was performed by the US OAT Group to measure mesoscale eddies from travel times among six source-receiver arrays [Ocean Tomography Group, 1982]. The eddy fields which were reconstructed by the inverse analysis of one-way travel time data were validated by the shipborne and airborne CTD/XBT/AXBT surveys. The early data demonstrated the feasibility of sound transmission to map temperature structures, using the integrating nature of sound transmission. Since then, a number of experiments were carried out to monitor ocean environments. The deep convection [Worcester, et al, 1993], shallow-bay internal scattering [Apel, et al., 1997] and ocean tide [Dushaw, et al., 2011; Stammer, et al. 2014] were also measured by the OAT.

Sound is able to propagate hundreds of kilometers in open seas. In contrast with open seas of thousand-meter depths, sound transmission processes in coastal seas are much complicated, cause by complex shorelines, high-level ambient noises and reflection and scattering of sound waves at the sea surface and seafloor. The first application of OTA to coastal ocean was performed by Chester et al. [1991] to measure the path-average current velocities in Florida Straits. Long-term, continuous effort has been made by Hiroshima University acoustic tomography group to develop a cost-effective coastal acoustic tomography (CAT) system since 1993. The CAT system, which is a coastal-sea application of OAT, is characterized with high-frequency acoustic signals of range 800 Hz-50 kHz in contrast to 100-800Hz of OAT. CAT system provides an intelligent way to monitor coastal environments inside an observation domain, surrounding it by multi-acoustic stations. The moored or land-based CAT systems were successfully applied to the measurement of current and temperature structures in the coastal and inland seas. The ocean states derived from CAT were also well validated by comparison with CTD and ADCP data.

Pioneering contributions for CAT development were done by Hiroshima University Group. In 1995, the first reciprocal sound transmission experiment was performed between two acoustic stations in the Nekoseto Strait of the Seto-Inland Sea. In comparison with the ADCP data, the feasibility of current measurement by the CAT was well validated [Zheng et al., 1997a; Zheng, 1997b; Zheng et al., 1998]. On the basis of reciprocal sound transmission method, several CAT systems were successfully deployed

in coastal seas around Japan and China [Park and Kaneko, 2001; Yamaoka et al., 2002; Yamaguchi et al., 2005; Zhu, et al., 2012; Zhu, et al., 2013; Zhang et al., 2015; Chen et al., 2017]. By using the multi-station travel time data, the complicated fields of coastal current were reconstructed by the inverse method with the boundary condition of flow. The results showed that the CAT is an accurate and efficient observational method for continuously mapping tidal current structures in the coastal seas.

Intensive effort was devoted to horizontal-slice inversion from CAT data because of difficulty identifying multi-arrival sound rays that turn at different depths. Vertical-slice measurement of currents from CAT still remains as a challenge until multi-arrival rays were obtained. A CAT experiment with an aim of long-term measurement of Kuroshio Current was conducted during May to September 2008 in the Luzon Strait [Taniguchi et al., 2010]. Three kinds of ray group which travel at different depths were obtained and used to reconstruct the vertical profiles of path-average current. Vertical slice of current was also achieved in the CAT experiment of southeast of Taiwan in 2009 [Taniguchi et al., 2013; Taniguchi and Huang, 2014] and the Bali Strait in 2015 [Fadli et al., 2017], applying regularized inversion for multi-arrival rays.

Acoustic tomography data which hold the information on sound speed (mainly related to temperature and salinity) and current velocity along sound transmission paths, are of different quality in comparison with the conventional types of data obtained by sensors deployed at one location. Current structures can be reconstructed through tomographic

inversion of travel time differences obtained for all station pairs. In spite of those efforts mentioned above, tomographic inversion could not produce high-quality mappings because of limited number of transmission lines to be used in inverse analysis. Data assimilation (DA) is a prosperous method to relax the shortage of acoustic tomography in spatial resolution. The prediction accuracy of oceanic variables (temperature, salinity and current velocity) from ocean model has been significantly improved through the assimilation of acoustic tomography data with temporal growth [Munk and Wunsch, 1979; Munk et al., 1995]. Fukumori and Malanotte-Rizzoli [1995] and Sheinbaum [1995] assimilated the simulated data of acoustic tomography into an ocean model to specify the efficiency of tomography data on model performance. Assimilation of CAT data into coastal-sea circulation model has been often attempted to map barotropic coastal currents since 2000 (Park and Kaneko, 2000; Lin et al., 2005). However, its application to baroclinic currents is rarely performed because of difficulty in resolving multi-arrival peaks along sound transmission lines crossing tomography domain.

### 1.3 Further Advancement of Data Assimilation

DA was first developed in meteorology, and then applied to oceanography. A good summary of data assimilation applied to oceanography was presented in Ghil and Melanotte-Rizzoli [1991], Bennett [1992], Fukumori [2001] and Christopher et al. [2015]. According to Ghil and Melanotte-Rizzoli [1991], data assimilation can be separated into

two classes: sequential approach based on the estimate theory and variational approach based on the control theory. The major advantage of variational assimilation is an ability to assimilate asynchronous observation data. The major drawbacks are difficulties to construct adjoint model and large computational burden. Ensemble Kalman filter (EnKF) proposed by Evensen [1994, 2003] is a representative method of sequential approach. Its major advantage in comparison with variational assimilation is simplicity to design and code. Sliced data produced by ocean acoustic tomography was proposed with the best fit to data assimilation [Munk et al., 1995]. EnKF method may be preferable in assimilation of coastal-sea data pronounced with time varying characteristics rather than variational method with heavy time consumption. On the other hand, computational burden still exists in the conventional EnKF method with model error covariance calculated by a large number of ensemble forecast of model states and updated at every data assimilation step. Further time reducing method is required for quick assimilation of time varying coastal sea data, obtained by coastal acoustic tomography.

## 1.4 Outline

This thesis is intended to study the mapping of coastal-sea environmental parameters such as temperature, salinity and current on the basis of data assimilation. Realistic mapping is realized by inverse analysis of coastal acoustic tomography data and their assimilation into coastal-sea circulation model. The remainder of this thesis is composed

of the following chapters. In Chapter 2, methods and formulation are described. A newly proposed time-efficient data assimilation scheme based on EnKF is briefly described here along with general introduction to Princeton Ocean Model (POM). Vertical-slice inversion method is also formulated. In Chapter 3, the time-efficient data assimilation method proposed in this thesis is applied to the 2013 Hiroshima Bay tomography data characterized by a typhoon-driven coastal upwelling. Chapter 4 is reserved to reconstruct current and temperature fields from the tomography data obtained in the Bali Strait. Vertical-slice inversion and barotropic data assimilation are applied. Recent advancement of coastal acoustic tomography is presented in Chapter 5. CAT with mirror-transpond functionality (MCAT) is proposed to monitor offshore subsurface environments from shore, measuring both current and temperature in a domain surrounded by offshore instruments. Forthcoming issue for coastal acoustic tomography and data assimilation are given in Chapter 6. Conclusions of this thesis are given in Chapter 7.

**References**

Apel J R, Badiey M, Chiu C S, et al. (1997). An overview of the 1995 SWARM shallow-water internal wave acoustic scattering experiment, IEEE Journal of Oceanic Engineering, 22: 465—500.

Bennett A. F. (1992). Inverse Methods in Physical Oceanography, 347pp, Cambridge University Press, Cambridge.

Chester, D. B., et al. (1991). Acoustic tomography in the straits of Florida, J. Geophys. Res., 96, 7023–7048.

Dushaw, B. D., Worcester, P. F. and Dzieciuch, M. A. (2011). "On the predictability of mode-1 internal tides", Deep-Sea Res., Part II, 58, 677–698.

Evensen, G. (1994). Sequential data assimilation with a nonlinear quasi-geostrophic model using Monte Carlo methods to forecast error statistics, J. Geophys. Res., 99, 10143-10162.

Evensen, G. (2003). The ensemble Kalman filter: Theoretical formulation and practical implementation. Ocean Dynamics, 53(4), 343–367.

Edwards, C. A., Moore, A. M., Hoteit, I., & Cornuelle, B. D. (2015). Regional ocean data assimilation. Annual review of marine science, 7, 21-42.

Fadli S., Chen, M., Kaneko A, et al. (2017). Profiling measurement of internal tides in Bali Strait by reciprocal sound transmission. Acoustical Science and Technology, 38(5), 246-253.

Fukumori, I., and Malanotte-Rizzoli, P. (1995). An approximate Kalman filter for ocean data assimilation: An example with an idealized Gulf Stream model, J. Geophys. Res., 100, 6777-6793.

Lin, J., Kaneko, A., Gohda, N., & Yamaguchi, K. (2005). Accurate imaging and prediction of Kanmon Strait tidal current structures by the coastal acoustic tomography data.

Geophysical Research Letters, 32, L14607.

Munk, W. and Wunsch, C. (1979). Ocean acoustic tomography: a scheme for large scale monitoring, Deep-Sea Res., 26A, 123-161.

Munk, W., Worceser, P. F. and Wunsch, C. (1995). Ocean acoustic tomography, 433pp, Cambridge Univ. Press, Cambridge.

Ocean Tomography Group. (1982). A demonstration of ocean acoustic tomography, Nature, 299, 121-125.

Park, J. H., and Kaneko, A. (2000). Assimilation of coastal acoustic tomography data into a barotropic ocean model, Geophys. Res. Lett., 27, 3373-3376.

Park, J. H., and Kaneko, A. (2001). Computer simulation of the coastal acoustic tomography by a two-dimensional vortex model. J. Oceanogr., 57, 593-602.

Sheinbaum J. (1995). Variational assimilation of simulated acoustic tomography data and point observations: A comparative study. J. Geophys. Res., 100, 20745-20761.

Stammer, D., et al. (2014). "Accuracy assessment of global barotropic ocean tide models". Reviews of Geophysics, 52, 243–282.

Taniguchi, N., Kaneko, A., Yuan, Y., Gohda, N., Chen, H., Liao, G., Yang, C., Minamidate, M., Adityawarman, Y., Zhu, X.-H., and Lin, J. (2010). Long-term acoustic tomography measurement of ocean currents at the northern part of the Luzon Strait, Geophys. Res. Lett., 37, L07601.

Taniguchi, N., Huang, C.-F., Kaneko, A., Howe, B. M., Wang, Y.-H., Yang, Y., Lin, J., Zhu, X.-H. and Gohda, N. (2013). Measuring the Kuroshio Current with ocean acoustic tomography, J. Acoust. Soc. Am., 134, Pt.2: 3272-3281.

Worcester, P. F., Lynch, J. F., Morawitz, W. M. L., Pawlowicz, R., Sutton, P. J., Cornuelle, B. D., Johannessen, O. M., Munk, W. H., Owens, W. B., Shuchman, R., Spindel, R. C. 1993. Evolution of the large-scale temperature field in the Greenland Sea during 1988-1989 from tomographic measurements, Geophys. Res. Lett, 20: 2211—2214.

Yamaguchi K., Lin, J., Kaneko, A., Yamamoto, T., Gohda, N., Nguyen, H.-Q. and Zheng, H. (2005). A continuous mapping of tidal current structures in the Kanmon Strait, J. Oceanogr., 61, 283-294.

Yamaoka H., Kaneko, A., Park, J.-H., Zheng, H., Gohda, N., Takano, T., Zhu, X.-H. and Takasugi, Y. (2002). Coastal acoustic tomography system and its field application, IEEE Journal of Oceanic Engineering, 27, 283-295.

Zheng, H., Gohda, N., Noguchi, H., Ito, T., Yamaoko, H., Tamura, T., Takasugi, Y. and Kaneko, A. (1997a). Reciprocal Sound Transmission Experiment for Current Measurement in the Seto Inland Sea, Japan, J. Oceanogr., 53, 117-127.

Zheng, H. (1997b). Study on Development and Application of the Coastal Acoustic Tomography System, Doctor Dissertation, Hiroshima Univ., 115pp.

Zheng, H., Yamaoko, H., Gohda, N., Noguchi, H. and A. Kanko (1998). Design of the

acoustic tomography system for velocity measurement with an application to the coasral sea, J. Acoust. Soc. Jpn. (E), 19, 199-210.

Zhu, X.-H., Zhang, C.-Z., Wu, Q.-S., Kaneko, A., Fan, X.-P. and Li, B. (2012). Measuring discharge in a river with tidal bores by use of the coastal acoustic tomography system, Estuarine, Coastal and Shelf Sci., 104-105: 54-65.

Zhu, X.-H., Kaneko, A., Wu, Q.-S., Zhang, C.-Z., Taniguchi, N. and Gohda, N. (2013). Mapping Tidal Current Structures in Zhitouyang Bay, China, Using Coastal Acoustic Tomography, IEEE J. Oceanic Eng., 38, 285-296.

# CHAPTER II METHOD AND FORMULATION

## 2.1 POM

The ocean model used in this study is the Princeton Ocean Model (POM), a three-dimensional, nonlinear, primitive equation model, which was developed by Blumberg and Mellor from 1977. Details of POM are provided by Blumberg and Mellor [1987] and Mellor [2002]. POM is a free-surface ocean general circulation model. The model solves fluid motion with the Navier-Stokes equations on a horizontal Arakawa C grid and a vertical sigma-level grid under the Boussinesq and hydrostatic approximations. The numerical scheme is leap-frog in time and centered in space. It also adopts mode-split technique. The depth-averaged 2D equations (normally called the barotropic or external mode) are solved with a smaller time step which satisfies the Cnurrant-Friedrichs-Lewy (CFL) condition. On the other side, the 3D equations (called baroclinic or internal mode) are solved with a longer time step based on the CFL condition and the internal wave speed. Horizontal mixing is parameterized according to the Smagorinsky diffusion scheme and vertical mixing coefficients are calculated with a level 2.5 Mellor-Yamada turbulence closure scheme.

## 2.2 Time-Efficient Data Assimilation

In this thesis, travel time difference and travel time summation, proportional to path-

average current and sound speed, respectively, are considered as observation data to be assimilated into ocean circulation model. Another available assimilation data for CAT are current and sound speed obtained by tomographic inversion. When compared with the accurate travel time difference and travel time summation, computation error is introduced in the inversion result because the inversion analysis cannot resolve flow fields with spatial scales smaller than spatial resolution determined from tomography array. Thus, travel time difference and summation are better as data assimilation data than inverted current and sound speed fields.

As proposed by Munk et al. [1995], the difference $\Delta d_i$ and sum $\Delta s_i$ of the i-th reciprocal travel-time perturbations relate to the path-average current and sound speed in the following forms:

$$\Delta d_i = \frac{1}{2}[(\tau_i^+ - \tau_i^0) - (\tau_i^- - \tau_i^0)] = -\int_{\Gamma_i} \frac{\vec{u} \cdot \vec{n}}{C_0^2} ds \quad (2.2.1)$$

$$\Delta s_i = \frac{1}{2}[(\tau_i^+ - \tau_i^0) + (\tau_i^- - \tau_i^0)] = -\int_{\Gamma_i} \frac{\Delta C}{C_0^2} ds \quad (2.2.2)$$

where $\tau_i^+$ and $\tau_i^-$ are the travel times for the i-th ray in the reciprocal transmission, $\tau_i^0$ is the travel time for the i-th reference ray, $\vec{u}$ is the velocity vector, $\vec{n}$ is the unit vector tangential to the ray and $\Delta C$ is the sound speed deviation from the reference sound speed $C_0$. By projecting onto a horizontal slice, the integral Eq. (2.2.1) for the path-average current is approximated by the following discrete form:

$$\Delta d_i = -\sum_{j=1}^{n} \frac{l_{ij} \cdot (u_j \cos\theta_i + v_j \sin\theta_i)}{C_0^{\,2}} \quad (2.2.3)$$

where $l_{ij}$ is the arc length of the i-th ray which crosses the j-th model grid and $n$ is the total number of model state vectors. The $u_j$ and $v_j$ are the east-west and north-south components of the current respectively, and $\theta_i$ is the angle of the i-th ray, measured counter-clockwise from the east-west line.

In Eq. (2.2.2), temperature $T$ and salinity $S$ are divided into two parts, the reference value and the deviation from it, as expressed by

$$T = T_0 + \Delta T \quad (2.2.4)$$

$$S = S_0 + \Delta S \quad (2.2.5)$$

where $T_0 >> \Delta T$ and $S_0 >> \Delta S$. Substituting $T$ and $S$ into MacKenzie's [1981] sound speed formula and disregarding the second and higher order terms in the Taylor expansion, we obtain $\Delta C$:

$$\Delta C = \alpha \Delta T + \beta \Delta S \quad (2.2.6)$$

where

$$\begin{aligned} C_0 = {} & 1448.96 + 4.591 T_0 - 0.05304 T_0^2 + 2.374 \times 10^{-4} T_0^3 \\ & + 1.340(S_0 - 35) + 1.630 \times 10^{-2} D + 1.675 \times 10^{-7} D \\ & - 1.025 \times 10^{-2} T_0 (S_0 - 35) - 7.139 \times 10^{-13} T_0 D^3 \end{aligned} \quad (2.2.7)$$

$$\begin{aligned} \alpha = {} & 4.591 - 0.05304 \times 2 T_0 + 2.374 \times 10^{-4} \times 3 T_0^2 \\ & - 1.025 \times 10^{-2} (S_0 - 35) - 7.139 \times 10^{-13} D^3 \end{aligned} \quad (2.2.8)$$

$$\beta = 1.340 - 1.025 \times 10^{-2} T_0 \quad (2.2.9)$$

In the present study, the unknown variable $\Delta T$ in Eq. (2.2.6) is determined using the temperature array data $T_{array}$ as applied to Hiroshima Bay experiment data in Chapter 3 to make salinity assimilation possible. Thus Eq. (2.2.6) becomes:

$$\Delta C = \alpha(T_{array} - T_0) + \beta\Delta S \quad (2.2.10)$$

By substituting Eq. (2.2.10), Eq. (2.2.2) becomes

$$\Delta s_i + \int_{\Gamma_i} \frac{\alpha(T_{array} - T_0)}{C_0^2} ds = -\int_{\Gamma_i} \frac{\beta\Delta S}{C_0^2} ds \quad (2.2.11)$$

Finally, Eq. (2.2.11) is rewritten in the following discrete form:

$$\Delta s_i + \sum_{j=1}^{n} \frac{l_{ij} \cdot \alpha \cdot (T_{array} - T_0)}{C_0^{\,2}} = -\sum_{j=1}^{n} \frac{l_{ij} \cdot \beta \cdot \Delta S_j}{C_0^{\,2}} \quad (2.2.12)$$

Barotropic and baroclinic information are sampled from CAT data when multi-arrival peaks traveling in different depths are identified. In order to assimilate correctly multi-arrival peak data of CAT, barotropic data assimilation (BTDA) and baroclinic data assimilation (BCDA) are separately described here. Notice that they are also compatible with mode splitting technique of ocean model. As shown in Fig 2.2.1, the arc length $l_{ij}^{BT}$ of i-th ray projected to j-th horizontal grid gives barotropic information and the arc length $l_{ij}^{BC}$ of i-th ray crossing the j-th model grid in the vertical slice gives baroclinic information. They are used to formulate the transform matrix $H_{ij}^{BT}$ and $H_{ij}^{BC}$ for barotropic and baroclinic assimilations, respectively. The superscripts *BT* and *BC* are assigned for barotropic and baroclinic assimilations, respectively. On the basis of Eqs. (2.2.3) and (2.2.12), the transform matrixes $H_{ij}^{BT}$ and $H_{ij}^{BC}$ are expressed by

$$H_{ij}^{BT} = [-\frac{l_{ij}^{BT} \cdot \cos\theta}{C_0^2}, -\frac{l_{ij}^{BT} \cdot \sin\theta}{C_0^2}] \quad (2.2.13)$$

$$H_{ij}^{BC} = [-\frac{l_{ij}^{BC} \cdot \cos\theta}{C_0^2}, -\frac{l_{ij}^{BC} \cdot \sin\theta}{C_0^2}] \quad (2.2.14)$$

for current and

$$H_{ij}^{BT} = -\frac{l_{ij}^{BT} \cdot \beta}{C_0^2} \qquad (2.2.15)$$

$$H_{ij}^{BC} = -\frac{l_{ij}^{BC} \cdot \beta}{C_0^2} \qquad (2.2.16)$$

for salinity

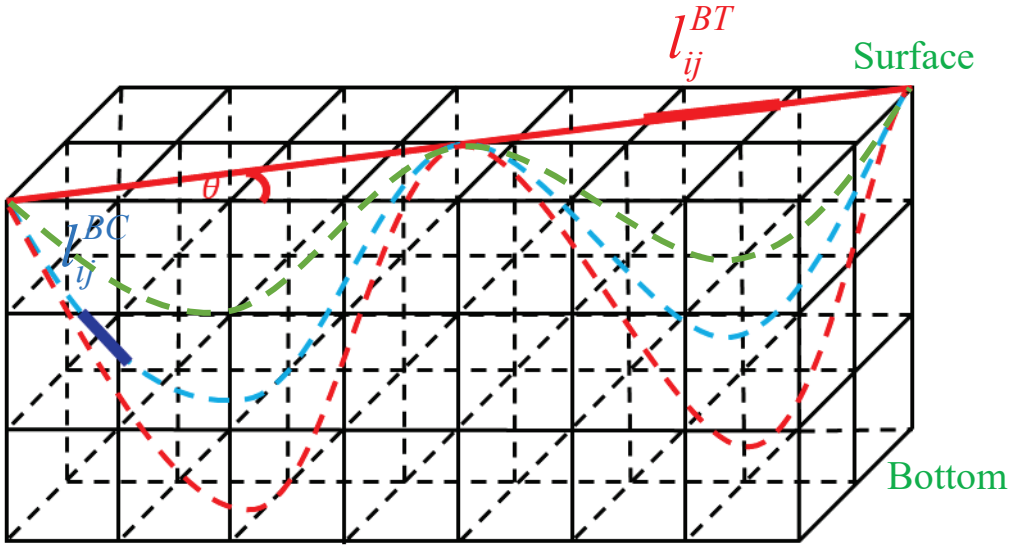


Fig. 2.2.1. Typical example of the ray patterns which give barotropic (red dashed line) and baroclinic (blue dashed line) information in model grid.

The conventional EnKF methods are derived from merging Kalman filter theory and Monte Carlo estimate [Evensen, 1994; Evensen, 2003]. EnKF updates a prior forecast of the ocean model $\psi_t^f$ at certain time $t$ with the information in observation $D_t$ to attain a realistic estimate of ocean model $\psi_t^a$ as described in Eq. (2.2.17). To this end, a Kalman gain $K_t$ with observation error covariance $R$ and model error covariance $P$ is introduced to find an optimal weight to minimize a difference between measurement $D_t$ and model estimate $H\psi_t^f$ as in Eq. (2.2.18). The transform matrix $H$ performs the

mapping from model space to observation space. Finally, a forecast model $M$ is adopted to grow up the realistic estimate $\psi_t^a$ to the model state at the next time step as in Eq. (2.2.19):

$$\psi_t^a = \psi_t^f + K_t(D_t - H\psi_t^f) \quad (2.2.17)$$

$$K_t = PH^T(HPH^T + R)^{-1} \quad (2.2.18)$$

$$\psi_{t+1}^f = M(\psi_t^a) \quad (2.2.19)$$

In the conventional method, model error covariance is estimated from ensemble forecasts with time growth. In the process constructing ensemble forecasts in typical oceanic applications, model error covariance estimate is a major source to increase the computational time exhausted for completing a DA cycle. Large ensemble size is imposed to obtain accurate model error covariance so that much computational time is consumed.

A new method of data assimilation with much time-efficient scheme based on EnKF is proposed here in which model error covariance is calculated from pseudorandom fields provided in a fixed time without time growths. A N-ensemble of smooth pseudorandom fields $\Upsilon$ is generated to calculate model error covariance, using a procedure provided from Evensen [2003].

$$\Upsilon = (\varepsilon_1, \varepsilon_2, ..., \varepsilon_n)^T \in \Re^{n \times N} \quad (2.2.20)$$

Individual sub-vectors $\varepsilon_n \in \Re^N$ have zero mean and time-invariant variance $\delta$. The covariance of $(\varepsilon_k, \varepsilon_l)$ is determined using the proposed formula from the decorrelation length of $\gamma_h$ given to fit the observation domain prior to the covariance calculation [Evensen, 2003]. The ensemble model forecast $\psi_t^f$ with $\Upsilon$ is expressed by

$$\psi_t^f = \begin{pmatrix} \varphi_1^f + \varepsilon_{11} & \cdots & \varphi_1^f + \varepsilon_{1j} & \cdots & \varphi_1^f + \varepsilon_{1N} \\ \vdots & \vdots & \vdots & \vdots & \vdots \\ \varphi_i^f + \varepsilon_{i1} & \cdots & \varphi_i^f + \varepsilon_{ij} & \cdots & \varphi_i^f + \varepsilon_{iN} \\ \vdots & \vdots & \vdots & \vdots & \vdots \\ \varphi_n^f + \varepsilon_{n1} & \cdots & \varphi_n^f + \varepsilon_{nj} & \cdots & \varphi_n^f + \varepsilon_{nN} \end{pmatrix} \qquad (2.2.21)$$

where $\varphi_i^f$ is the i-th model grid forecast and $\varepsilon_{ij}$ the j-th element of $\varepsilon_i$. Thus, *P* in Eq. (2.2.18) is determined by the equation

$$P = \frac{(\psi_t^f - \overline{\psi_t^f})(\psi_t^f - \overline{\psi_t^f})^T}{N-1} \quad (2.2.22)$$

In this study, $R$ is determined from the variation of CAT travel times, typically using standard deviation (STD) of travel time.

Thus, the Kalman gain is time-invariant during the whole DA period. The idea is the same as that proposed by Fukumori et al. [1993], in which a steady-state Kalman gain was used to assimilate sea surface topography into ocean circulation model, applying Kalman filter. Furthermore, the smooth correlation function $\lambda$, defined by Gaspari and Cohn [1999], is introduced as an effective factor to localize the effect of data assimilation inside the tomography domain and diminish its effect outside the domain by using the Schur (element-wise) product to model error covariance [Houtekamer and Mitchell, 2001]. This was achieved using a 5th order piecewise polynomial function expressed as follow:

$$K_t = (\lambda \circ P)H^T(H(\lambda \circ P)H^T + R)^{-1} \quad (2.2.23)$$

$$\lambda = \begin{cases} -\frac{1}{4}(|L|/L_0)^5 + \frac{1}{2}(L/L_0)^4 + \frac{5}{8}(|L|/L_0)^3 - \frac{5}{3}(L/L_0)^2 + 1, & 0 \le |L| \le L_0 \\ \frac{1}{12}(|L|/L_0)^5 - \frac{1}{2}(L/L_0)^4 + \frac{5}{8}(|L|/L_0)^3 & \\ \quad + \frac{5}{3}(L/L_0)^2 - 5(|L|/L_0) + 4 - \frac{2}{3}L_0/|L|, & L_0 \le |L| \le 2L_0 \\ \quad 0, & 2L_0 \le |L| \end{cases} \tag{2.2.24}$$

where $L$ is the distance apart from reference point, $L_0$ half the distance within which DA effect vanishes. The proposed method does not possess an ability to determine P independently. Instead we seek the optimal ratio of P/R which is determined by evaluating the root mean square error (RMSE) between the path-average currents from data assimilation and CAT data, changing P/R. The optimal ratio is determined at a point where the sum of RMSEs for all transmission lines is sufficiently small.

### 2.3 Vertical-Slice Inversion

The reciprocal travel time $t_i^{\pm}$ for the i-th ray $\Gamma_i$ traveling in a vertical slice is calculated by the following path integral:

$$t_i^{\pm} = \int_{\Gamma_i^{\pm}} \frac{ds}{C_0(z) + \delta C(x,z) \pm v_s(x,z)} \tag{2.3.1}$$

in which $C_0$ is the reference sound speed determined from the CTD data, $\delta C = C - C_0$, and $v_s$ is the current velocity along the ray. The travel time $t_{0i}$ for $C_0$ is calculated along the reference ray $\Gamma_{0i}$ using the CTD data as

$$t_{0i} = \int_{\Gamma_{0i}} \frac{ds}{C_0(z)} \tag{2.3.2}$$

The deviation of the reciprocal travel time $\tau_i^{\pm}$ from $t_{0i}$ is calculated by subtracting Eq. (2.3.2) from Eq. (2.3.1). By linearizing the resulting equation around $C_0$ and $\Gamma_{0i}$, $\Gamma_i^{\pm}$ is replaced by $\Gamma_{0i}$. Taking the difference ($\Delta\tau_i$) and sum ($\delta\tau_i$) of $\tau_i^{\pm}$, one can separate the effects of $v_s$ and $\delta C$ on the travel time. Next, $\Delta t_i$ and $\delta t_i$, given by integrals along the i-th ray $\Gamma_{0i}$, are approximated by the following summations:

$$\Delta\tau_i = \sum_{j=1}^{N} E_{ij} v_{sj} \qquad (2.3.3)$$

$$\delta t_i = \sum_{j=1}^{N} E_{ij} \delta C_j \qquad (2.3.4)$$

where i and j are the indices for the rays and layers, respectively, and $E_{ij} = -2l_{ij} / C_{0j}^{\,2}$. The $v_{sj}$ and $\delta C_j$ are the current velocity and sound speed deviation for the j-th layer, respectively, $l_{ij}$ is the arc length of the i-th ray crossing the j-th layer, and $C_{0j}$ is the reference sound speed for the j-th layer. The travel time vector **y**, the unknown variable vector **x**, the transform matrix **E,** and the travel time error vector **n** are related in the matrix form as

$$\mathbf{y} = \mathbf{E}\mathbf{x} + \mathbf{n} \qquad (2.3.5)$$

where $\mathbf{y} = \{\Delta t_i\}$ or $\{\delta t_i\}$, $\mathbf{x} = \{v_{sj}\}$ or $\{\delta C_j\}$, and the error residuals are denoted by $\mathbf{n} = \{n_i\}$.

The regularized inversion is applied to solve Eq. (2.3.5). The least-squares solution $\hat{\mathbf{x}}$ is determined that minimizes the cost function [MacKenzie K. V., 1981]

$$\mathbf{J} = (\mathbf{y} - \mathbf{E}\mathbf{x})^{\mathrm{T}} (\mathbf{y} - \mathbf{E}\mathbf{x}) + \lambda \mathbf{x}^{\mathrm{T}} \mathbf{H}^{\mathrm{T}} \mathbf{H}\mathbf{x} \qquad (2.3.6)$$

where $\lambda$ is the Lagrange multiplier, superscript T denotes the transpose of a matrix, and

**H** is the smoothing matrix constructed from a finite-difference approximation of the second-order derivative operator $\partial^2\mathbf{x}/\partial z^2$, which is introduced to regularize a solution through a moving average of three consecutive layers.

$$\int_{-D}^{0}\left(\frac{\partial^2\mathbf{x}}{\partial z^2}\right)^2 dz = \sum_{\mathbf{i=1}}^{\mathbf{M}}\left(\mathbf{x_{i-1}} - \mathbf{2x_i} + \mathbf{x}_{\mathbf{i+1}}\right)^2 = \mathbf{x^T H^T H x} \quad (2.3.7)$$

Here, $D$ is the seafloor depth and the vertical grid width $\Delta z$ is taken to be $\Delta z$=1. For the 5 layers, $H$ is expressed by

$$\mathbf{H} = \begin{bmatrix} -2 & 1 & 0 & 0 & 0 \\ 1 & -2 & 1 & 0 & 0 \\ 0 & 1 & -2 & 1 & 0 \\ 0 & 0 & 1 & -2 & 1 \\ 0 & 0 & 0 & 1 & -2 \end{bmatrix} \quad (2.3.8)$$

By minimizing **J**, the optimal solution $\hat{\mathbf{x}}$ reduces to

$$\hat{\mathbf{x}} = \left(\mathbf{E^T E} + \boldsymbol{\lambda}\mathbf{H^T H}\right)\mathbf{E^T y} \quad (2.3.9)$$

where $\boldsymbol{\lambda}$ is chosen so that the squared residual defined by $\|\hat{\mathbf{n}}\|^2 = \|\mathbf{y} - \mathbf{E}\hat{\mathbf{x}}\|^2$ is less than a predetermined value of 0.2 ms$^2$, corresponding to 0.05 ms$^{-1}$ for both the current and sound speed for the station-to-station distance of 4,461 m. The solution uncertainty **P** is formulated in the form [Munk, et al., 1995].

$$\mathbf{P} = \left(\mathbf{E^T E} + \boldsymbol{\lambda}\mathbf{H^T H}\right)^{-1}\mathbf{E^T} < \mathbf{nn^T} > \mathbf{E}\left(\mathbf{E^T E} + \boldsymbol{\lambda}\mathbf{H^T H}\right)^{-1} \quad (2.3.10)$$

where <**nn**$^{\mathbf{T}}$> is the expected variance of the travel time difference ($\Delta t$) or sum ($\delta t$). Only the diagonal components are taken into consideration because small cross-correlation errors are expected between different layers. Finally, the inversion error for each layer is expressed by

$$V_{error} = diagonal\ (\sqrt{\mathbf{P}_{\Delta t}}) \qquad (2.3.11)$$

$$C_{error} = diagonal\ (\sqrt{\mathbf{P}_{dt}}) \qquad (2.3.12)$$

$$T_{error} = C_{error} / 2.37 \qquad (2.3.13)$$

**Reference**


Blumberg, A. F., and Mellor, G. L. (1987). A description of a three-dimensional coastal ocean circulation model. In N. Heaps (Ed.), Three-dimensional coastal ocean models (pp. 1-16). Washington, DC: American Geophysical Union.

Evensen, G. (1994). Sequential data assimilation with a nonlinear quasi-geostrophic model using Monte Carlo methods to forecast error statistics, J. Geophys. Res., 99, 10143-10162.

Evensen, G. (2003). The ensemble Kalman filter: Theoretical formulation and practical implementation. Ocean Dynamics, 53(4), 343–367.

Fukumori, I., Benveniste, J., Wunsch, C., & Haidvogel, D. B. (1993). Assimilation of sea surface topography into an ocean circulation model using a steady-state smoother. Journal of Physical Oceanography, 23(8), 1831-1855.

Gaspari, G., & Cohn, S. E. (1999). Construction of correlation functions in two and three dimensions. Quarterly Journal of the Royal Meteorological Society, 125, 723–757.

Houtekamer, P. L., & Mitchell, H. L. (2001). A sequential ensemble Kalman filter for atmospheric data assimilation. Monthly Weather Review, 129(1), 123–137.

MacKenzie, K. V. (1981). Nine-term equation for sound speed in the ocean, J. Acoust. Soc. Am., 70, 807-812.

Mellor, G. L., Häkkinen, S. M., Ezer, T., and Patchen, R. C. (2002). A generalization of a sigma coordinate ocean model and an intercomparison of model vertical grids. In Ocean Forecasting (pp. 55-72). Springer Berlin Heidelberg.

Munk, W., P. F. Worceser, and C. Wunsch (1995). Ocean acoustic tomography, 433pp, Cambridge Univ. Press, Cambridge, U. K.

# CHAPTER Ⅲ HIROSHIMA BAY STUDY

## 3.1 Introduction

Coastal acoustic tomography (CAT) is an application of ocean acoustic tomography to shallow, coastal seas. The technique uses acoustic data to derive the spatial structures of current and sound speed. Data assimilation (DA) techniques can be applied to the acoustic data to constrain an ocean model, as proposed by Munk and Wunsch [1979] and Munk et al. [1995]. Ocean estimates derived from CAT have been well tested by comparisons with ADCP data [Yamaoka et al., 2002; Yamaguchi et al., 2005; Zhu et al., 2012; Zhu et al., 2013] and CTD data [Zhang et al., 2015]. All previous studies using CAT have employed barotropic models because of limitations of the acoustic data. Those studies had difficulties distinguishing and identifying multiple ray arrivals because of the nature of sound transmission in shallow seas [Park and Kaneko, 2000; Lin et al., 2005]. Park and Kaneko [2000] first assimilated CAT data into the barotropic Princeton Ocean Model (POM) using the ensemble Kalman filter (EnKF), and forecasting model error covariance by means of a Monte Carlo method; they reconstructed a vortex pair that was generated by a strong tidal current in the Neko-Seto Channel in the Seto Inland Sea, Japan. An assimilation of CAT data was also performed by Lin et al. [2005] using EnKF, combined with a smoothed Kalman gain, that successfully reconstructed the rapidly varying vortex-embedded barotropic current generated by strong tidal currents in the Kanmon Strait, Japan. Heretofore, CAT data with depth dependent information have not been obtained

because of difficulty identifying multi-arrival rays that turn at different depths. Here, such data have been obtained, and are assimilated into an ocean model.

Hiroshima Bay, located at the western part of the Seto Inland Sea, Japan, is elliptical in shape with a north-south length of 50 km and an east-west length of 20 km. The northern part of the bay is further semi-enclosed on a 10-km scale, on the northern side by the south coast of Hiroshima City, and on the southern side by three islands: Miyajima, Etajima and Ninoshima (Fig. 3.1.1). Despite its importance as the largest aquaculture field in Japan, no systematic oceanographic observations based on moored instrumentation have been conducted due to constraints based on aquaculture activity and shipping traffic within the bay. These societal constraints highlight the utility of CAT arrays as an oceanographic platform [Nguyen et al., 2009; Zhang et al, 2015].

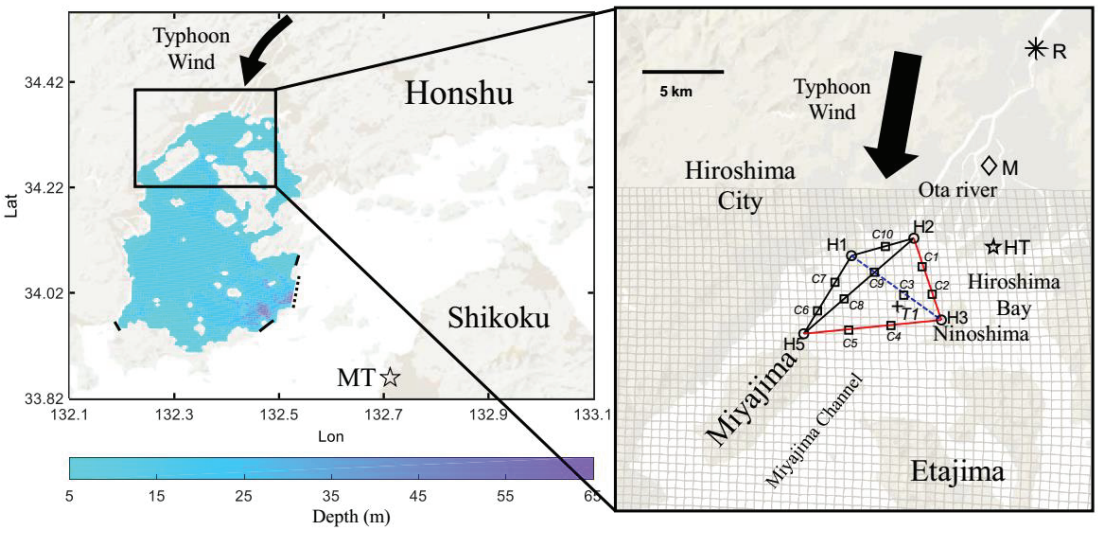


Fig. 3.1.1. POM computational domain with bathymetry chart (left panel) and the CAT station array at a magnified scale (right panel). Left panel: The black dashed line indicates

the open boundary and the black thick lines are artificially closed narrow gaps. The color scale for depth is at the bottom of the figure. Right panel: The four CAT acoustic stations (H1, H2, H3 and H5) and ten CTD points (C1-C10) are indicated with circles and squares, respectively. Black lines connecting the acoustic stations show the reciprocal sound transmission lines and red lines the one-way sound transmission lines. The blue dashed line is the transmission line with no data. T1 is the temperature array position, HT the Hiroshima tide gauge station, MT the Matsuyama tide gauge station, M the Hiroshima JMA meteorological station, and R the MLITT Yaguchi Ota River gauge station. Grid lines on the bay are the model grid. A distance scale of 5 km is shown at the top-left corner of the panel.

The Ota River discharges into the northern part of Hiroshima Bay with five distributaries and volume transports smaller than 100 $m^3s^{-1}$ except during periods of flooding. As a result of the continuous river discharge, Hiroshima Bay is characterized as a two-layer system with a fresh, near-surface layer overlaying a more saline, lower layer. This two-layer stratification enables acoustic travel time estimates from CAT data for two separate ray paths and the subsequent assimilation of the data into a full barotropic+baroclinic ocean model.

Upwelling generated in a semi-enclosed bay of 10-km scale, such as the northern part of Hiroshima Bay, may be a localized event with lesser Coriolis effects in the cross-shore current than in the alongshore current [Taylor and Stewart, 1959; Thomson, 1981; Hunt,

1995]. A coastal upwelling event, which occurs during a few days from initiation and growth to decay, is measurable in a sequence of snapshots by assimilating CAT data into a full barotropic+baroclinic ocean model. A previous paper which studied the internal-mode structure of mesoscale eddies from tomographic data might be regarded as a good precursor of the present study, despite having dynamics different from those of coastal upwelling [Gaillard, 1992].

In this chapter, data assimilation is performed, using high quality CAT data and a modified DA method. Initiation, growth and decay processes of coastal upwelling and the associated dynamic phenomena are specifically targeted by this study.

## 3.2 Observations and Methods

### 3.2.1 Site and data acquisition

A CAT experiment with four acoustic stations (H1, H2, H3, and H5) was conducted from September 11 to 25, 2013, covering the period when typhoon T1318 passed over Hiroshima Bay on September 16 (Figure 1). Experiment details have been described in a previous paper [Zhang et al., 2015], so only the information specific to this study is presented here. The conductivity-temperature-depth (CTD) data were acquired at 10 stations (C1-C10 on the sound transmission lines) on September 18. The CTD data were used to construct sound speed fields that were then used for acoustic ray-trace predictions in the tomography domain with a vertical profile of temperature from September 17,

provided by the Hiroshima City Fisheries Promotion Center (HCFPC). Long-term temperature profiles were obtained at depths of 0, 2, 4, 7, 10 and 15 m every 5 minutes from August 1 to October 23 using a temperature array, placed at T1, and performing a sound speed-to-salinity conversion using the sound speed formula. Ota River transport data, obtained from the Yaguchi Gauge Station (YGS) of the Ministry of Land, Infrastructure, Transport and Tourism (MLITT), were used to compare with the volume transport generated in the tomography domain by coastal upwelling.

Sound was transmitted every 10 minutes from all four stations and the 10-min interval data were processed using an hourly moving average to increase the signal-to-noise ratio (SNR) of the received signals. The hourly-mean data, mainly characterized by tidal components, were further processed through a 2-day low pass filter to detect sub-tidal components. Hereinafter the former data are called the hourly-mean data and the latter the 2-day filtered data.

Sound transmission was heavily interrupted by oyster aquaculture rafts, distributed along the bay. As a result, reciprocal data were obtained only for the station pairs H1H2, H2H5 and H5H1. One-way data were obtained from H2 to H3 and from H5 to H3 because the source level of the sound transmitted from H3 was too weak owing to incorrect settings of the output circuit. To perform a baroclinic data assimilation, multi-arrival peaks must be identified in the received data. In this study, the first arrival peak was identified as the one with the largest SNR with SNR>4 - the first threshold condition - in the received data, and the second arrival peak was identified as the largest peak with

SNR>4 in a time window of 1.5-2.5 ms after the first peak, considering the travel times from ray simulation described below. A second threshold condition to remove unusual path-averaged currents over 0.6 $ms^{-1}$ was further adopted for the reciprocal transmission lines H1H2, H2H5 and H5H1.

Two arrival peaks were successfully identified among H1, H2 and H5, constructing a triangular array (Figure 1). However, second peaks could not be identified for H2H3 and H3H5 owing to poor performance of the H3 system. The mean travel time differences between the first and second arrival times were 1.983 ms, 1.996 ms and 2.023 ms for H1H2, H2H5 and H5H1, respectively. Correlation patterns for the received signals are shown with stack diagrams in Fig. 3.2.1. The green and red dots correspond to arrival peaks for the surface-bottom reflected (SBR) rays and surface reflected (SR) rays, respectively. The SBR rays with the number of surface reflection smaller than the SR rays were the first arrivals and largest peaks for H2H5 and H5H1 while the SR rays with the number of surface reflection smaller than the SBR rays were the first arrivals and largest peaks for H1H2. The SBR rays that passed through the whole depth from the surface to the bottom sampled the depth-average current and sound speed. Hence, information from the SBR rays is suitable for assimilation into the POM results as barotropic (depth-average) data, thus being called a “barotropic data assimilation” (BTDA). On the other hand, the SR rays passed through the uppermost 5 m only, and give baroclinic information to the POM, producing a “baroclinic data assimilation” (BCDA). Semi-diurnal periods are visible in the stack data, especially for H1H5 and H2H5 crossing the central part of

the tomography domain. One-way data for H3H5 were too noisy owing to unknown aquaculture factors.

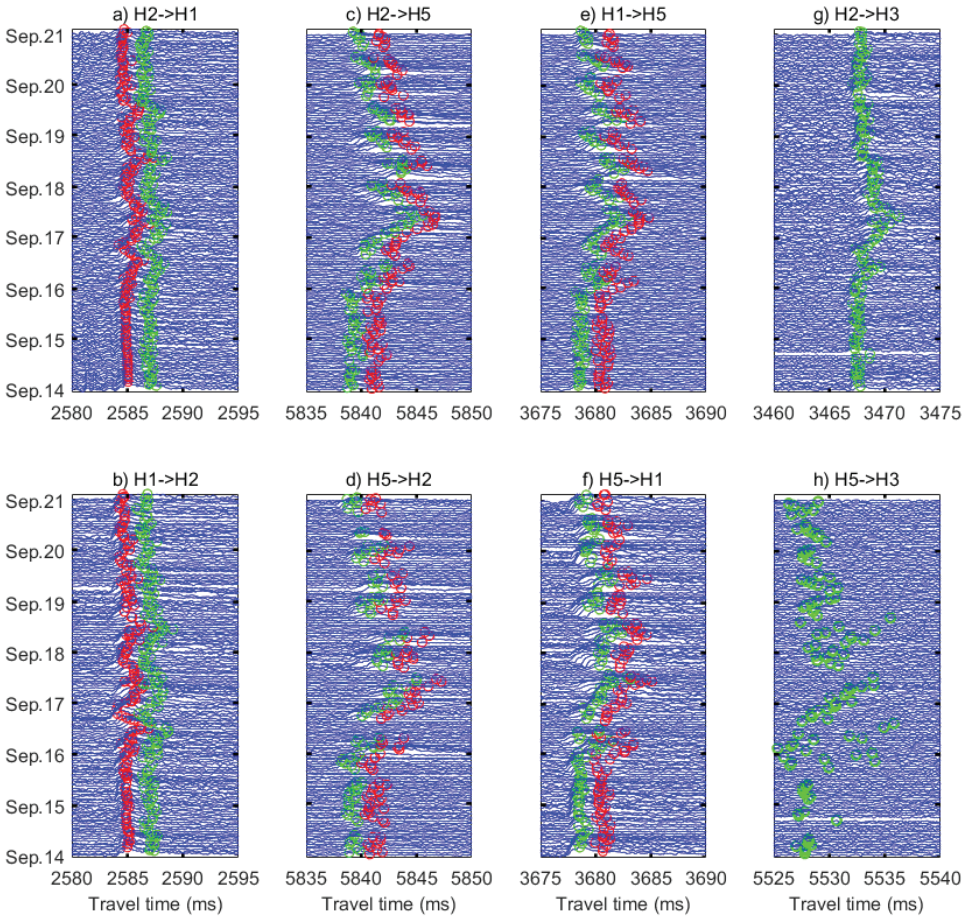


Fig. 3.2.1. Stack diagrams of the received correlation patterns plotted with the time axis proceeding upward. Green and red dots indicate arrival peaks for the SBR and SR rays, respectively.

### 3.2.2 Ray simulation

Ray simulation of sound transmission processes is a fundamental element of acoustic

tomography in order to understand how sound propagates through the intervening ocean; this is the “forward problem”. Figure 3.2.2 shows the ray patterns, obtained using the Bellhop simulation code with a range-independent sound speed profile [Ocean Acoustics Library, http://oalib.hlsresearch.com]. The temperature data on September 17 and the salinity data from the CTD on September 18 were combined to construct a sound speed profile for the range-independent ray simulation (Fig. 3.2.2a). For H2H5 and H5H1, the simulated SBR rays correspond to the first arrival peak, while for H1H2 the simulated SBR rays correspond to the second arrival peak. The simulated SR rays with a 2 ms delay from the first arrival peak correspond to the second arrival peak for H2H5 and H5H1 and, conversely, to the first one for H1H2 as seen in Figs. 3.2.2(b)-3.2.2(g). For the three transmission lines, the SR rays have their lower turning points at a depth of about 5 m, implying the presence of a halocline at this depth.

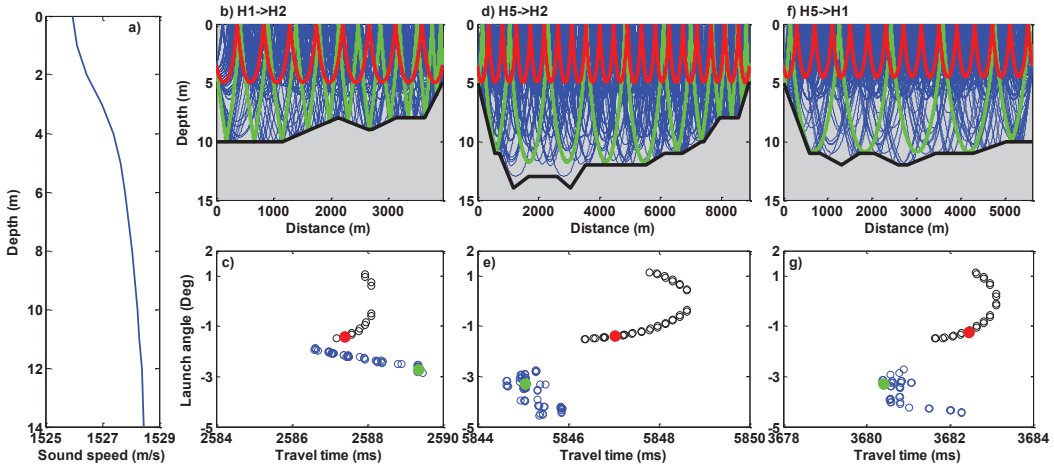


Fig. 3.2.2. Results of range-independent ray simulation along the three reciprocal transmission lines H1H2, H2H5 and H5H1. The green and red lines show the SBR and SR rays, respectively. The green and red dots indicate simulated travel times for the SBR

and SR rays, respectively.

### 3.3 Model and Data assimilation

#### 3.3.1 POM

The ocean model used in this study is POM with tidal and wind forcing, details of which are provided by Blumberg and Mellor [1987] and Mellor [2002]. The horizontal grid size is 490m for the east-west direction and 550m for the north-south direction, and the number of vertical grid nodes is 10, using the sigma coordinate system. Boundary conditions for non-slip and non-normal currents are given at the step-wise coast. An open boundary of width 6,500 m with tidal forcing is located at the southeast inlet of Hiroshima Bay (see Fig.3.1.1). These sea level data are provided with a time delay of 30 minutes from the Matsuyama tide gauge station (marked as MT in Figure 1) of the Japan Coast Guard (JCG). The simulated tide is compared with the Hiroshima tide gauge data to confirm the accuracy. Three gaps with widths smaller than 1,500 m at the periphery of the bay are artificially closed due to their narrowness and lack of tide data. The hourly-mean wind data from the Hiroshima station of the Japan Meteorological Agency (JMA) (marked as M in Fig. 3.1.1) are used to simulate wind forcing at the surface of Hiroshima Bay. Air-sea heat exchange is not taken into account, because coastal upwelling in Hiroshima Bay is a short-term phenomenon with one-day duration and the effect of a typhoon 450 km away from Hiroshima Bay is small. Also, during the typhoon period

discharge from the Ota River is not taken into account because it is as small as 30 $m^3s^{-1}$ with no flooding occurring.

The POM simulation was started on September 4 and continued for 19 days up to September 23 after the termination of upwelling and associated events. The first seven days are regarded as a spin-up period for barotropic mode with horizontally and vertically homogeneous temperature and salinity. The CTD data provided by HCFPC on September 11 were used as the initial conditions of baroclinic modes after the spin-up time was completed. Current and salinity were assimilated from 00:00 on September 14 to 00:00 on September 21 and from 00:00 on September 15 to 00:00 on September 21, respectively. This type of 6-day salinity assimilation was adopted in order to focus on the coastal upwelling and the associated events that occurred in the 4-day period of September 16 to 19, and to tackle a problem occurring at the edge of the 2-day low-pass filter. Note that all times are given in JST.

The tidal residual current (TRC) was calculated from the POM current, generated by tidal forcing alone. This TRC estimate was applied here despite its underestimation of the actual TRC because more accurate methods were not available. Sub-tidal currents were calculated by subtracting the POM-derived TRC from the 2-day filtered DA-derived current.

### 3.3.2 Data assimilation

The CAT data were assimilated into the POM, using a modified method based on the EnKF with model state vectors composed of east-west and north-south velocity components and salinity being perturbed by time-invariant smooth pseudorandom fields. Mathematically, it is impossible to determine temperature and salinity simultaneously from the sound speed formula for a given sound speed. We estimated salinity using the temperature array data and the sound speed formula. In this modified method, model error covariance stems from the model state vectors perturbed by time-invariant pseudorandom noise with a certain decorrelation length. Thus, a steady Kalman gain is obtained with time consumption much less than that for the conventional method in which model error covariance is calculated through an ensemble of forecast results. Another aspect of this method is that observation error covariance is provided from CAT data unlikely to Evensen [1994, 2003] in which observation error covariance also comes from pseudorandom noises.

In this study, the decorrelation length $\gamma_h$ of pseudorandom noises is assumed to be 9 km, almost as long as the tomography domain. The ensemble number $N$ is set to 250 and observation error covariance $R$ is determined from the variation of CAT travel times, using standard deviation (STD), in a short-period range of 10 min to one hour. The smooth correlation function $\lambda$, defined by Gaspari and Cohn [1999], is introduced as an effective factor to localize the effect of data assimilation inside the tomography domain

and diminish its effect outside the domain. This was achieved using Eq. (2.2.24) which has $\lambda = 0.6$ at H3, at a distance of 4.6 km from the center (marked O in Fig. 3.3.1) of concentric circles with constant $\lambda$. Note that this distance is nearly half the size of the tomography domain (9 km).

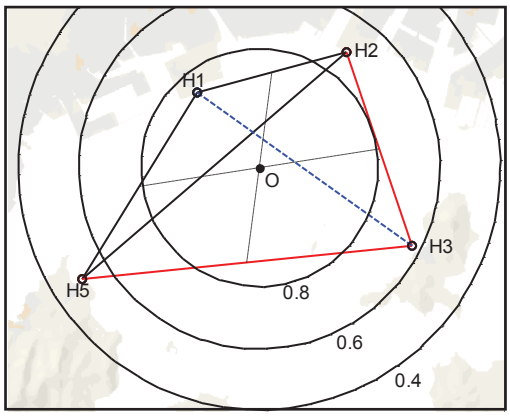


Fig. 3.3.1. Contour plot of $\lambda$, represented as concentric circles with center O and contour interval 0.2.

The mode splitting technique is applied to calculate separately the barotropic (external) and baroclinic (internal) modes in POM. Data assimilation is devised using the same scheme as the model. The difference of travel-time perturbations for the first arrival peak at H2H5 and H5H1, and for the second arrival peak at H1H2, corresponding to the SBR rays, was first assimilated into the barotropic mode for current (barotropic assimilation). The sum of travel time perturbations for the SBR rays at H1H2, H2H5 and H5H1 and the one-way travel time of travel-time perturbations for the SBR rays at H2H3 and H3H5 were also assimilated in the barotropic mode for salinity (barotropic assimilation). The barotropic DA results served to adjust the baroclinic model result. The difference of

travel-time perturbations for the second arrival peak at H2H5 and H5H1, and for the first arrival peak at H1H2 were related to the SR rays. The SR rays passed only through the uppermost 5 m and provided baroclinic information for the model. This baroclinic information was assimilated into the baroclinic mode with 10 vertical grid nodes (baroclinic assimilation). Furthermore, the sums of travel-time perturbations for the SR rays at H1H2, H2H5 and H5H1 were incorporated into the salinity in this baroclinic mode (baroclinic assimilation).

Only two arrival peaks or two rays were resolvable in the observation data because the profiles of sound speed and salinity were characterized by an upper and a lower layer separated by a steep slope at 5-m depth (see the left panel of Fig. 3.2.2). The result of the 10-vertical-grid-point data assimilation was therefore well approximated by the 2-layer result, averaging the upper and lower layers.

From equations (2.2.13) and (2.2.14) for the current, H is written in matrix form:

$$H=\begin{pmatrix} -\frac{l_{11}\cdot\cos\theta_1}{C_0^{\,2}} & \cdots & -\frac{l_{1j}\cdot\cos\theta_1}{C_0^{\,2}} & \cdots & -\frac{l_{1n}\cdot\cos\theta_1}{C_0^{\,2}} & -\frac{l_{11}\cdot\sin\theta_1}{C_0^{\,2}} & \cdots & -\frac{l_{1j}\cdot\sin\theta_1}{C_0^{\,2}} & \cdots & -\frac{l_{1n}\cdot\sin\theta_1}{C_0^{\,2}} \\ \vdots & \cdots & \vdots & \cdots & \vdots & \vdots & \cdots & \vdots & \cdots & \vdots \\ -\frac{l_{i1}\cdot\cos\theta_i}{C_0^{\,2}} & \cdots & -\frac{l_{ij}\cdot\cos\theta_i}{C_0^{\,2}} & \cdots & -\frac{l_{in}\cdot\cos\theta_i}{C_0^{\,2}} & -\frac{l_{i1}\cdot\sin\theta_i}{C_0^{\,2}} & \cdots & -\frac{l_{ij}\cdot\sin\theta_i}{C_0^{\,2}} & \cdots & -\frac{l_{in}\cdot\sin\theta_i}{C_0^{\,2}} \\ \vdots & \cdots & \vdots & \cdots & \vdots & \vdots & \cdots & \vdots & \cdots & \vdots \\ -\frac{l_{61}\cdot\cos\theta_6}{C_0^{\,2}} & & -\frac{l_{6j}\cdot\cos\theta_6}{C_0^{\,2}} & & -\frac{l_{6n}\cdot\cos\theta_6}{C_0^{\,2}} & -\frac{l_{61}\cdot\sin\theta_6}{C_0^{\,2}} & & -\frac{l_{6j}\cdot\sin\theta_6}{C_0^{\,2}} & & -\frac{l_{6n}\cdot\sin\theta_6}{C_0^{\,2}} \end{pmatrix} \quad (3.3.1)$$

where $i=(1,\ 2,\ 3)$ are assigned to the SBR rays and $i=(4,\ 5,\ 6)$ to the SR rays. Using equations (2.2.15) and (2.2.16) for salinity, *H* is written in the following matrix form:

$$H = \begin{pmatrix} -\frac{l_{11}\cdot\beta}{C_0^{\,2}} & \cdots & -\frac{l_{1j}\cdot\beta}{C_0^{\,2}} & \cdots & -\frac{l_{1n}\cdot\beta}{C_0^{\,2}} \\ \vdots & \cdots & \vdots & \cdots & \vdots \\ -\frac{l_{i1}\cdot\beta}{C_0^{\,2}} & \cdots & -\frac{l_{ij}\cdot\beta}{C_0^{\,2}} & \cdots & -\frac{l_{in}\cdot\beta}{C_0^{\,2}} \\ \vdots & \cdots & \vdots & \cdots & \vdots \\ -\frac{l_{81}\cdot\beta}{C_0^{\,2}} & & -\frac{l_{8j}\cdot\beta}{C_0^{\,2}} & & -\frac{l_{8n}\cdot\beta}{C_0^{\,2}} \end{pmatrix} \quad (3.3.2)$$

where $i = (1,\ 2,\ ...,\ 6)$ is assigned for the three SBR rays and three SR rays at the reciprocal transmission lines H1H2, H2H5 and H5H1 and $i = (7,\ 8)$ for the two SBR rays at the one-way transmission lines H2H3 and H3H5.

The proposed method cannot determine *P* correctly because DA is not yet adopted in Eq. (2.2.22). Instead we seek the optimal ratio of *P*/*R* which is an adjustable factor. The optimal value of the ratio $\gamma = P/R$ was determined to be 12 from Fig. 3.3.2 in which the root mean squares errors (RMSEs) for the DA path-average currents and CAT path-average currents were plotted against $\gamma$. In all six cases for the three reciprocal lines and two arrival peaks, RMSEs rapidly decreased with increasing $\gamma$ up to 5, and gradually decreased with further increase of $\gamma$. The errors were slightly larger for the SBR rays of H1H2 and H5H1, compared to other cases. The errors produced gentle slopes for $\gamma > 12$. As a result, $\gamma = 12$ was selected as the optimal value. This value was applied to the assimilation of salinity as well.

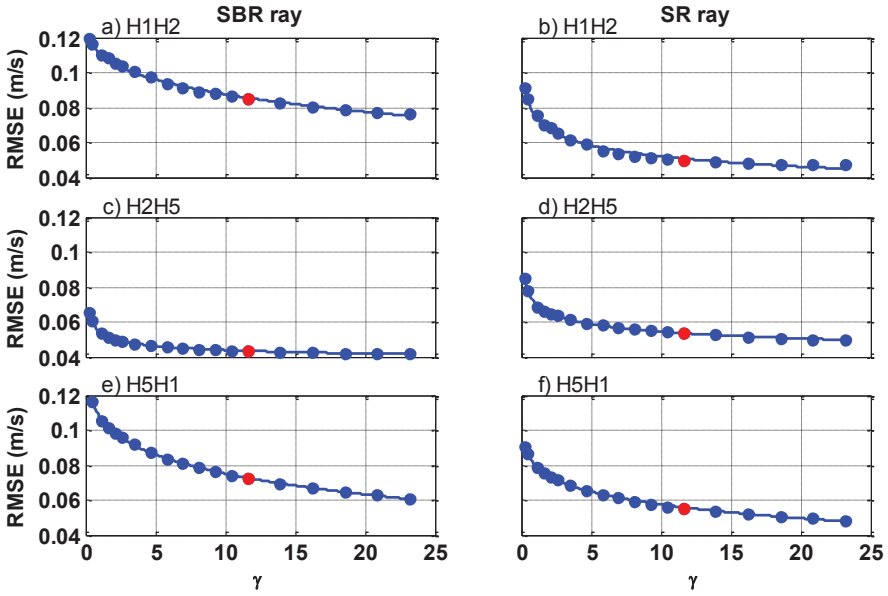


Fig. 3.3.2. RMSEs for the DA and CAT path-average currents, constructed for the SBR (left) and SR (right) rays and plotted against $\gamma$. Red dots indicate RMSE values at $\gamma = 12$.

### 3.4 Results

In Fig. 3.4.1, the BTDA results are shown with the 3-hour-interval vector plots for hourly-mean current from 00:00 on September 16 to 00:00 on September 17, and compared with the POM results. During this period, coastal upwelling was initiated and grew. The POM current was significantly strengthened through the BTDA. Tidal currents were mainly characterized by the stronger northward currents, flushed out from the Miyajima Channel and the weaker southward currents, taken into the channel. Tidal currents were directed northward during the flood tide, with a maximum value of 0.6 $ms^{-1}$, and they were reversed during the ebb tide, with a smaller maximum current of 0.3 $ms^{-}$

[1].

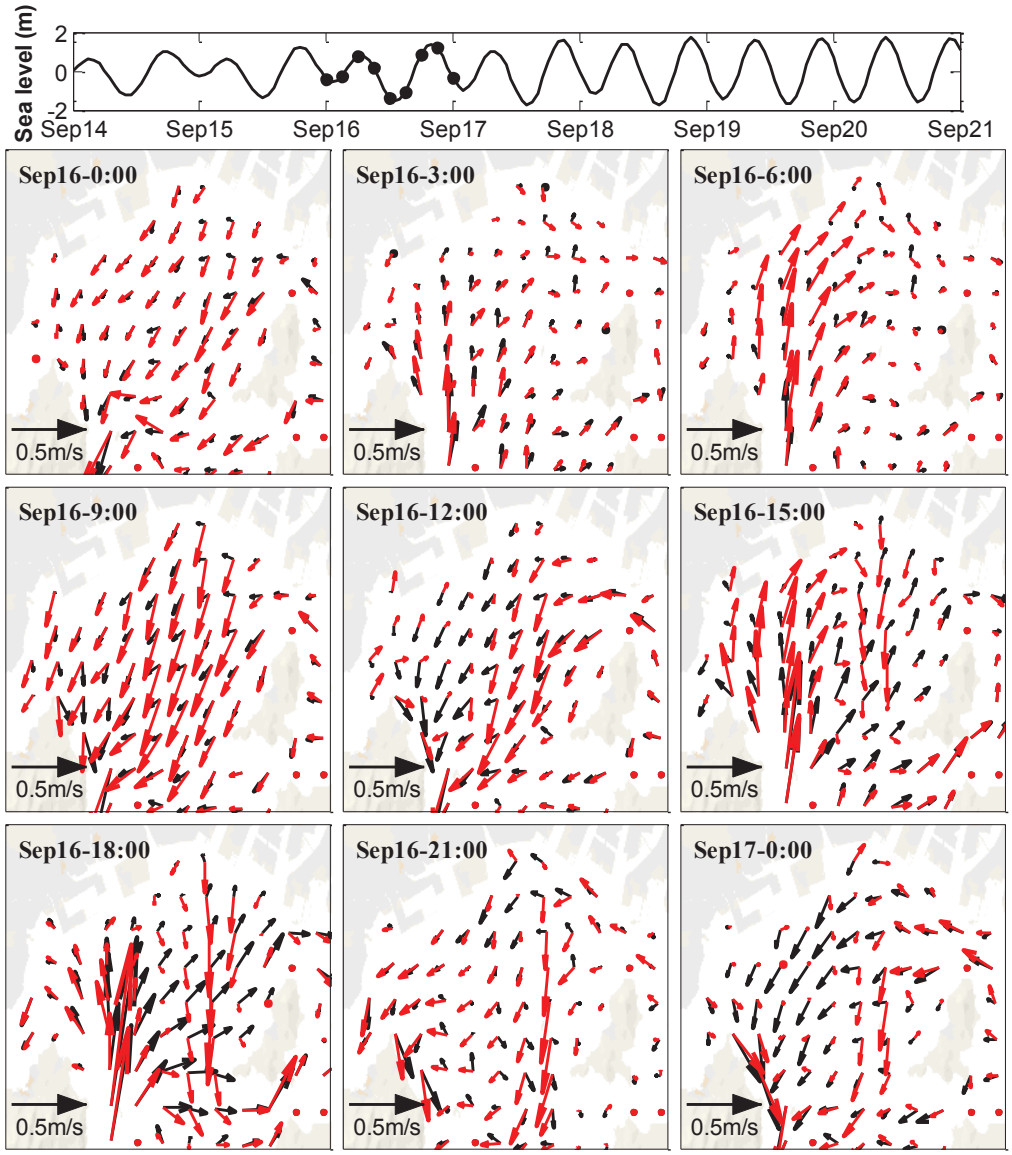


Fig. 3.4.1. Time variations of the hourly-mean BTDA (red arrows) and POM (black arrows) currents with tidal and wind forcing, plotted at 3-hour intervals from 00:00 on September 16 to 00:00 on September 17. The simulated sea level change is shown at the top of the figure. Dots on the sea level curve are placed at times corresponding to the 3-hour interval current pictures. A scale of 0.5 $ms^{-1}$ is provided at the bottom-left corner of

each panel.

The BCDA results are shown in Fig. 3.4.2 with half-day interval vector plots for the subtidal component (mainly the wind-driven current), averaged over the upper and lower layers. The subtidal current was less than 0.02 $ms^{-1}$ before the maximum northerly wind blew over the bay at 10:00 on September 16 and strengthened with the decrease of the northerly wind after it reached its maximum. Around the northern part of the bay during 00:00-12:00 on September 17 the subtidal currents were directed southward in the upper layer while the lower layer was directed by a northward current. During this mature phase of the upwelling, the magnitude of the subtidal current reached 0.10 $ms^{-1}$ in the upper layer and 0.08 $ms^{-1}$ in the lower layer. As time proceeded, the southward upper-layer current gradually diminished and was replaced, from the beginning of September 19, by a northeastward current with a maximum value of 0.10 $ms^{-1}$. During this period, the lower-layer current with magnitude less than 0.05 $ms^{-1}$ also shifted from northward to southeastward, especially in the eastern half of the bay.

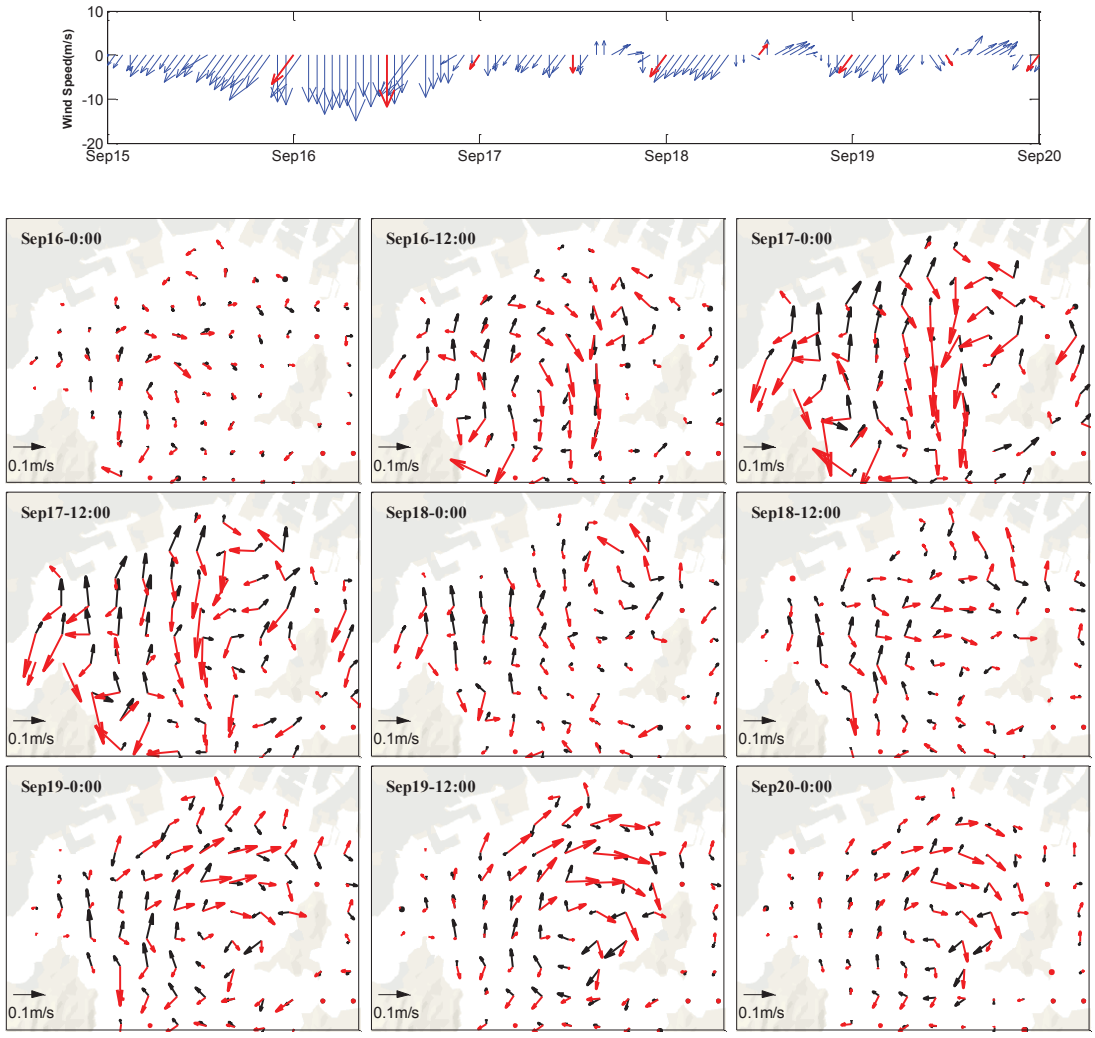


Fig. 3.4.2. The 12-hour interval variations of the subtidal BCDA currents for the upper-layer (red arrows) and lower-layer (black arrows) from 00:00 on September 16 to 00:00 on September 20. The temporal variation of wind vectors is also shown at the top of the figure. The thick red arrows on the wind speed plot are placed at times corresponding to the 12-hour interval current pictures. A scale of 0.1 $ms^{-1}$ is provided at the bottom-left corner of each figure.

The DA salinity results for the 2-day filtered data are shown in Fig. 3.4.3 with contour plots for the upper- and lower-layer averages**.** With the start of salinity assimilation at

00:00 on September 15, a salinity contrast of 28.5 and 29.5 developed between the upper and lower layers, respectively, except for the northern shore region which displayed unusually high salinity of 32. This contrast continued up to 06:00 on September 16. In the upper layer, a tongue of saline water greater than S=31 begun to develop southward from the northern shore of the bay at 18:00 on September 16 and reached a mature phase during 00:00-12:00 on September 17. Outside the tongue, the upper-layer salinity was 30.0-30.5, less than the lower-layer salinity of 30.5-31.0. After the mature phase, the upper-layer saline tongue gradually retreated northeastward up to the end of September 19. From September 18 to 19, the upper-layer salinity gradually decreased from 30.5 to 30.0 except in the tongue region. At the same time, the lower-layer salinity stayed almost constant in the range of 30.5-31.0.

a) b)

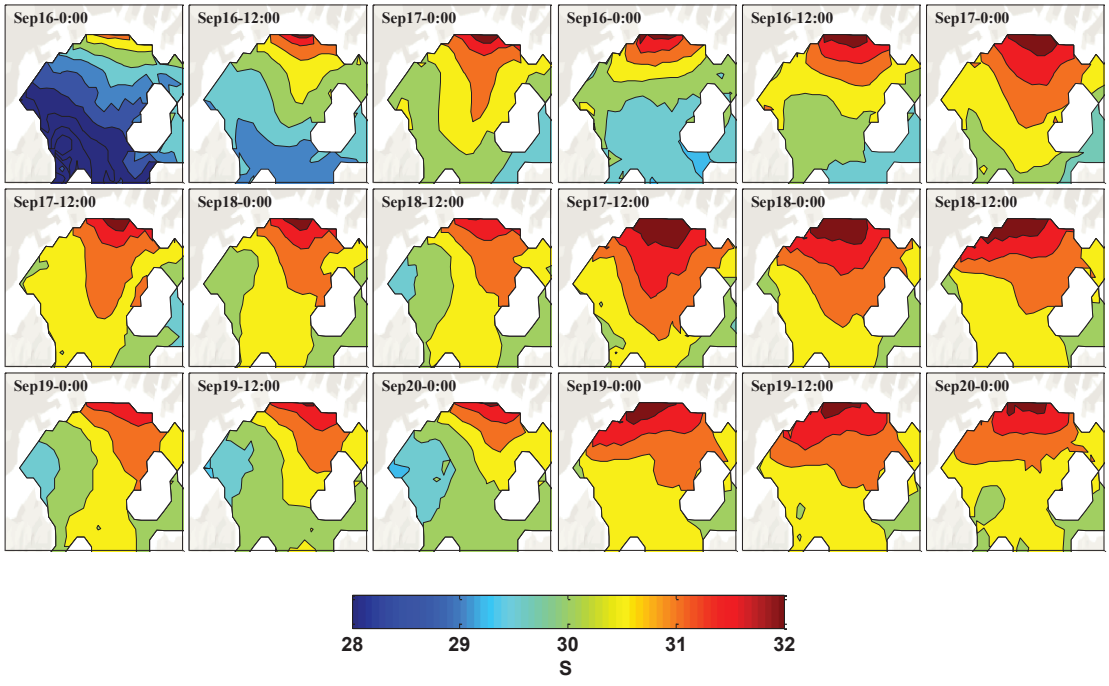

Fig. 3.4.3. The 12-hour interval variations of the 2-day filtered DA salinity, averaged for the upper (a) and lower (b) layers. A color-bar for salinity is provided at the bottom of the figure.

Volume transport of the subtidal current across a zonal transect EF is shown in Fig. 3.4.4 with time plots for the upper and lower layers. The negative (southward) transport for the upper layer began at 04:00 on September 16 and ended at 00:00 on September 18, reaching a maximum transport of 1580 $m^3s^{-1}$ at 04:00 on September 17. The positive (northward) transport for the lower layer began 6 hours after the start of the negative (southward) upper-layer transport and ended 2 hours after the upper-layer transport. The maximum lower-layer transport of 1550 $m^3s^{-1}$ was nearly equal to the maximum upper-layer transport of 1580 $m^3s^{-1}$. Immediately after the upwelling diminished, a reverse transport began in both the upper and lower layers (with a 2-hour delay for the lower layer) and ended at 00:00 on September 20. This suggests the sinking of upwelled water into the lower layer near the northern shore of the bay and the resulting return of offshore water in the upper layer. The maximum transport of the reverse flow was 970 $m^3s^{-1}$ for the upper layer and 640 $m^3s^{-1}$ for the lower layer, establishing a significant difference of 330 $m^3s^{-1}$.

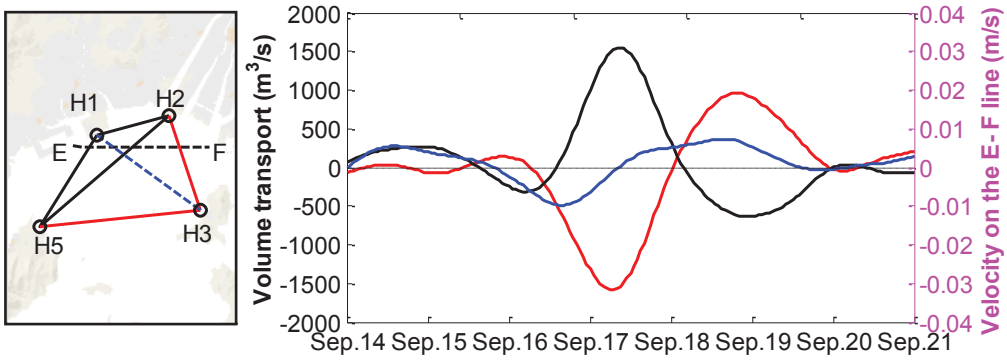


Fig. 3.4.4. Time plots of subtidal volume transport for the upper (red line) and lower (black line) layers across the transect EF. Transport difference between the upper and lower layers is shown by the blue line. The position of transect EF (horizontal dashed line) is depicted at the left of the figure.

Time plots of the 10-grid vertical profiles for the subtidal current and salinity averaged along the transect EF are shown in Figs. 3.4.5a and 3.4.5b respectively. During the upwelling period on September 17, the vertical profiles of the current formed a clear interface between the upper and lower layers at 5 m depth. In the next two days, the current reversed in both the upper and lower layers, deepening the interface from 5 m to 7 m. Furthermore, on September 16, saline water with S=31~31.5 in the lower layer outcropped at the surface, forming a steep slope of the S=31 contour line. At the beginning of September 19, the upwelled water began to sink, forming a gentle slope of this contour line.

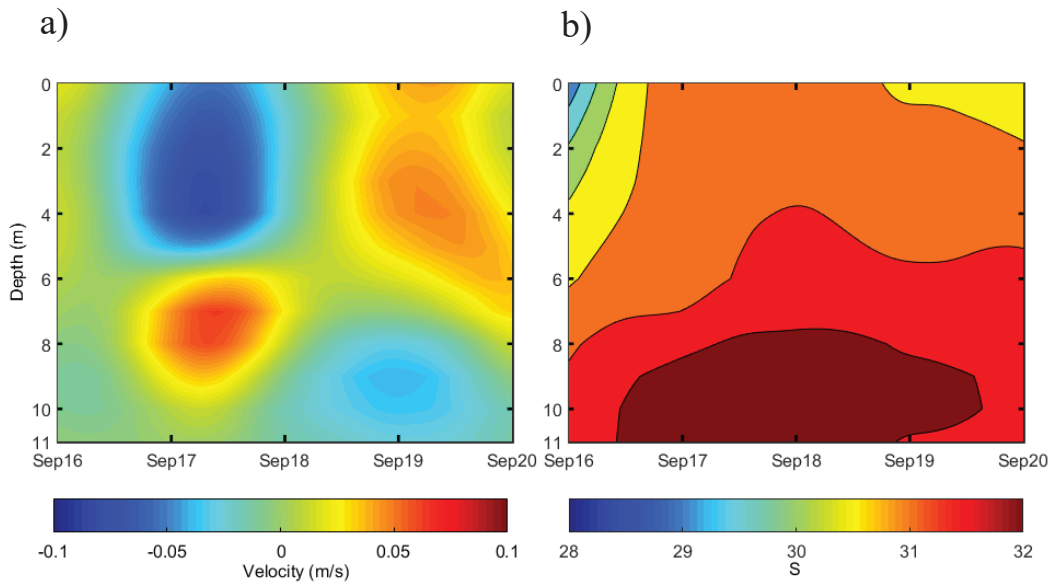


Fig. 3.4.5. Time plots of the 10-grid-point vertical profiles for (a) the subtidal current and (b) 2-day filtered salinity, averaged along transect EF.

## 3.5 Discussion

### 3.5.1 Transport continuity and mixing fractions

The coastal upwelling in Hiroshima Bay was triggered by a southward wind-driven current (subtidal current), generated in the upper layer and followed by a northward subtidal current in the lower layer. The southward lower-layer transport began with a delay of 6 hours from the northward upper-layer transport (Fig. 3.5.1). At the final stage of the upwelling with the wind decaying, the lower-layer transport diminished with a delay of 2 hours after the upper-layer current diminished. During the upwelling, the total volume ($V_A$=33,685 $m^3$) transported in the upper layer was nearly balanced by the total

lower-layer volume ($V_B$=33,275 $m^3$), generating only a small difference of 410 $m^3$. Thus, continuity was achieved for the water volume transported in the upper and lower layers. In addition, there was no significant effect of river discharge on the upwelling because the Ota River discharge was less than 80 $m^3s^{-1}$ throughout the observation period.

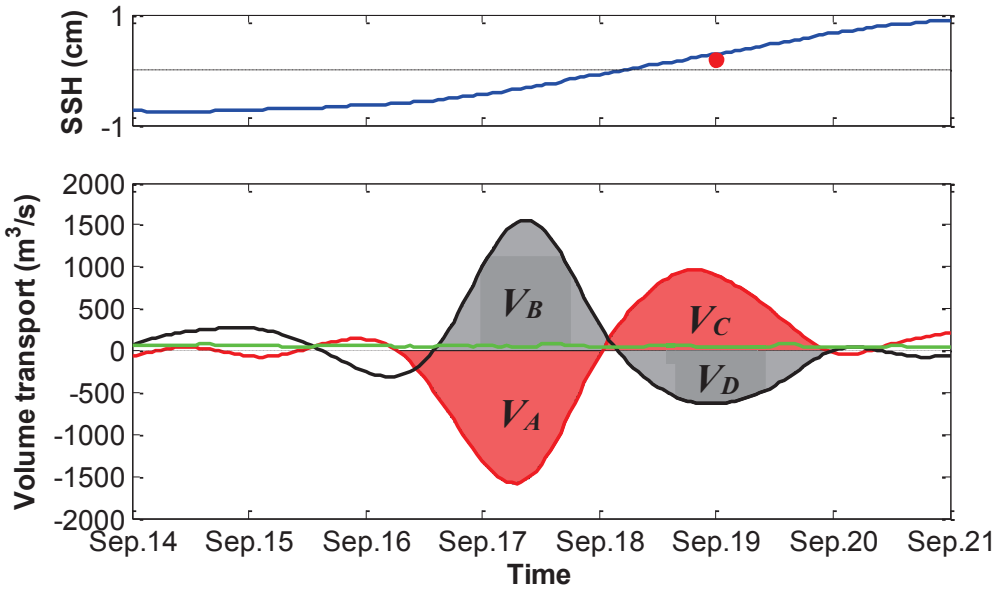


Fig. 3.5.1. Total water volume transports through the upper and lower layers across the transect EF (positive northward). $V_A$ and $V_C$ are the upper-layer transports for the upwelling and reverse-flow periods, respectively. $V_B$ and $V_D$ are the corresponding lower-layer transports. The green line shows the Ota river discharge at the Yaguchi gauge station. Temporal variation of the 2-day filtered SSH from the Hiroshima tide gauge station and SSH rise estimated from the excess volume around the northern shore are shown at the top of the figure with the blue line and red dot respectively.

In the upper layer, the total volume ($V_A$) transported southward during the upwelling

was not balanced by the total volume ($V_C$) transported northward during the reverse-flow period. It is likely that this transport reduction was caused by water mixing, (called offshore mixing), which occurred at the interface between the upper and lower layers. There was another mixing process generating an imbalance of the total upper-layer and lower-layer volumes ($V_C$ and $V_D$ respectively), transported during the reverse-flow period. The second mixing, (called nearshore mixing), may have been generated by the sinking of saline water from the upper to the lower layer. The mixing fractions are calculated by the following formulas:

$$\eta_1 = (V_A - V_C)/V_A \qquad (3.5.1)$$

$$\eta_2 = (V_C - V_D)/V_C \qquad (3.5.2)$$

where $V_A$=33,685 m$^3$ and $V_C$=25,484 m$^3$ are the total upper-layer volumes transported during the upwelling and reverse-flow periods, respectively. $V_B$=33,275 m$^3$ and $V_D$=17,937 m$^3$ are the total lower-layer volumes transported during the upwelling and reverse-flow periods, respectively. The offshore and nearshore mixing fractions were 24% and 30% respectively.

In the reverse-flow period from the beginning of September 18 to the end of September 19, the total upper- and lower-layer volumes transported across the transect EF were $V_C$=25,484 m$^3$ northward and $V_D$=17,937 m$^3$ southward. The excess northward transported volume increased the water storage in the domain between EF and the south coast of Hiroshima City. The resulting 0.20 cm water-level rise is roughly comparable to the 2-day filtered sea surface height (SSH) rise of 0.28 cm, provided by the Hiroshima

tide gauge station of the JCG.

### 3.6 Validation of the DA results

The path-average DA current and salinity, obtained along the sound transmission lines, are compared with the CAT data in Figs. 3.6.1 and 3.6.2 respectively. The DA currents were much larger than the POM currents and closer to the CAT data, except for the H1H2 data, demonstrating the effectiveness of data assimilation. The path-average DA salinities for H2H5 and H5H1 were in good agreement with the CAT data. The DA salinity data of H1H2, scattered around S=32, were a result of overestimation owing to the large distance from T1. The H3H5 data with weak SNRs deviated significantly from the DA salinity data. RMSEs calculated for the DA, CAT and CTD data are presented in Table 1. The averages of the hourly-mean current error were 0.061 $ms^{-1}$ for the SBR ray and 0.056 $ms^{-1}$ for the SR ray. These averages were much smaller than the maximum BTDA current, which oscillated in the range of 0.3 to 0.6 $ms^{-1}$. The averages of subtidal current errors were 0.018 $ms^{-1}$ and 0.014 $ms^{-1}$ for the SBR and SR rays, respectively, and smaller than the BCDA currents which were 0.10 $ms^{-1}$ for the upper layer and 0.08 $ms^{-1}$ for the lower layer.

The average of the hourly-mean salinity errors was 0.539 for the SBR ray and 0.455 for the SR ray. The average of the salinity errors, derived from subtraction of the hourly-mean DA salinity from the CTD data, was 0.680 for the upper layer and 0.881 for the

lower layer, larger than the aforementioned CAT salinity errors. The hourly-mean DA salinity overestimated the CTD salinity at H1H2. The salinity errors, except for H1H2, were lower than the salinity variation range of about 2.0 during the upwelling (see Fig. 3.6.2).

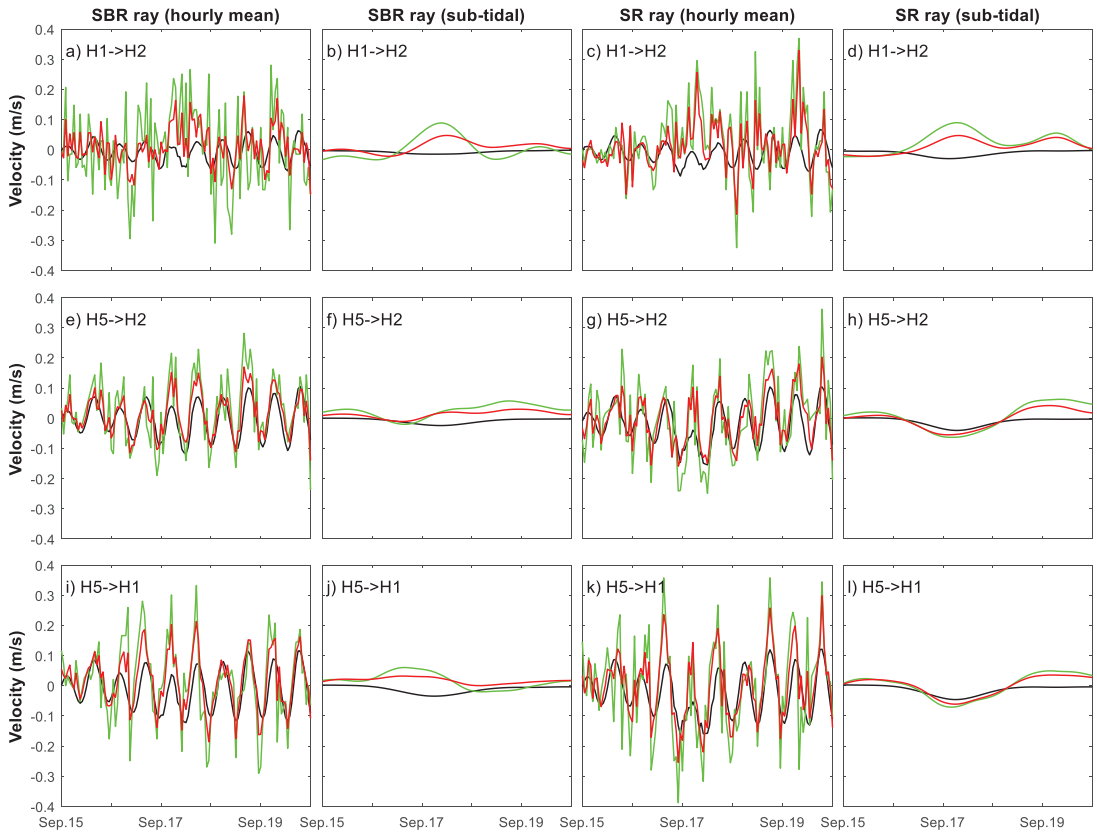


Fig. 3.6.1. Comparisons of the hourly-mean and subtidal path-average currents for the POM (black line), DA (red line) and CAT (green line) data at the three reciprocal sound transmission lines. Date tick marks at the bottoms of the figures indicate the beginning of each day.

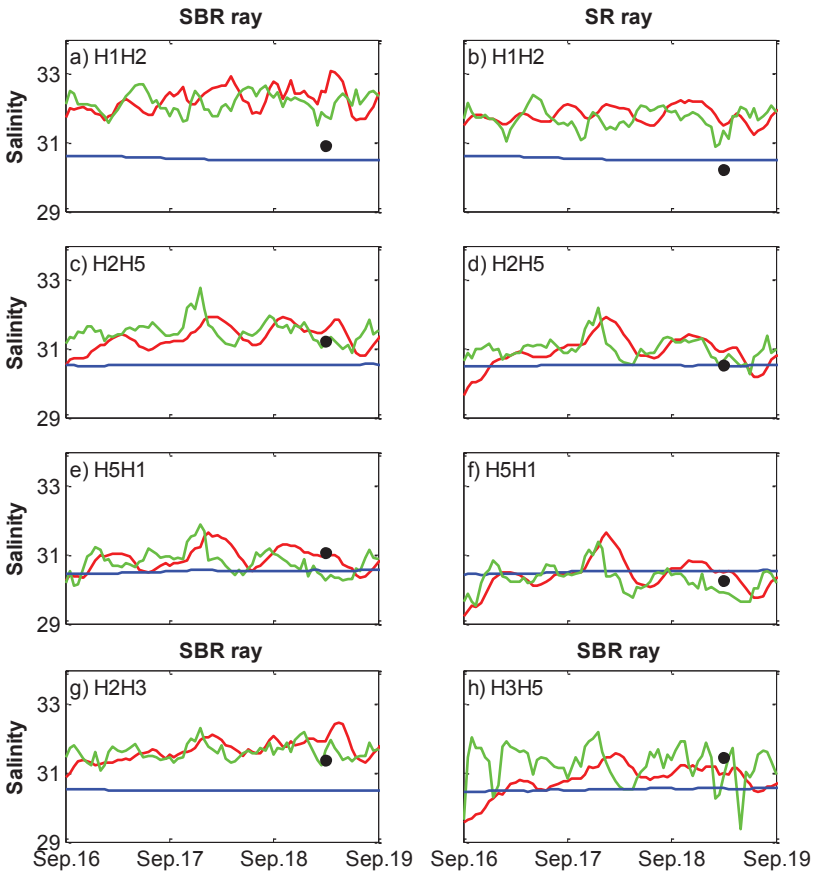


Fig. 3.6.2. Comparisons of the hourly-mean path-average salinity for the POM (blue line), DA (red line) and CAT (green line) results. Results for the SBR and SR rays are shown in (a) and (b) for H1H2, (c) and (d) for H2H5, and (e) and (f) for H5H1 respectively. The (g) and (h) panels are for the SBR rays at the one-way transmission lines H2H3 and H3H5, respectively. Black dots indicate the depth-average CTD salinities at the CTD cast times. Date tick marks at the bottoms of the figures indicate the beginning of each day.

Table 3.6.1. RMSEs for the hourly-mean and subtidal path-average DA and CAT currents. The hourly-mean depth-average DA salinities for the upper and lower layers are compared with the corresponding CTD results on September 18.

| RMSE | Current (path-average) [m/s] | | | | Salinity (path-average) | | Salinity (depth-average) | |
|---|---|---|---|---|---|---|---|---|
| | SBR ray | | SR ray | | SBR ray | SR ray | DA-CTD | |
| | Hourly mean | Sub tidal | Hourly mean | Sub tidal | Hourly mean | Hourly mean | Upper layer | Lower layer |
| H1H2 | 0.085 | 0.025 | 0.043 | 0.020 | 0.501 | 0.448 | 1.377 | 1.467 |
| H2H5 | 0.043 | 0.014 | 0.054 | 0.018 | 0.523 | 0.475 | 0.480 | 0.505 |
| H5H1 | 0.055 | 0.016 | 0.072 | 0.013 | 0.417 | 0.523 | 0.617 | 0.867 |
| H2H3 | – | – | – | – | 0.347 | – | 0.382 | 0.754 |
| H3H5 | – | – | – | – | 0.905 | – | 0.545 | 0.810 |
| Mean | 0.061 | 0.018 | 0.056 | 0.014 | 0.539 | 0.455 | 0.680 | 0.881 |

10-grid-point vertical profiles of the hourly-mean BCDA salinity are compared with the CTD data in Fig. 3.6.3. The BCDA salinity profiles overestimated the CTD salinities at C1 and C10 close to the northern shore and underestimated the CTD salinities at C5, C6, C7 and C8 southwest of the tomography domain. The assimilation of the fixed-point temperature array data for the whole domain produced misfits with the salinity at the CTD points located far from the temperature array. Note that the water was well homogenized from the surface to the bottom in the POM results.

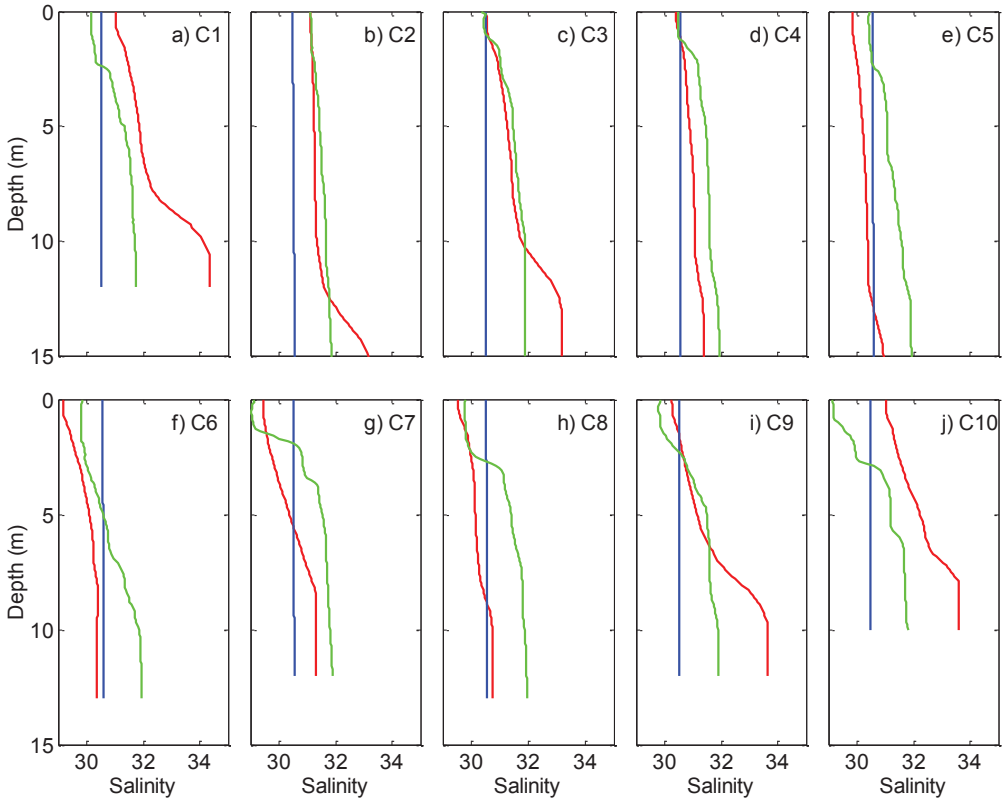


Fig. 3.6.3. 10-grid-point vertical profiles of the hourly-mean BCDA (red line) and POM (blue line) salinities compared with the 10-point CTD data (green line).

### 3.7 Summary

The CAT data, acquired in Hiroshima Bay on September 14-20, 2013 were assimilated into a full barotropic+baroclinic ocean model with 10 vertical grid nodes. The modified DA method significantly reduced computational time, based on the EnKF with model state vectors perturbed by time-invariant smooth pseudorandom fields. Travel-time data for the SBR and SR rays were respectively assimilated into the barotropic and baroclinic modes of the model. Travel-time differences were used to determine path-averaged

currents, and travel-time sums and one-way travel times were used to determine path-average salinity, by use of the sound speed formula and temperature array data. The 10-grid vertical-profile results of current and salinity were averaged over the upper 0-5 m depth layer and the lower depth>5 m layer to approximate a two-layer coastal upwelling system. The upwelling was generated in the northern part of Hiroshima Bay where the less saline water, discharged by the Ota River, spreads out in the upper 5 m.

During the upwelling, a subtidal southward-flowing current formed in the upper layer and a northward-flowing current in the lower layer, suggesting generation of upwelling near the northern shore of Hiroshima Bay from 00:00 to 12:00 on September 17. During the upwelling, salinity in the upper layer increased up to values equal to the lower-layer salinity. The upwelling was followed by a period of reverse flow with a northward subtidal current in the upper layer and a southward subtidal current in the lower layer. During upwelling, the total transported volume was balanced between the upper and lower layers, demonstrating this continuity of the upper- and lower-layer currents and the reliability of data assimilation. The total northward transported volume for the upper layer in the reverse-flow period was significantly smaller than the total southward transported volume for the upper layer in the upwelling period. Furthermore, the total northward transported volume for the upper layer was significantly larger than the total southward one for the lower layer in the reverse-flow period. These transported volume imbalances implied the existence of two types of water mixing: offshore mixing during the upwelling and nearshore mixing during the reverse-flow period. The mixing fractions, estimated

from the volume imbalances were 24% for the offshore mixing and 30% for the nearshore mixing. The offshore and nearshore mixings may have been respectively generated at the interface between the upper and lower layers and by the sinking of upper-layer water into the lower layer near the northern shore of the bay. By assimilating the CAT data into a full barotropic+baroclinic ocean model, mixing phenomena associated with the upwelling were better understood in the present study than in the previous one [Zhang et al., 2015].

The assimilated results were compared with path-averaged currents and salinities, calculated for the SBR and SR rays. The five sets of sound transmission data (three reciprocal and two one-way) for the SBR rays and three reciprocal transmission data for the SR rays were used to validate the barotropic and baroclinic results, respectively. The hourly-mean DA salinity was also compared with the CTD data, acquired on September 18. The average RMSEs for the DA and CAT currents in the subtidal data were 0.018 $ms^{-1}$ and 0.014 $ms^{-1}$ for the SBR and SR rays, respectively. The average RMSEs for the hourly-mean salinity were 0.539 for the SBR rays and 0.455 for the SR rays. The depth-average salinity errors for the DA and CTD data were 0.680 for the upper layer and 0.881 for the lower layer. The DA errors were significantly smaller than the variation ranges of current and salinity associated with the upwelling.

It is concluded that the process of coastal upwelling and the associated reverse flow, generated in the northern part of Hiroshima Bay, was adequately mapped using the assimilation of CAT data with travel times from two separate rays into the POM. Furthermore, the reliability of data assimilation is well validated from the continuity of

the upper- and lower-layer transports during the upwelling.

**References**

Blumberg A. F., G. L. Mellor (1987). A Description of a Three-Dimensional Coastal Ocean Circulation Model, in Three-Dimensional Coastal Ocean Models, edited by N. Heaps, pp. 1–16, AGU, Washington, D. C.

Evensen, G. (1994). Sequential data assimilation with a nonlinear quasi-geostrophic model using Monte Carlo methods to forecast error statistics. J. Geophys. Res., 99(C5), 10143-10162.

Evensen, G. (2003). The ensemble Kalman filter: Theoretical formulation and practical implementation. Ocean dynamics, 53(4), 343-367.

Gaillard, F. (1992). Evaluating the information content of tomographic data: Application to mesoscale observations. J. Geophys. Res., 97 (C10), 15489-15505.

Gaspari, G., and Cohn, S. E. (1999). Construction of correlation functions in two and three dimensions. Quart. J. Roy. Meteor. Soc.,125, 723–757.

Houtekamer, P. L. and Mitchell, H. L. (2001). A sequential ensemble Kalman filter for atmospheric data assimilation. Mon. Weather Rev., 129(1), 123-137.

Hunt, G. L. Jr (1995). Oceanographic Processes and Marine Productivity in Waters Offshore of Marbled Murrelet Breeding Habitat. USDA Forest Service Gen. Tech. Rep. PSW-152: 219-222.

Lin, J., Kaneko, A., Gohda, N. and Yamaguchi, K. (2005). Accurate imaging and prediction of Kanmon Strait tidal current structures by the coastal acoustic tomography data, Geophys. Res. Lett., 32, L14607, doi:10.1029/ 2005GL022914.

MacKenzie, K. V. (1981). Nine-term equation for sound speed in the oceans. J. Acoust. Soc. Am., 70(3), 807-812.

Mellor, G. L. (2002). Users Guide for a Three-Dimensional, Primitive Equation, Numerical Ocean Model, Princeton Univ., Princeton, N.J., 1992.

Munk, W. and Wunsch, C. (1979). Ocean acoustic tomography: A scheme for large scale monitoring. Deep-Sea Res., 26A, 123-161.

Munk, W., Worceser, P. F. and Wunsch, C. (1995). Ocean Acoustic Tomography, 433 pp., Cambridge Univ. Press, Cambridge, U. K.

Nguyen, H., Kaneko, A., Lin, J., Yamaguchi, K., Gohda, N. and Takasugi, Y. (2009). Acoustic measurement of multi sub-tidal internal modes generated in Hiroshima Bay, Japan, IEEE J. Oceanic Eng., 34(2), 103-112.

Park, J.-H. and Kaneko, A. (2000). Assimilation of coastal acoustic tomography data into a barotropic ocean model. Geophys. Res. Lett., 27(20), 3373-3376, doi:10.1029/ 2000GL011600.

Taylor, C. B. and Stewart, H. B. Jr. (1959). Summer upwelling along the east coast of Florida, J. Geophys. Res., 64(1), 33-40.

Thomson, R. E. (1981). Oceanography of the British Columbia Coast, 281 pp., Minister

of Supply and Services, Canada.

Yamaguchi, K., Lin, J., Kaneko, A., Yamamoto, T., Gohda, N., Nguyen, H.-Q. and Zheng, H. (2005). A continuous mapping of tidal current structures in the Kanmon Strait, J. Oceanogr., 61(2), 283-294.

Yamaoka, H., Kaneko, A., Park, J.-H., Zheng, H., Gohda, N., Takano, T., Zhu, X.-H. and Takasugi, Y. (2002). Coastal acoustic tomography system and its field application, IEEE J. of Oceanic Eng., 27(2), 283-295.

Zhang, C.-Z., Kaneko, A., Zhu, X.-H. and Gohda, N. (2015). Tomographic mapping of a coastal upwelling and the associated diurnal internal tides in Hiroshima Bay, Japan, J. Geophys. Res., 120(6), doi:10.1002/2014JC010676, 4288-4305.

Zhu, X.-H., Kaneko, A., Wu, Q., Zhang, C.-Z., Taniguchi, N. and Gohda, N. (2013). Mapping tidal current structures in Zhitouyang Bay, China, using coastal acoustic tomography, IEEE J. Oceanic Eng., 38(2), 285-296.

Zhu, X.-H., Zhang, C.-Z., Wu, Q., Kaneko, A., Fan, X. and Li, B. (2012). Measuring discharge in a river with tidal bores by use of the coastal acoustic tomography system, Estuarine, Coastal and Shelf Sci., 104: 54-65.

# CHAPTER Ⅳ BALI STRAIT STUDY

## 4.1 Introduction

The Bali Strait, located between Java and Bali, is connected to the Java Sea through a narrow northern inlet of width about 2 km, which broadens southward in a trumpet shape toward the outlet to the Indian Ocean. The northern part with channel widths of about 5 km is characterized by a strong tidal current, which makes the scheduled operation of ferry boats difficult. However, in spite of the societal importance of the current distribution and variation, cross-strait profiling measurement of the current and temperature has never been attempted in the strait.

Coastal acoustic tomography (CAT) has been well developed as a coastal sea application of ocean acoustic tomography [Munk, et al.,1995; Zheng, et al., 1997; Park and Kaneko, 2000]. Intensive field measurements by CAT have been performed in coastal seas around Japan [Yamaoka, et al., 2002; Yamaguchi, et al., 2005; Zhang, et al., 2015] and China [Zhu, et al., 2013]. CAT-based reciprocal sound transmission, which has often been applied to narrow straits, provides an observational method suited to profiling measurement in the Bali Strait [Send, et al., 2002; Adityawarman, et al., 2012; Zhang, et al., 2016; Zhu, et al., 2015].

In this chapter, the cross-strait layered structure and the temporal variation of the current and temperature in the Bali Strait are investigated by reciprocal sound transmission using vertical-slice inversion and data assimilation. Semi-diurnal internal

tides and the associated higher-frequency phenomena are the main targets of the experiment.

## 4.2 Experiments

### 4.2.1 First experiment

The first reciprocal sound transmission experiment was carried out over three days (June 10-13, 2015 in local time) in the northern part of the Bali Strait, characterized by a strong tidal current. Land-based CAT systems were located on both sides of the strait (Fig. 4.2.1). Station B2 on the Bali side was sited at an abandoned platform of a natural gas pipeline 60 m offshore from the coast, and station B3 on the Java side was at the edge of a jetty in a resort hotel. The distance between B2 and B3 was 4,461 m, determined from the global positioning system (GPS) and conductivity-temperature-depth (CTD) correction [Zhang, et al., 2016]. The seafloor depth is about 27 m at B2 and 5 m at B3. There is a submarine trough with a maximum depth of 79 m at a distance of 1 km from B2 and the seafloor forms a gentle slope toward B3 from the trough. A 10-kHz broadband transducer (International Transducer Corporation ITC-3013) was set to about 10 m below the surface by a rope at B2 and the transducer was 2 m below the surface at B3. A 10-kHz carrier modulated by one period (4095 digits=1.2285 s) of the $12^{th}$ order M sequence was transmitted simultaneously from both transducers every 3 min. By cross-correlating received signals with the M sequence used in the transmission, the signal-to-noise ratio

(SNR) of the received signals was markedly increased by $10\log(2^{12}-1)=36.1$ [dB] on the basis of error theory.

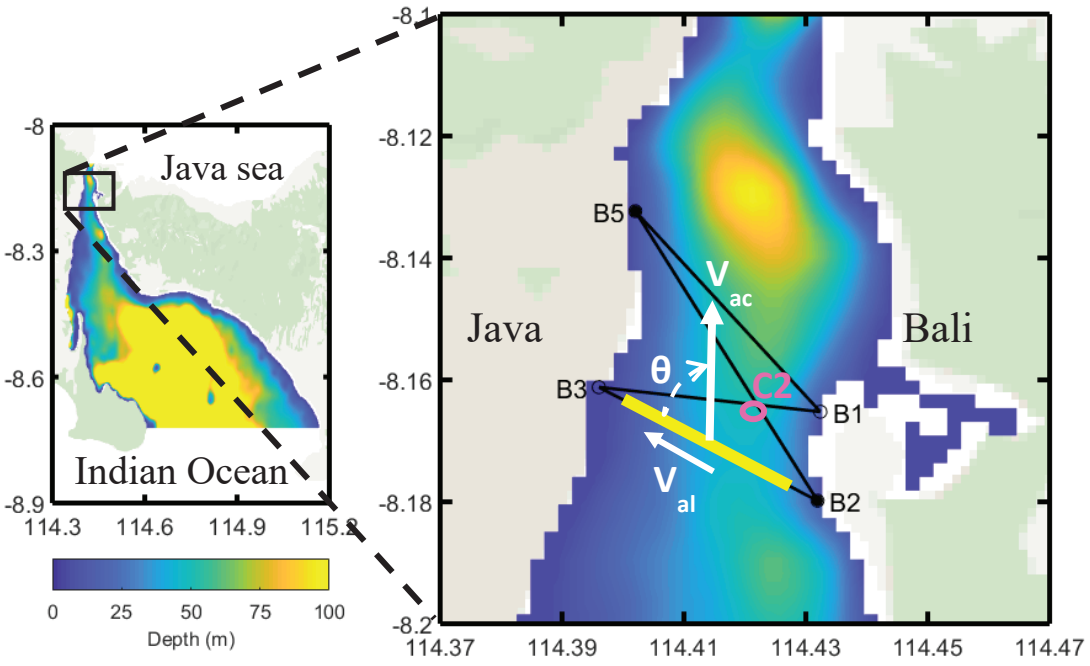


Fig. 4.2.1 (Left) POM simulation domain with bathymetry chart, and (right) the CAT station array at a magnified scale. In the right figure, four CAT stations (B1, B2, B3 and B5) are indicated with black circles. In first experiment, only B2 and B3 stations were operated. The along-channel current $V_{ac}$ is roughly directed to the north at an angle of $\theta=63^{\circ}$ clockwise from the along-line (path-averaged) current $V_{al}$ on the sound transmission line B2B3. C2 is the CTD point labelled with a pink dot. In second experiment, all four stations were operated. The dots at B2 and B5 show stations equipped with pressure sensors. The black lines connecting the stations are the reciprocal sound transmission lines.

By dropping a CTD package from a ship into the water, the conductivity and temperature were recorded with increasing depth. Two sets of CTD data, obtained on Mar. 19, 2014 and Jun. 11, 2015 at C2, close to the sound transmission line B2B3, were used in this study. HORIBA W-20XD CTD sensors were used in 2014 and SonTek-CastAway sensors were used in 2015. The maximum observable depth of the CTD casts was 79 m in 2014, but was only 45 m in 2015 owing to a strong southward tidal current. The CTD data allowed us not only to understand the density environment but also to know the sound speed field for acoustic ray simulation. Because of the greater maximum depth, the 2014 data were as below used to obtain a reference sound speed for the following ray simulation and inverse analysis.

### 4.2.2 Second experiment

The second CAT experiment with four acoustic stations (B1, B2, B3 and B5 in Fig. 4.2.1) was performed on June 1 to 3, 2016 (local time) for further investigating 3D current structures of the Bali Strait. All acoustic stations transmitted every minute 10-kHz sound, modulated by three periods of $10^{th}$ order M-sequence. Reciprocal transmission data were obtained for four lines (B1B3, B1B5, B2B3 and B2B5) because sound transmission along B3B5 and B1B2 was prohibited by the protruded shorelines. A pressure sensor was attached on the suspension rope above the transducer at B2 and B5 to observe sea level variation during the CAT experiment. Accurate sea level data were obtained at B2 while

B5 data were polluted by swings of rope with a transducer due to strong tidal currents. The accuracy of model and data assimilation was validated by comparing the simulated and observed tides at B2.

## 4.3 Methods

### 4.3.1 Data processing

#### 1) Quality check of received data

In the 2015 experiment, noisy data were acquired especially at B2, so the following quality check of the data was adopted to increase the SNR of the received data.

**Step 1**: Sequential correlation patterns, are summed over 30 min to increase the SNR of the correlation data where the SNR is defined with a non-dB scale as the ratio of the peak height to the mean height of the received data. As a result, the SNR is slightly underestimated because signal peaks are included in calculation of the noise level.

**Step 2**: Arrival peaks are identified in the correlation patterns summed over 30 min. The largest arrival peak is first determined on the basis of the comparison with thresholds of SNR (the first threshold) and is defined as the first arrival peak above the threshold. Although the first and largest arrival peaks are not always coincident, pick-up errors of the first arrival peak are reduced through the summation over 30 min. Further study is required for the acoustical identification of the first arrival peak. The second arrival peak

is found in the range of 1-5 ms after the first peak, using the thresholds of SNR (the first threshold). These SNR thresholds are taken to select good reciprocal data of the sufficient numbers. The selection of higher SNR thresholds increases the number of missing data. By considering the acceptable data quality and number, SNR values for the first thresholds are determined by trial-and-error.

**Step 3**: The semi-hourly range-averaged current $V_m$ and temperature $C_m$ are calculated from the differential travel time $\Delta t$ and mean travel time $t_m$, respectively, using Eqs. (4.3.1) and (4.3.2) for both the first and second arrival peaks. The hourly mean data are constructed through a one-hour moving average of the 30-min data. The hourly-mean $C_m$ is converted to $T_m$ under fixed salinity ($S$=34 in the practical salinity unit used conventionally) and layer depths using the sound speed formula [MacKenzie, 1981]. Data with an hourly-mean range-averaged current greater than 2 $ms^{-1}$ (the second threshold) and the corresponding sound speed are removed as unnatural data. Data in regions with missing data are produced by linear interpolation of neighboring data.

$$V_m = \frac{C_0^2}{2L}\Delta t \quad (4.3.1)$$

$$C_m = \frac{L}{t_m} \quad (4.3.2)$$

Here, $C_0$ is the reference sound speed, usually taken as the average sound speed at the observation site, and is nearly equal to $C_m$. The $t_m$-derivative of Eq. (4.3.2) under a fixed $L$ becomes

$$\Delta C_m = -\frac{C_0^2}{L}\delta t_m \quad (4.3.3)$$

Where $\Delta C_m$ is the deviation of the sound speed from $C_m$ and $\delta t_m$ is the deviation from the reference mean travel time $L/C_0$.

**Step 4**: $V_m$ and $\Delta C_m$ for good quality data are converted to the travel time difference $\Delta t$ and the mean travel time deviation $\delta t_m$ for the first and second arrival peaks using Eqs. (4.3.1) and (4.3.3), respectively.

**Step 5**: The inverse analysis of the range-averaged current and temperature for five horizontal layers is performed using the accurate data of $\Delta t$ and $\delta t_m$ for the first and second arrival peaks.

**2) Error Evaluation**

We here evaluate the observation errors. The first observation error for the current and sound speed (denoted as $V_e$ and $C_e$, respectively) are determined from the one-digit length of the M sequence $t_r$, which is the time resolution for multi ray arrival. $(V_e,\ C_e)$ are obtained by replacing $t_r$ by the differential travel-time $\Delta t = t_r$ and the mean travel time $\delta t_m = t_r$ in Eqs. (4.3.1) and (4.3.3), respectively.

$$(V_e,\ C_e) = \frac{C_0^2}{2L}(\Delta t,\ 2\delta t_m) \quad (4.3.4)$$

Here $C_0$ is the reference sound speed and *L* is the station-to-station distance [Zhang, et al., 2016]. For a modulation number of three cycles per digit, $t_r = 3/10{,}000 = 0.3$ ms.

For L=4,461 m and $C_0 = 1{,}500$ ms$^{-1}$, $V_e = 0.076$ ms$^{-1}$ and $C_e = 0.152$ ms$^{-1}$.

The first observation errors are found in the travel time variations at frequency ranges shorter than 1 h$^{-1}$ [Yamaoka, et al., 2002; Zhu, et al., 2015]. The root mean square (RMS) variations of the travel time difference and the summation in the range of (3 min -1 h) are taken into consideration as the second observation errors. Then these RMS travel time errors ($\Delta t_e = \Delta t$ and $\delta t_e = \delta t_m$) were converted to the current velocity error $\overline{V_e}$ and sound speed error $\overline{C_e}$, respectively, using Eq. (4.3.4). Error evaluation was performed for both the first and second peaks and the results are presented in Table 4.3.1. $\overline{V_e}$ and $\overline{C_e}$ were 0.106 and 0.108 ms$^{-1}$ for the first peak, and 0.076 and 0.088 ms$^{-1}$ for the second peak, respectively. These RMS errors were in rough agreement with the one-digit errors (the first observation errors).

Table 4.3.1 RMSEs of the travel time difference $\Delta t$ and travel time sum $\delta t$ accompanied by the 1-h- and 2-day-average errors of current $\overline{V_e}$, sound speed $\overline{C_e}$ and temperature $\overline{T_e}$.

| | | $\Delta t_e$ (s) | $\delta t_e$ (s) | $\overline{V_e}$ (ms$^{-1}$) | $\overline{C_e}$ (ms$^{-1}$) | $\overline{T_e}$ (°C) |
|---|---|---|---|---|---|---|
| RMS observation error | 1st arrival | 0.00042 | 0.00043 | 0.106 | 0.108 | 0.046 |
| | 2nd arrival | 0.00030 | 0.00035 | 0.076 | 0.088 | 0.037 |

From the dependence of temperature on sound speed in the sound speed formula

[Taniguchi, et al., 2013], $\overline{C_e}$ was converted to the temperature error $\overline{T_e}$ using [Zhang, et al., 2015]:

$$\overline{C_e} = 2.37\overline{T_e} \quad (4.3.5)$$

with the average values $T_0$=25.3 ℃, $S_0$=34, and $D_0$=30 m obtained in the Bali Strait.

### 4.3.2 First experiment

#### 1) Received data

The original 3-min data (green circles) and 30-min summed data (red circles) are compared in Fig. (4.3.1) for a typical observation period from 14:00 to 14:12 on June 12, 2015. The summation enabled us to construct peak heights larger than the pre-summation ones for both the B2 and B3 data. In both the original and summed data, the first (largest) peak heights for B2 were significantly smaller than those for B3. Furthermore, the missing data in the fifth non-sum data of B2 were reproduced by the 30-min sum. This problem of missing data did not occur in the B3 data.

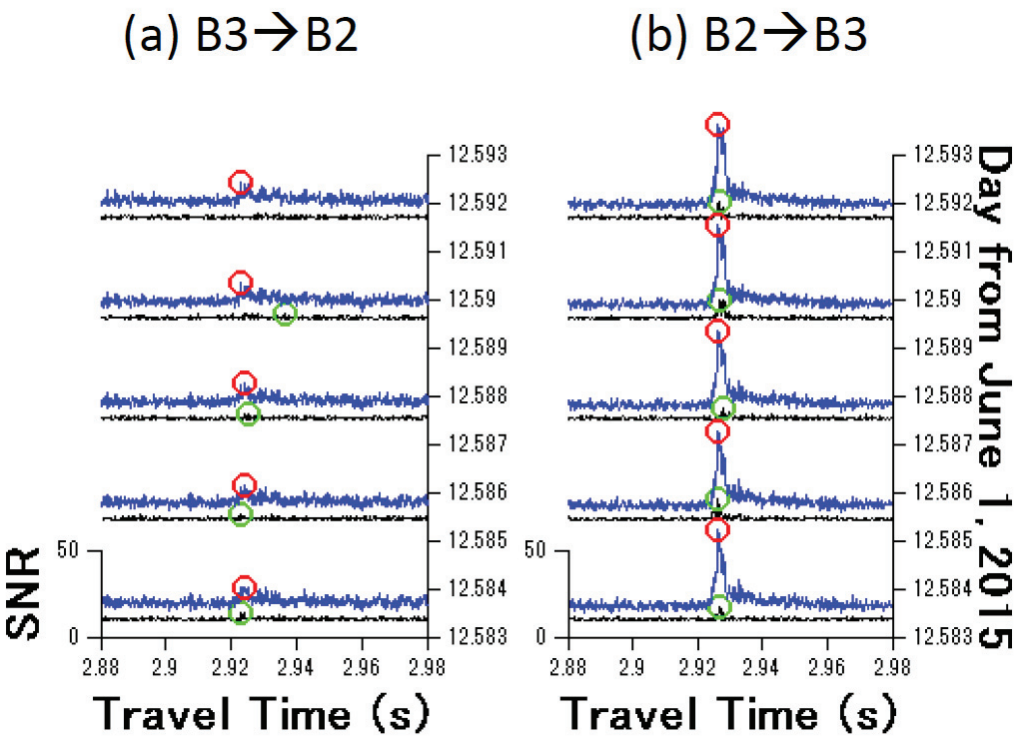


Fig. 4.3.1 Comparison of typical stack diagrams obtained in the period from 14:00 to 14:12 on June 12, 2015 to show the significant effect of taking a 30-min sum. The black and blue lines show examples of correlation patterns in the cases of not taking a sum and taking a 30-min sum, respectively. The largest (first) arrival peaks are highlighted with red and green circles for the cases of 30 min sum and no sum, respectively. (a) The left illustration is for B2 and (b) the right one is for B3.

The first and second arrival peaks identified in the correlation pattern by SNR>18 and SNR>16 for B2, SNR>20 and SNR>20 for B3 (the first threshold) are plotted in Fig. (4.3.2) with red and green circles, respectively, for one received data pre-summation (left illustration) and for the whole of the observational data post-summation (right

illustration). In the pre-summation, the SNR for the first peak was 4.2 for the B2 data and 6.8 for the B3 data. Although the SNR was markedly increased by summing over 30-min, the first and second arrival peaks still exhibited scatter, implying the presence of significant errors.

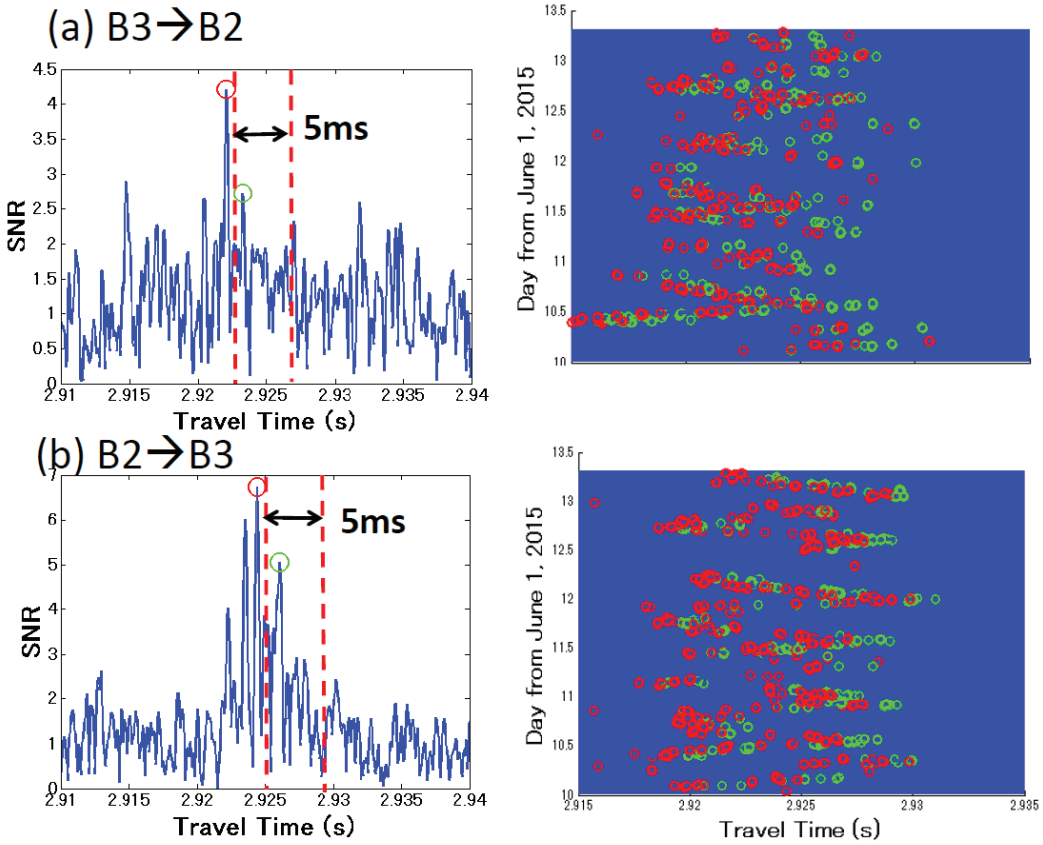


Fig. 4.3.2 (left) Typical examples of the pre-summation correlation pattern obtained at 02:30 on June 12. The second arrival peak is identified in the range of 1-5 ms, bounded by two red broken lines after the first arrival peak. (right) Stack diagrams of the 30-min-sum correlation pattern with the first and second arrival peaks (red and green circles, respectively) obtained at (a) B2 and (b) B3. Individual correlation patterns are not visible owing to the narrow-space drawing of sequential correlation patterns.

**2) Path-average current**

Temporal variations of the hourly-mean and 2-day-mean path-average current and temperature are shown in Fig. (4.3.3) with the red and blue lines for the first and second arrival peaks, respectively. The hourly-mean data oscillated with a period of about 8 h for both the first and second peaks with the amplitude decreasing with time. The 2-day-mean data remained nearly constant around -0.3 $ms^{-1}$ for the current and 22.0 ℃ for the temperature. The average differences between the first and second peaks were 0.2 $ms^{-1}$ for the current and 0.2 ℃ for the temperature.

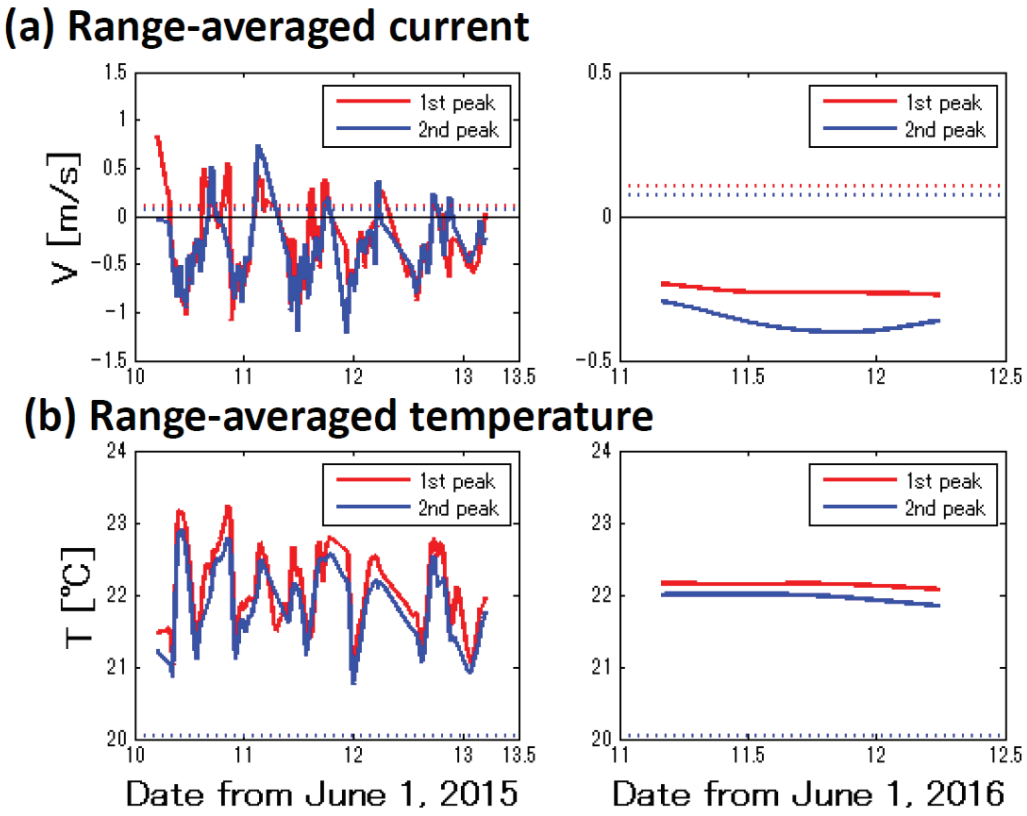


Fig. 4.3.3 Temporal variations of the path-average (a) current and (b) temperature. Data

for the first and second arrival peaks are shown with the red and blue lines, respectively. The left and right illustrations are for the hourly- and 2-day-mean data, respectively. RMS observation errors are drawn with horizontal dotted lines for the first and second peaks using the same colors as the path-average data. The temperature errors for the first and second peaks overlap owing to their small differences.

**3) Ray simulation and vertical-slice inversion**

The results of a range-independent ray simulation based on the sound-speed profile from the 2014 CTD data are shown in Fig. (4.3.4). The first arrival peak corresponds to the refracted-bottom reflected ray (red ray), called "Ray-1" and the second arrival peak ("Ray-2") corresponds to a surface-bottom reflected ray (green ray). The travel time and ray length are 2.9186 s and 4462.8 m for Ray-1 and 2.9223 s and 4473.2 m for Ray-2, respectively. Ray-1 travels near the seafloor, forming upper turning points deeper than Ray-2. Ray-1 and Ray-2 follow distinct paths in the 1.3-3.8 km range from B2. However, Ray-1 and Ray-2 travel only in the first (deepest) layer around 1 km from B2, forming a bad effect in the layered inversion. The information along the two rays traveling at different depths in the ranges of 0-0.6 km and 1.3-3.8 km from B2 was used to reconstruct the layered structure of the currents and temperature deviations. The vertical-slice inversion, which was proposed in geo-tomography [Rajan, et al., 1987] and used to profile the Kuroshio Current east of Taiwan [Taniguchi, et al., 2013], can also be applied to the

Bali Strait. The details were explained in chapter 2.

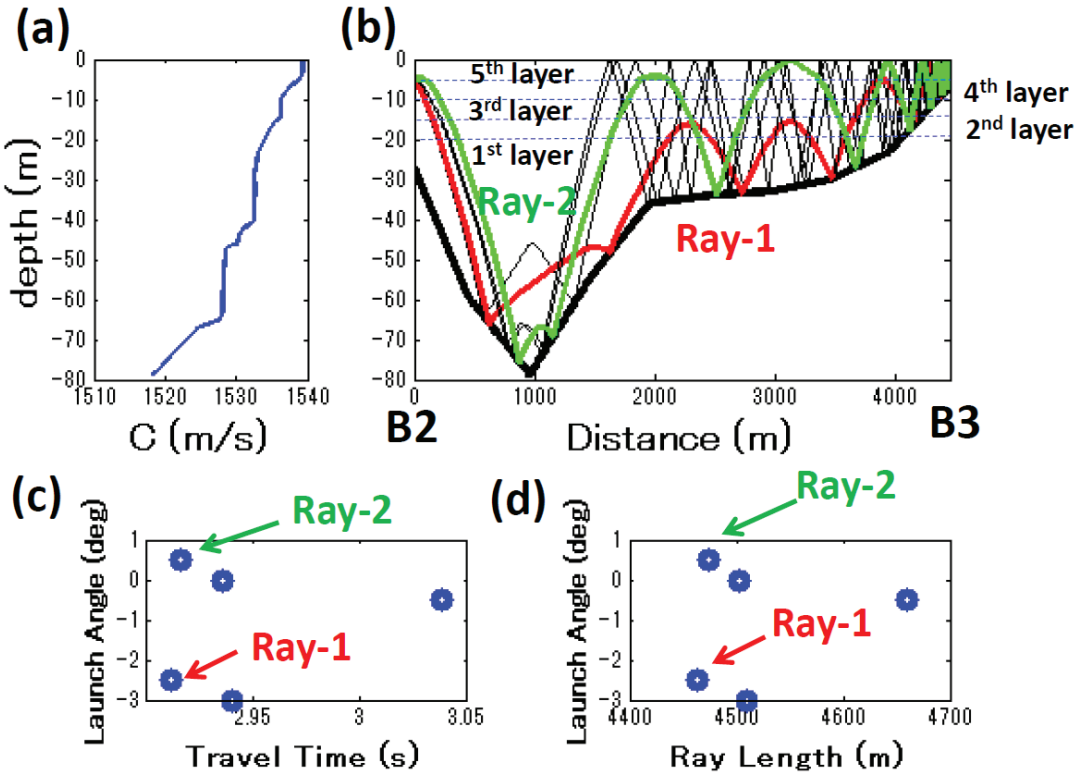


Fig. 4.3.4 Results of a range-independent ray simulation. The vertical profile of the reference sound speed is shown in (a). Ray-1 and Ray-2 are indicated with thick red and green lines in (b), respectively. The simulated travel time (c) and ray length (b) are plotted against the launch angle of sound from the horizontal at B2.

### 4.3.3 Second experiment

#### 1) Data processing

The first three steps for quality check were also applied to identify the first arrival peak in the second experiment. The first threshold of SNR>30 was used to determine the largest arrival peak for all station pairs. The second threshold was further adopted for all stations

to remove unnaturally large path-average current over 2 $ms^{-1}$. Finally, the data gap was filled by linear interpolation for each transmission line.

The largest arrival peaks identified reciprocally for four transmission lines through three-step quality check were shown in Fig. 4.3.5. The largest arrival peaks were always the first arrival peaks. The first arrival peaks were successfully identified in the period from 08:00 on June 1 to 11:00 on June 3 although data number were significantly decreased for the station pairs B1B5 and B2B5 related to B5. Semidiurnal variations were visible in all the figures, forming pronounced oscillation especially for B1→ B3 and B2→ B3.

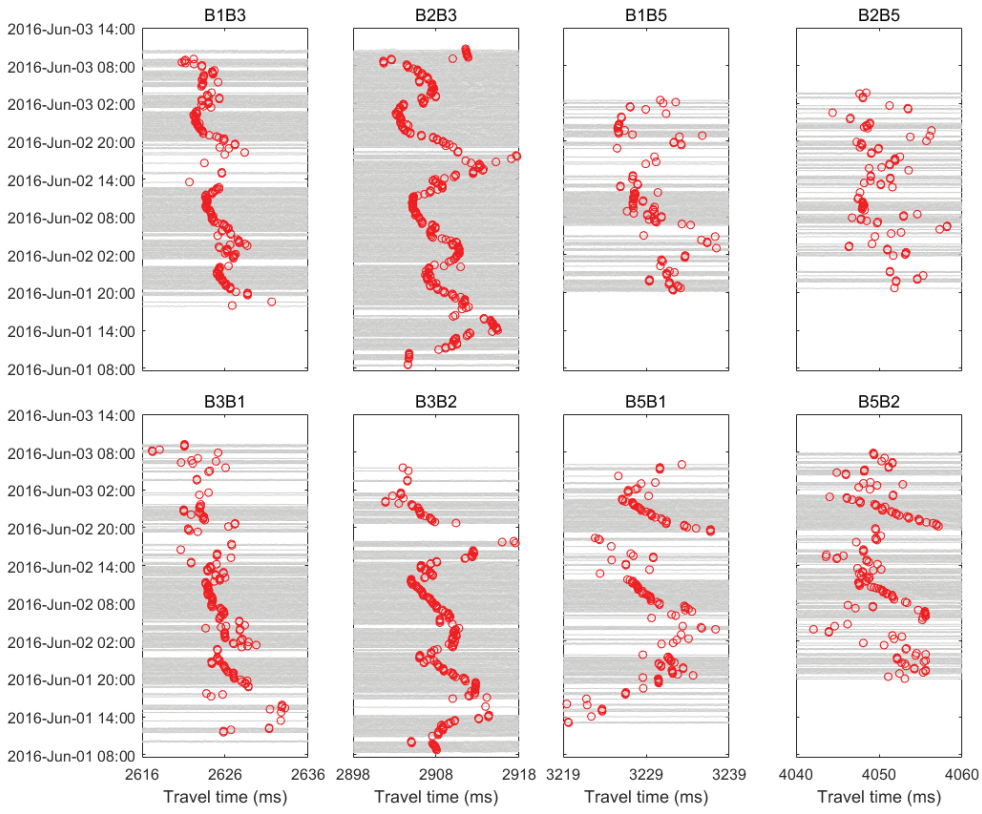


Fig. 4.3.5 The largest arrival peaks plotted with time proceeding upward.

**2) POM**

The ocean model used in Bali Strait study is barotropic POM with tidal forcing. The simulation domain is shown in the left panel of Fig. 4.2.1. The horizontal grid size is 250 m for both east-west and north-south direction. The open boundaries are set at the northern and southern edges of domain. Tidal forcing is given at southern boundary which faces to the Indian Ocean. Radiation condition that current passes without any constraints through the northern open boundary is applied there. Sea level data are provided by Tidal Model Driver (TMD) which is a global model product of ocean tides. Refer to Egbert, et al. [1994] and further Egbert and Erofeeva [2002] for detailed information of TMD. The POM simulation started on May 24 and continued for 12 days up to June 4 covering the CAT experiment period. The first 7 days were regarded as a spin-up period for correct simulation. RMSE for the simulated and observed sea levels at B2 was 0.16 m less than 10% of sea level range.

**3) Ray simulation and Data assimilation**

From the range-independent ray simulation result (Fig. 4.3.6) based on the sound-speed profile from the 2014 CTD data, the first arrival peaks corresponded to rays crossing the whole depth from surface to seafloor. Thus, current sampled by these rays was mainly barotropic current. Hence, hourly mean path-average current calculated from these largest arrival peaks were processed by a 6-hour low pass filter (LPF) to remove high-frequency phenomena and the resulting currents were assimilated into

barotropic POM using the barotropic data assimilation scheme introduced in chapter 2. Barotropic assimilation started from 15:00 on June 1 and ended to 08:00 on June 3 considering the acquisition period of CAT data. At the starting period from 15:00 on June 1 to 23:00 on June 1, assimilation data were ones obtained at only B2B3 data. The B1B3 data joined newly the assimilation at 00:00 on June 2. By the addition of other two-line data at 03:00 on June 2, four-line data assimilation continued to 05:00 on June 3. After that, only B1B3 data were assimilated from 05:00 on June 03 to 08:00 on June 03.

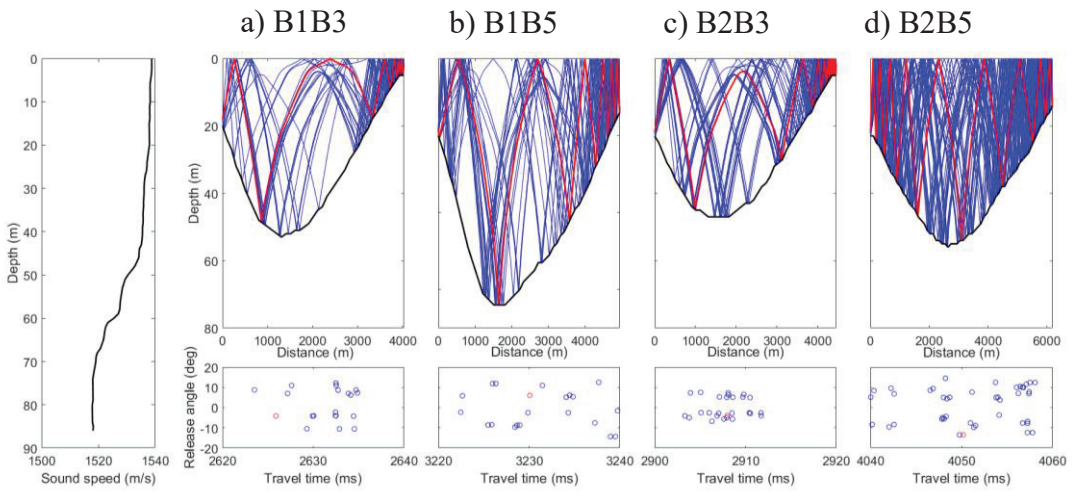


Fig. 4.3.6. Results of range-independent ray simulation along four reciprocal transmission lines B1B3, B1B5, B2B3 and B2B5. Red lines show rays with the simulated travel times nearest to the average travel time for the observed, largest arrival peak. Red dots indicate the simulated travel times corresponding to the red rays.

In barotropic assimilation scheme, the decorrelation length $\gamma_h$ of pseudorandom noises was set to 5 km equated to the width of the Bali Strait. The optimal ratio of *P/R* was

determined to be 25 from Fig. (4.3.7) in which RMSEs for the DA and CAT path-average currents were plotted against $\gamma$. The RMSEs showed no more decrease when *P/R* increased up to 25 for all cases. RMSE for DA and CAT path-averaged currents was 0.08 m/s for B1B3, 0.16 m/s for B1B5, 0.11 m/s for B2B3 and 0.12 m/s for B2B5. The smooth correlation function $\lambda$ which localizes data assimilation effect was set to 0.6 at B5, the farthest position from tomography center (Fig. 4.3.8). This setting was learned from Hiroshima Bay data assimilation experience that the best result was obtained when $\lambda$ took 0.6 at the farthest point from the tomography center.

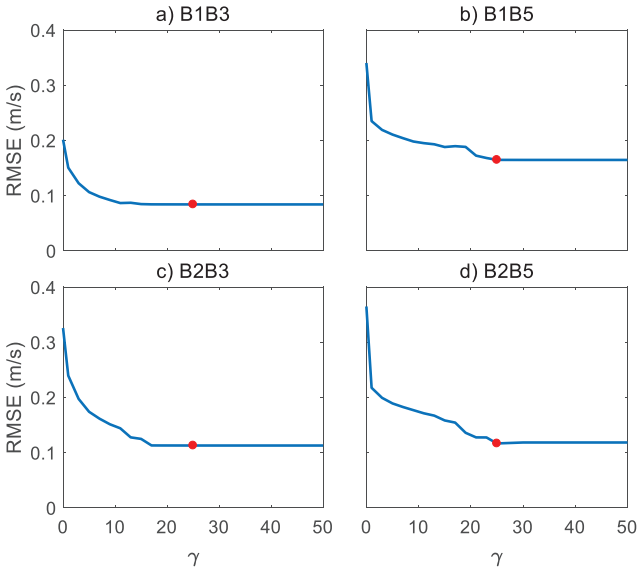


Fig. 4.3.7 RMSEs for DA and CAT path-average currents plotted against $\gamma = P/R$. The red dots indicate RMSE values at $\gamma = 25$.

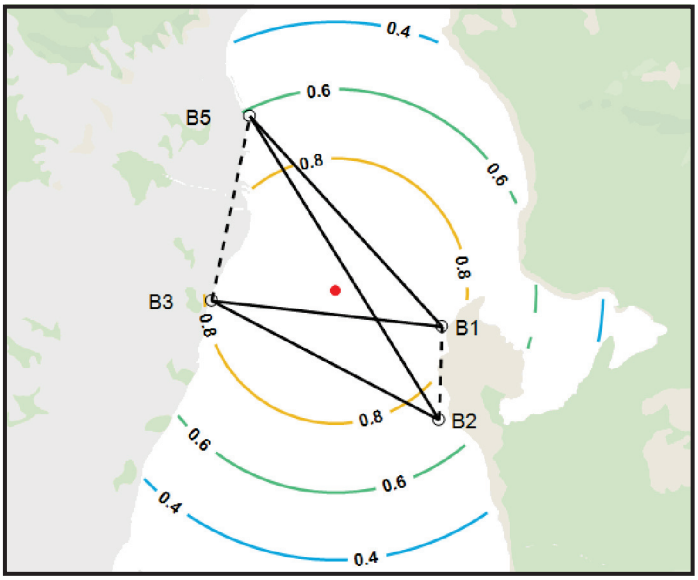


Fig. 4.3.8 Contour plot of $\lambda$ represented as concentric circles with a center (red dot) and contour interval 0.2.

## 4.4 Results

### 4.4.1 First experiment

The five-layer structures of the hourly mean current are shown with the temporal plots in Fig. 4.4.1. Nonlinear internal tides with higher frequencies, superimposed on semi-diurnal internal tides, were visible in all layers with an amplitude range of 1.0-1.5 $ms^{-1}$. The current variations were out-of-phase between the upper three layers (V3, V4, and V5) and the lower two layers (V1 and V2) as shown with the dotted vertical lines. The five-layer hourly-mean temperatures oscillated with amplitudes of about 1.5 ℃ for the middle two layers (T2 and T3) and about 1.0 ℃ for the upper two layers (T4, T5) and the deepest layer (T1) although the semi-diurnal tides were less visible than in the current variations

(Fig. 4.4.2). In contrast to the current variations, the temperature variations were in-phase for all five layers.

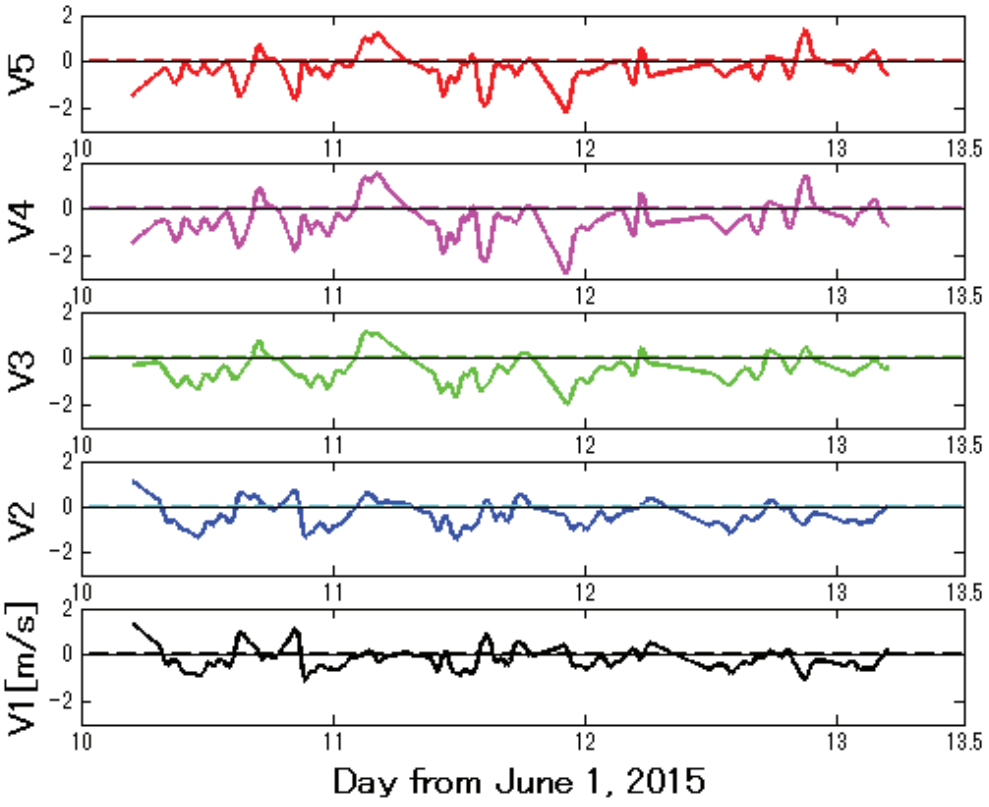


(a)

Fig. 4.4.1 Temporal variations of the five-layer hourly mean current reconstructed by the regularized inversion. Crests and troughs in the current variations are traced with vertical dotted lines at specific times. The horizontal dashed line close to zero current shows the inversion error for each layer.

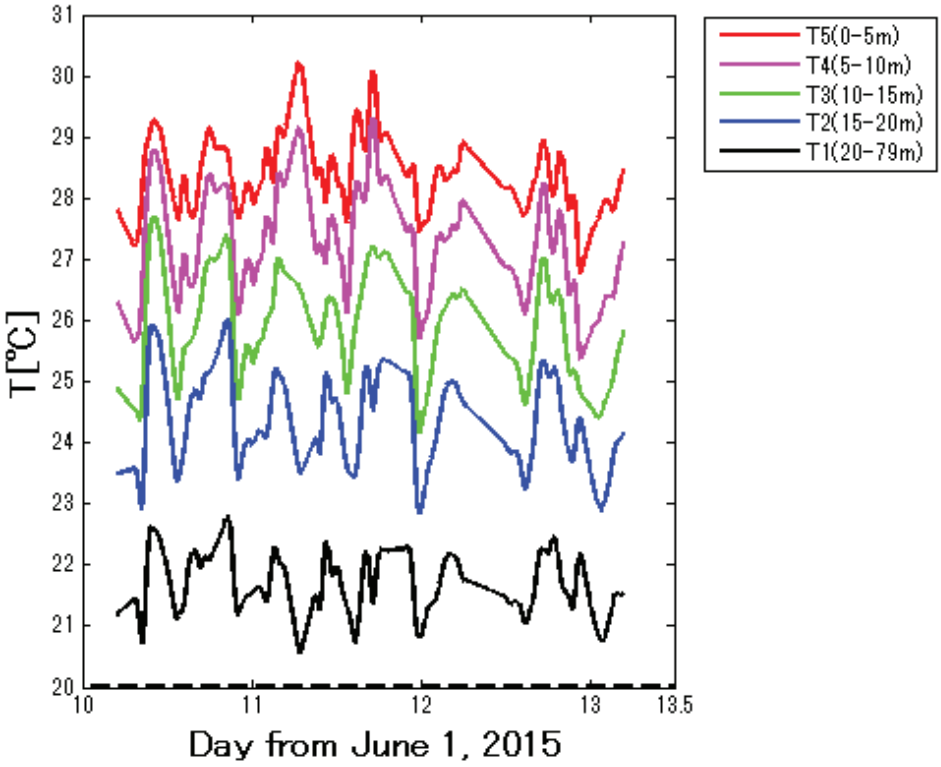


Fig. 4.4.2 Temporal variations of the hourly-mean temperature. Crests and troughs are traced by broken vertical lines at specific times. The horizontal dashed line close to the 22 ℃ line shows the inversion error for the first-layer temperature scaled with the offset from 22 ℃.

The temporal variations of the 2-day-mean current are shown in Fig. 4.4.3 together with those of the 2-day-mean temperature. The 2-day-mean current showed a strong vertical shear, which varied from -0.7 $ms^{-1}$ in the shallowest layer to -0.1 $ms^{-1}$ in the deepest layer. The 2-day-mean temperature remained nearly constant with time and showed strong thermal stratification, decreasing from 28.0 ℃ in the shallowest layer (T5) to 23.8 ℃ in the deepest layer (T1).

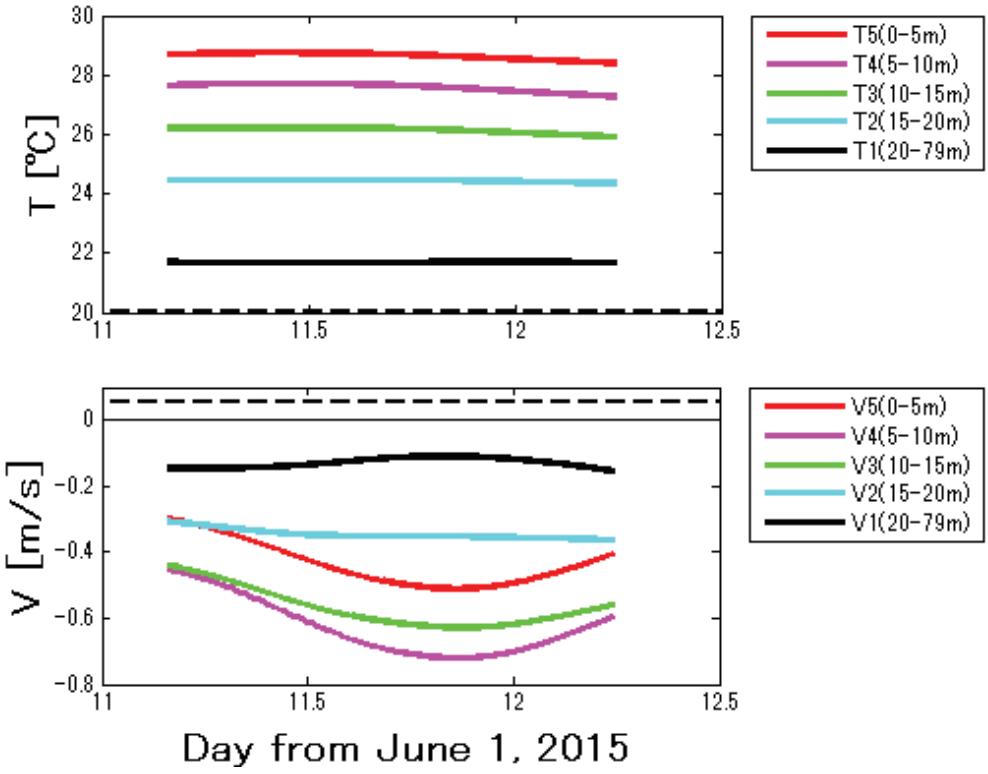


Fig. 4.4.3 Temporal variations of the 2-day-mean temperature (upper illustration) and current (lower illustration) for the five layers. The horizontal dashed lines show the inversion error for the deepest layer scaled with the offset from 20 ℃ for the temperature while no offset is used for the current.

Vertical profiles of the current and temperature, constructed from the all-data average (about one day) of the 2-day-mean data, are shown in Fig. (4.4.4) together with the CTD data obtained in 2014 and 2015. The 2015 temperature (blue line) was higher in the upper layer (0-20 m) and lower in the lower layer (< 20 m) than the 2014 temperature (black line). The averaged profile traced the CTD data in 2015 rather than the data in 2014. The average current varied from -0.6 $ms^{-1}$ in the shallowest layer to -0.1 $ms^{-1}$ in the deepest

layer.

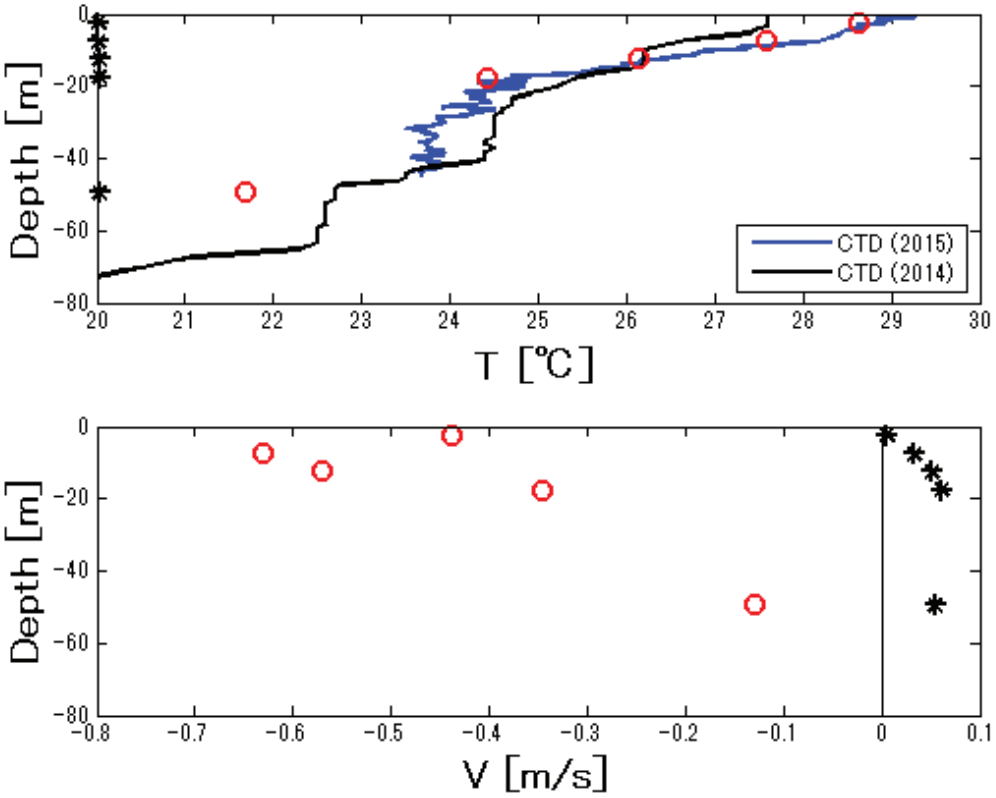


Fig. 4.4.4 Five-layer profiles of the (lower) all-data average current and (upper) temperature. The inverted temperature and current are shown with red circles in the upper and lower illustrations, respectively. The CTD data for 2014 and 2015 are shown with the black and blue lines, respectively. The asterisks (*) are the inversion error for the 2-day-mean data scaled with the offset from 20 ℃. The temperature errors are close to the zero line of 20 ℃ owing to the values smaller than 0.026 ℃.

### 4.4.2 Second experiment

Three kinds of path-average currents from POM simulation, CAT data (CAT) and data

assimilation (DA) are compared in Fig. 4.4.5 for the DA period from 15:00 on June 1 to 08:00 on June 3. The DA path-average current was largely separated from POM and close to CAT data, showing a pronounced effect of DA. Both path-average currents for CAT and DA were over 1.0 $ms^{-1}$ at the high tide around 06:00 on June 2. DA data were significantly deviated from CAT data in the period from 16:00 on June 2 to 02:00 on June 3, implying the generation of higher-frequency phenomena (see the upper panel of Fig. 4.4.6).

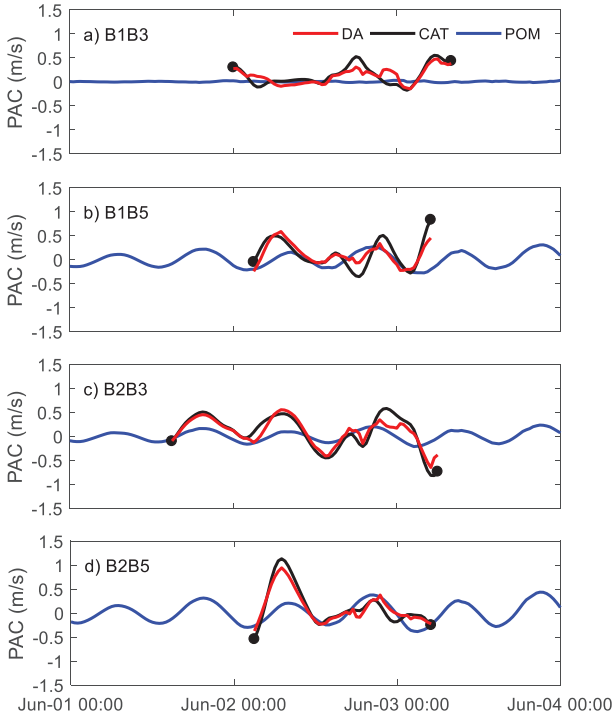


Fig. 4.4.5 Comparison of the path-average currents for DA (red lines), CAT (black lines) and POM (blue lines) along the four transmission lines. The start and end times of CAT data assimilation into POM are shown with the black dots for individual transmission lines.

In Fig. 4.4.6, the horizontal structures of DA current are shown with the vector plots at a bi-hourly interval from 03:00 on June 2 to 01:00 on June 3, focusing on tomography region. Northward currents were the strongest with about 2 $ms^{-1}$ at the high tide around 07:00 on June 2. However, no northward currents occurred at the next high tide around 19:00 on June 2. Instead a counter-clockwise vortex of size 3 km was generated in front of B1. On the other hand, southward currents around low tides were relatively weak at 03:00 and 15:00 on June 2. The counter-clockwise vortex generated at the low tide around 15:00 on June 2 was replaced by the clockwise vortex at the low tide around 01:00 on June 3. The vortex center was always placed at 1-2 km from B1.

The maximum northward volume transport across B1B3 was about 2.0 x $10^5$ $m^3s^{-1}$ at the high tide around 07:00 on June 2. The maximum southward volume transport occurred at the low tide around 03:00 on June 2 with half the maximum northward transportation. The volume transport at the next low tide around 01:00 on June 3 was reversed to the northward.

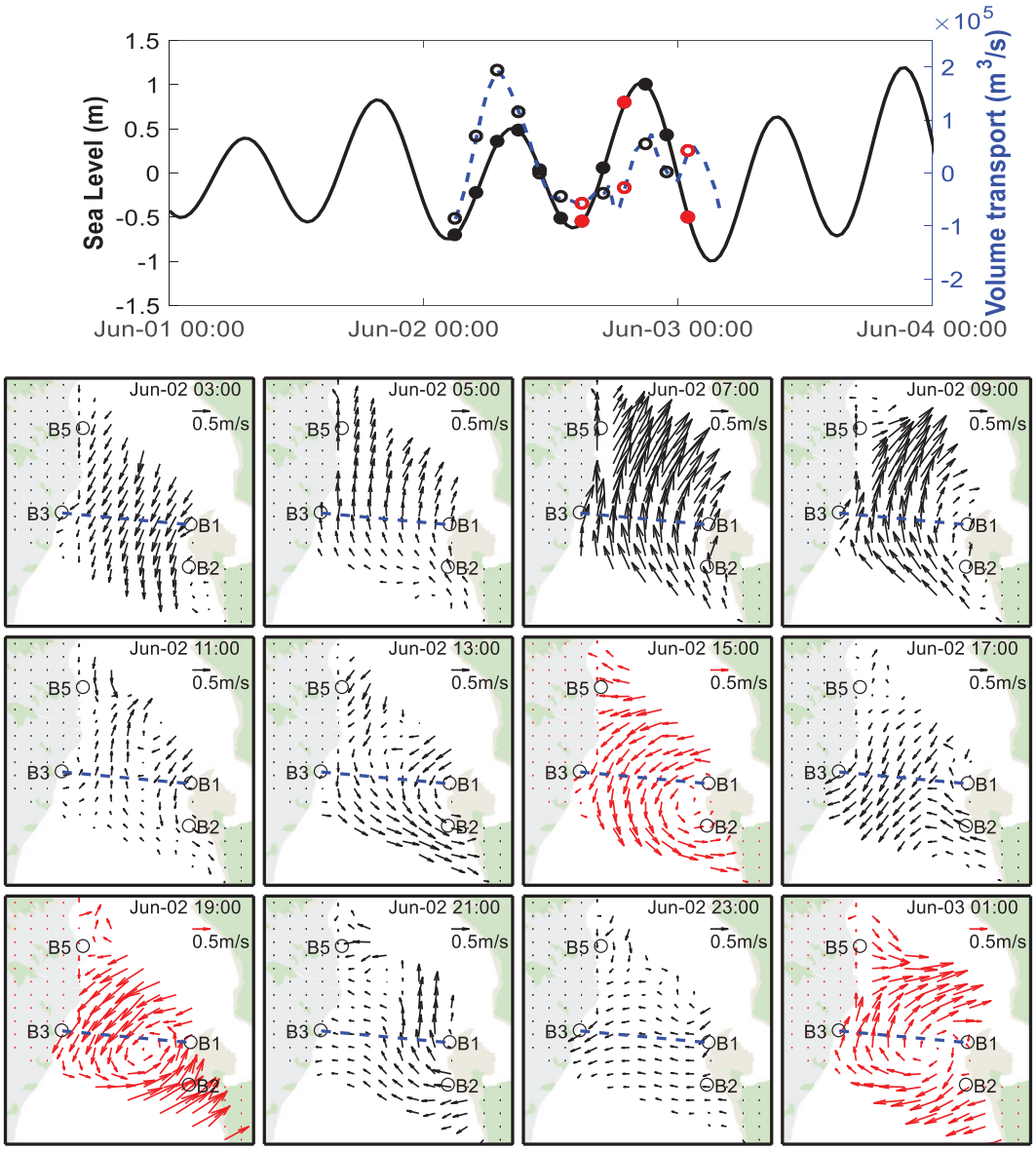


Fig. 4.4.6. Bi-hourly variations of the DA current fields from 03:00 on June 2 to 01:00 on June 3 for the four-line CAT data acquisition period. The temporal variation of sea level (black solid line) is also shown at the top of the figure with volume transport (blue dashed line) across B1B3 (blue dashed line in lower panel). Dots with the same color on the sea level curve are placed at times corresponding to the bi-hourly current fields. The same policy for time and dots is taken on volume transport curve. A scale of 0.5 $ms^{-1}$ is provided

at the top-right corner of each figure.

### 4.5 Summary and discussion

In the first experiment, tidal currents were measured at a 3-min interval by reciprocal sound transmission between two acoustic stations located on opposite sides of the Bali Strait. The SNR of the noisy received data was markedly improved by taking a 30-min sum of the 3-min-interval original data. The 30-min data were further improved by taking a moving average over 1 h.

The 5-layer structures in a vertical slice along the sound transmission line were reconstructed by the regularized inversion of the travel time data for 2 rays. The received data were severely disturbed by nonlinear internal tides with frequencies higher than the semi-diurnal tide, which were superimposed on semi-diurnal internal tides that varied with amplitude ranges of 1.0-1.5 $ms^{-1}$ for the current and 1.0-1.5 ℃ for the temperature [Robinson and Lee, 1994]**.** The nonlinear internal tides may be generated by a nonlinear interaction between the semi-diurnal internal tides and the irregular bottom topography [Gerkema and Zimmerman, 1995; Helfrich and Grimshaw, 2010]. Further study is required to elucidate the generation mechanism.

The 2-day-mean current showed a strong vertical shear, varying from -0.7 $ms^{-1}$ in the upper layer to -0.1 $ms^{-1}$ in the lower layer. The 2-day-mean temperature remained nearly constant with time and showed strong thermal stratification, decreasing from 28.0 ℃ in

the shallowest layer to 23.8 ℃ in the deepest layer. The vertical profile of the temperature, obtained through the all-data average of the 2-day-mean data, traced the 2015 CTD data better than the 2014 data. The vertical profile of the current varied from -0.6 $ms^{-1}$ in the shallowest layer to -0.1 $ms^{-1}$ in the deepest layer. The five-layer current and temperature significantly exceeded the inversion errors.

It is likely that the positive and negative path-average currents along the transmission line B2B3 correspond roughly to the northward and southward currents, respectively, because the shoreline has a north-south orientation. The north-south conversion of range-averaged (layered) currents implies that currents in the north-south direction reached speeds of about $1.5/\cos 63^{\circ} = 3$ [$ms^{-1}$] for θ= 63°at the maximum phase of the internal tide.

In the second experiment, four acoustic stations (B1, B2, B3 and B5) were successfully operated, enabling the mapping of current fields by data assimilation for 03:00 on June 2 to 05:00 on June 3. The accuracy of DA current was validated in comparison with the CAT data along the four transmission lines, producing RMSEs of 0.08 $ms^{-1}$ for B1B3, 0.16 $ms^{-1}$ for B1B5, 0.11 $ms^{-1}$ for B2B3 and 0.12 $ms^{-1}$ for B2B5.

Tidal waves coming from the Indian Ocean and passing through the Bali Strait are likely to be a progressive-wave type with maximum current at high tide and maximum southward current at low tide. The northward currents at the high tide around 07:00 on June 2 were the strongest with about 2 $ms^{-1}$. However, no northward currents occurred at the next high tide around 19:00 on June 2. When compared with the northward current,

the southward currents were weak at the low tides around 03:00 and 15:00 on June 2. At the high tide around 19:00 on June 2, a counter-clockwise vortex of size 3 km was generated in front of B1 instead of the strong northward current. The counter-clockwise vortex generated at the low tide around 15:00 on June 2 was replaced by the clockwise vortex at the low tide around 01:00 on June 3. The vortex center was always placed at 1-2 km from B1. Further studies are required for elucidating the dynamics of vortex generation.

The maximum northward volume transport across B1B3 was about 2.0 x $10^5$ $m^3s^{-1}$ at the high tide around 07:00 on June 2. The maximum southward volume transport occurred at the low tide around 02:00 on June 2 with half the maximum northward transportation. The volume transport at the next low tide around 01:00 on June 3 was reversed to the southward.

It is proposed that land-based CAT system provides a novel method of measuring the spatiotemporal structure of tidal current fields with higher-frequency phenomena.

**Acknowledgements**

This study was supported by funding from Hiroshima University. It was also supported by the National Program on Global Change and Air-Sea Interaction (GASI-IPOVAI-01-02) and the National Natural Science Foundation of China (grant numbers 41276095, 41476020, 41576001, and 41321004).

**References**

Adityawarman, Y., Kaneko, A., Taniguchi, N., Mutsuda, H., Komai, K., Guo, X. and Gohda, N. (2012). Tidal current measurement in the Kurushima Strait by the reciprocal sound transmission method, Acoust. Sci. and Technol., 33, 45-51.

Gerkema, T. and Zimmerman, J. T. F. (1995). Generation of nonlinear internal tides and solitary waves, J. Phys. Oceanogr., 25, 1081-1094.

Helfrich, K. R. and Grimshaw, H. J. (2010). Nonlinear disintegration of the internal tide, Ame. Meteorol. Soc., Journals Online, doi: http://dx.doi.org/10.1175/2007JPO3826.1.

MacKenzie, K. V. (1981). Nine-term equation for sound speed in the ocean, J. Acoust. Soc. Am., 70, 807-812.

Munk, W., Worceser, P. F. and Wunsch, C. (1995). Ocean acoustic tomography, 433pp, Cambridge Univ. Press, Cambridge.

Park, J. H., and Kaneko, A. (2000). Assimilation of coastal acoustic tomography data into a barotropic ocean model, Geophys. Res. Lett., 27, 3373-3376.

Rajan, S. D., Lynch, J. F. and Frisk, G. V. (1987). Perturbative inversion methods for obtaining bottom geoacoustic parameters in shallow water, J. Acoust. Soc. Am., 82, 998-1017.

Robinson, A. R. and Lee, D. (1994). Oceanography and Acoustics (AIP Press, New York).

Send, U., Worcester, P., Cornuelle, B., Tiemann, C. and Baschek, B. (2002). Integral measurement of mass transport and heat content in the Strait of Gibraltar from acoustic

transmissions, Deep-Sea Res. Part II, 49, 4069-4095, doi:10.1016/S0967-0645(02)00143-1.

Taniguchi, N., Huang, C.-F., Kaneko, A., Howe, B. M., Wang, Y.-H., Yang, Y., Lin, J., Zhu, X.-H. and Gohda, N. (2013). Measuring the Kuroshio Current with ocean acoustic tomography, J. Acoust. Soc. Am., 134, Pt.2: 3272-3281.

Yamaguchi K., Lin, J., Kaneko, A., Yamamoto, T., Gohda, N., Nguyen, H.-Q. and Zheng, H. (2005). A continuous mapping of tidal current structures in the Kanmon Strait, J. Oceanogr., 61, 283-294.

Yamaoka H., Kaneko, A., Park, J.-H., Zheng, H., Gohda, N., Takano, T., Zhu, X.-H. and Takasugi, Y. (2002). Coastal acoustic tomography system and its field application, IEEE Journal of Oceanic Engineering, 27, 283-295.

Zhang, C.-Z., Kaneko, A., Zhu, X.-H. and Gohda, N. (2015). Tomographic mapping of a coastal upwelling and the associated diurnal internal tides in Hiroshima Bay, Japan, J. Geophys. Res., 120(6), doi:10.1002/2014JC010676, 4288-4305.

Zhang, C.-Z., Kaneko, A., Zhu, X.-H., Howe, B. M. and Gohda, N. (2016). Acoustic measurement of the net transport through the Seto Inland Sea, Acoust. Sci. & Tech., 32, 10-20.

Zheng, H., Gohda, N., Noguchi, H., Ito, T., Yamaoko, H., Tamura, T., Takasugi, Y. and Kaneko, A. (1997a). Reciprocal Sound Transmission Experiment for Current Measurement in the Seto Inland Sea, Japan, J. Oceanogr., 53, 117-127.

Zhu, X.-H., Kaneko, A., Wu, Q., Zhang, C.-Z., Taniguchi, N. and Gohda, N. (2013).

Mapping tidal current structures in Zhitouyang Bay, China, using coastal acoustic tomography, IEEE J. Oceanic Eng., 38(2), 285-296.

Zhu, X.-H., Zhu, Z.-N., Guo, X., Ma, Y.-L., Fan, X., Dong, M.-H. and Zheng, C.-Z. (2015). Measurement of tidal and residual currents and volume transport through the Qiongzhou Strait using coastal acoustic tomography, Cont. Shelf Res., 108, 65-75.

# CHAPTER Ⅴ FURTHER ADVANCEMENT OF THE SYSTEM

## 5.1 Introduction

Coastal acoustic tomography (CAT) is an application of ocean acoustic tomography (OAT) to shallow, coastal seas [Munk and Wunsch, 1979; The ocean tomography group, 1982; Munk, et al., 1995; Zheng, et al., 1997; Park and Kaneko, 2000; Yamaoka, et al., 2002; Zhang, et al.,2015]. Both the techniques use acoustic data to derive the spatial structures of current and sound speed. In OAT/CAT, travel-time data are generally stored in individual subsurface stations and data analyses are performed after the recovery of the subsurface systems. Shoreward transfer of subsurface CAT data can enable the monitoring of offshore environments from the shore and making the real-time prediction of offshore environmental changes possible.

CAT with mirror-transpond functionality (MCAT) is here proposed to monitor offshore subsurface environments from the shore, measuring both current and sound speed between instruments. MCAT is an extension of the mirror transponder (MT) techniques that has been used in seafloor geodetic centimeter-level positioning of triangular MT arrays. In this technique, the sound was transmitted to the near−bottom MT transponders (often a triangular array) from ship and the subsequent mirror reflection signal from the MT array is received on the ship [Asada and Yabuki, 2001; Asada and Ura, 2009]. The mirror reflection signal is simply the received signal re-transmitted after a fixed, known delay. Two-way travel time sums observed were converted to sound speeds for known

MT positions. However, no current velocities were measured because the two-way travel time sums were not separated into two one-way travel times. On the other hand, MCAT with sound transmission from all subsurface stations can measure reciprocal travel time between instruments and both current velocity and sound speed.

### 5. 2 MCAT System Design

MCAT is functioned to construct travel time sums through repeat mirror transmissions following regular transmission. The simplest MCAT system, is composed of one cable-connected-station (M1: calle a “land” station in the compact MCAT array that is mentioned later) and one offshore autonomous subsurface station (M2: called a “key” station in the compact MCAT array). During the starting regular-transmission phase, the travel time ($t_{21}$) of sound propagating from M2 to M1 is recorded at M1 using record start time determined from expected travel time. The travel times ($t_{12}$) in the opposite direction is recorded at M2 with a method similar to M1. From the recorded data, the first pair of reciprocal travel times $t_{12}$ and $t_{21}$ forms. Note that in the subscript for the travel times, the first and second numbers show the number of transmit and reception stations, respectively. During the first-mirror transmission phase, sound transmitted from M1 at the same timing as M2 is mirrored or reflected by M2 and then received at M1 forming the travel time sum $[t_{12} + t_{21}]$. The offshore-recorded travel time $t_{12}$ is calculated at M1 by subtracting $t_{21}$ from the travel time sum $[t_{12} + t_{21}]$. Note here that these travel-time sums are not separable values. As a result, the second pair of reciprocal travel times are constructed using data

obtained at the land station M1 alone and available for real-time use. At the key station M2, $t_{12}$ is obtained from the regular data and $t_{21}$ is calculated by subtracting $t_{12}$ from the first-mirror data [$t_{21}$ + $t_{12}$] at M2. As a result, the third pair of reciprocal travel times is constructed but this is not available for real-time use. At the second-mirror transmission phase, the fourth pair of reciprocal travel times are obtained at land station M1, using the second-mirror data. The $t_{21}$ is obtained from the regular transmission at M1, and $t_{12}$ are calculated by subtracting $2t_{21}$ from the second-mirror data [$t_{21}$+$t_{12}$+$t_{21}$] at M1. Not only path-average current, but also path-average sound speed can be calculated, using the reciprocal data. However, the former which requires more strict time accuracy is selected to confirm MCAT performance.

As a result, four kinds of path-average currents are calculated from the four pairs of reciprocal travel times. The repeat cycles of regular transmission and subsequent mirror transmission are illustrated in Fig. 5.2.1 with time proceeding downward. Here, sound transmission and reflection losses are not taken into consideration and only reciprocal travel times are targeted in this paper.

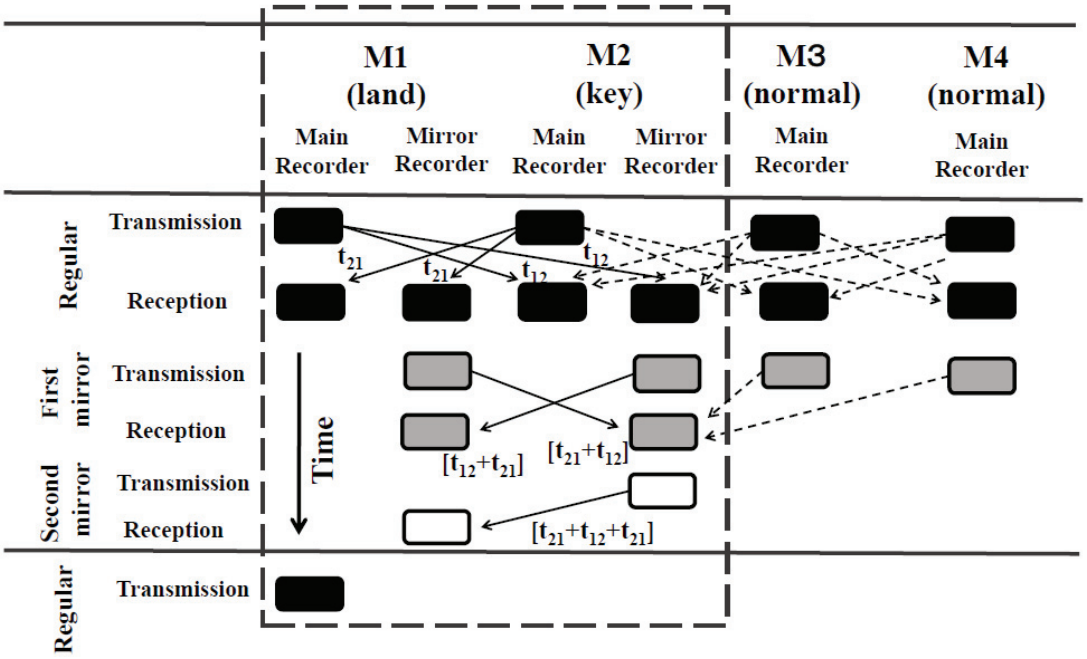


Fig. 5.2.1. Time chart showing regular transmission and subsequent mirror transmissions repeated among M1, M2, M3 and M4. Stations M1 and M2, operated in the feasibility experiments, are surrounded by thick rectangular lines. Slant arrows show the direction of sound transmission and the corresponding travel times and sums are put near the arrows.

Three travel-time sums $[t_{12}+t_{21}]$, $[t_{21}+t_{12}]$ and $[t_{21}+t_{12}+t_{21}]$ are non-separable parameters and valued with $[t_{12}+t_{21}]=t_{21}+t_{s1}$, $[t_{21}+t_{12}]=t_{12}+t_{s1}$ and $[t_{21}+t_{12}+t_{21}]=t_{21}+t_{s1}+t_{s2}$, respectively, where $t_{s1}/t_{s2}$ is the pre-determined record start time for regular/first mirror data in mirror recorder. Time chart for constructing travel-time sums between land (M1) and key (M2) stations is presented in Fig. 5.2.2.

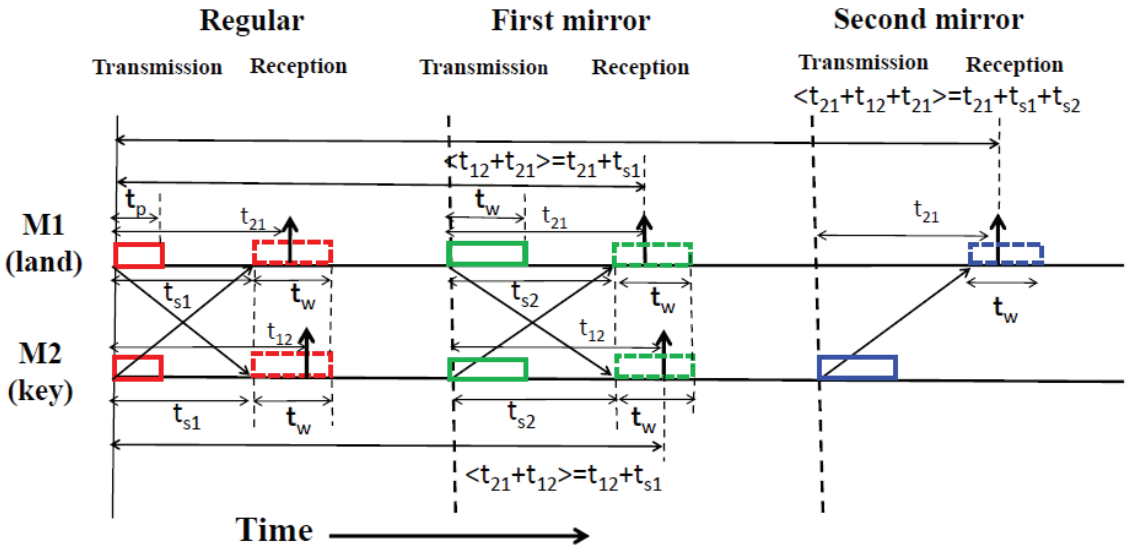


Fig. 5.2.2 Time chart for constructing travel-time sums between land (M1) and key (M2) stations. Solid and dashed rectangular boxes are transmit pulses and receiving windows, respectively. Slant arrows show the direction of sound transmission and begin at the start of acoustic pulses and end at the start of data recording. Thick vertical arrows show arrival peaks of signal coming from the counter station. The $t_{s1}$ and $t_{s2}$ are the start times of data recording for regular and first-mirror data, respectively.

CAT is enhanced here with mirror functionality to allow the transfer of subsurface environmental data shoreward from the offshore station. The environmental data is specifically a mirror image or duplicate of the acoustic signal received by a subsea CAT unit. Refer to the previous papers for the detailed CAT system design [Zheng, et al., 1997; Yamaoka, et al., 2002]. The block diagram of MCAT is presented in Fig. 5.2.3; portions associated with the new MCAT functionality are highlighted. The earlier internal micro−

computer SH7145F is replaced by SH7706 with main recorder to increase CPU speed and another SH7706 micro-computer is used as a mirror recorder to execute the mirror transmission following the regular transmission and reception. The 5-kHz sound modulated by the M sequence is transmitted from the broad-band transducer via D-Class Amp for both the regular and mirror transmissions. Received signals are amplified automatically up to a predetermined level by an amplifier with variable gains (VG-Amp) and then split into the regular and mirror circuits. The regular data are processed by the same circuit as CAT and stored into a 2GB micro SD memory card after 8-bit AD conversion. The mirror data are stored in the mirror recorder prior to the first mirror transmission. The first mirror transmission is done using data in the mirror recorder. The received first-mirror data are amplified by VG-Amp and then stored in both the main recorder of internal micro-computer and the mirror recorder after amplified by VG-Amp. Finally, the second-mirror transmission is done using the first-mirror transmission data in the mirror recorder. The received second-mirror data are amplified by VG-Amp and stored in the main recorder alone. Note that the second-mirror transmission is required to transfer the observation data to land station via key station as understood in the compact MCAT array, which is proposed later.

In all stations, a GPS receiver provides precise GPS clock signals. The subsurface station uses a chip-scale atomic clock (CSAC) and that is synchronized to GPS prior to system deployment. The offset of the CSAC is measured at system recovery with respect to GPS. The clock drift serves to correct CSAC clock during the subsurface observation.

On land, with a cable connected MCAT system, the operation is monitored by an external laptop PC via Bluetooth serial interface. The shore station is equipped with LAN modem for data telemetry to a remote site (e.g. the home office).

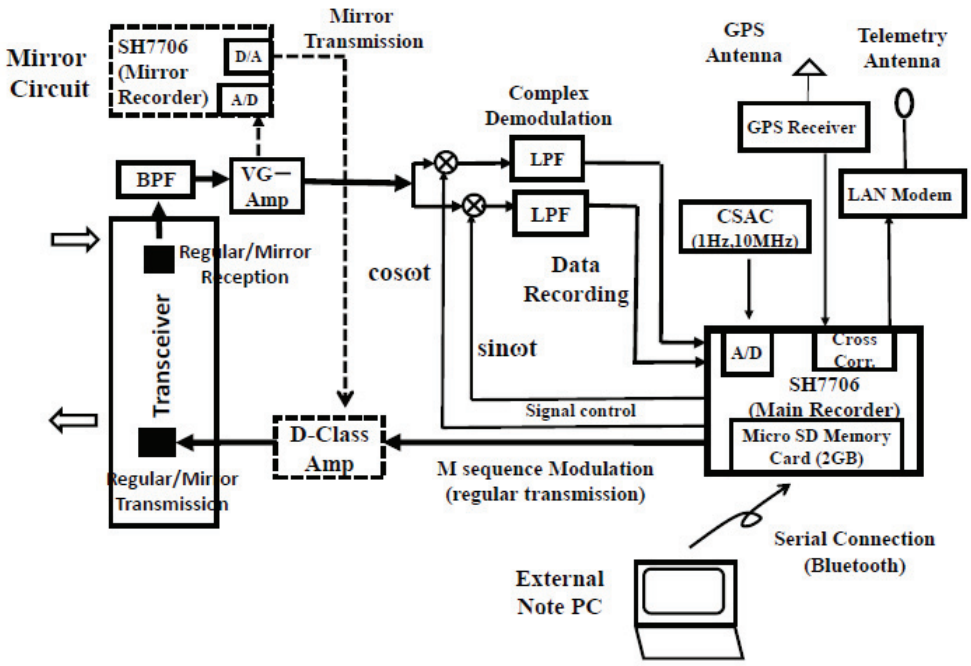


Fig. 5.2.3. Block diagram of MCAT. Portions equipped newly for mirror functionality are highlighted by dashed rectangles and arrows

### 5.3 Feasibility Experiments

Two feasibility experiments of MCAT were carried out during April 6-11, 2017 and June 22-24, 2017 in the Nekoseto Strait of the Seto Inland Sea, Japan. The first CAT experiment was carried out on March 2-3, 1999 [Park and Kaneko, 2000] at this same location, identifying the generation of vortex pairs. Two acoustic stations M1 and M2

were located on either side of the Strait with a separation of 5,246 m (Fig. 5.3.1). M1 is the land station with one mirror transmission and two mirror receptions and M2 is the key station with two mirror transmissions and one mirror reception (see Fig. 5.3.1). In the compact MCAT array described later, the key station is the offshore station, but note that it is located near the shore in the present feasibility experiment. At M1, system controller stored in the plastic container was put on the breakwater protecting a fishing port and only the transducer connected to the system controller by a cable was suspended into water in front of the breakwater by a rope and put with a 2-kg weight at 2m above the seafloor at depth 6 m (left in Fig. 5.3.2). At M2, all portions of the system stored in a 43-cm spherical glass were moored at 2 m above the seafloor at depth 6 m at the edge of the pontoon (right in Fig. 5.3.2). The seafloor deepens with a gentle slope reaching a maximum depth of 72 m at the distance of 3,000 m from M1, then rising linearly to M2. There is a 10-m bump on the seafloor at the distance of 1,000 m from M1.

The first Nekoseto experiment provided the first mirror data at both the land station M1 and key station M2, but the second-mirror data, expected at M1, were not acquired owing to the incompleteness of system operation program. After some improvement, second-mirror data were successfully obtained at M1 in the second Nekoseto experiment. However, there were no data at M2 owing to the recording error to the micro SD card. The voltage for system operation and sound transmission was 12.0 V for M1 and 13.2V for M2.

Five-kHz carrier signals modulated by one period (2.457 s) of the $12^{th}$ order M

sequence were transmitted simultaneously with different codes from the broad-band transducers (Neptune T170) placed at M1 and M2 at a 10-min interval for regular transmission. The first- and second-mirror transmissions were also done simultaneously from M1 and M2 at exactly 1-min and 2-min delays from the regular transmission, respectively, considering time elapsed in data recording. The cycle-per-digit value of modulated transmission signal (Q-value) was set to 3 so that one-digit length, the time resolution of multi-arrival rays, was 0.6 ms. The signal-to-noise ratio (SNR) of the received signals are increased by the processing gain of 36.1 dB by cross (replica)-correlation with the received signal with the M sequence used in the transmission. SNR is further improved by taking hourly-mean (six-ensemble average) of the 10-min interval data, focusing on semi-diurnal and diurnal tidal currents. A 2-day low pass filter (LPF) is adopted to retrieve tidal residual current from the hourly mean data.

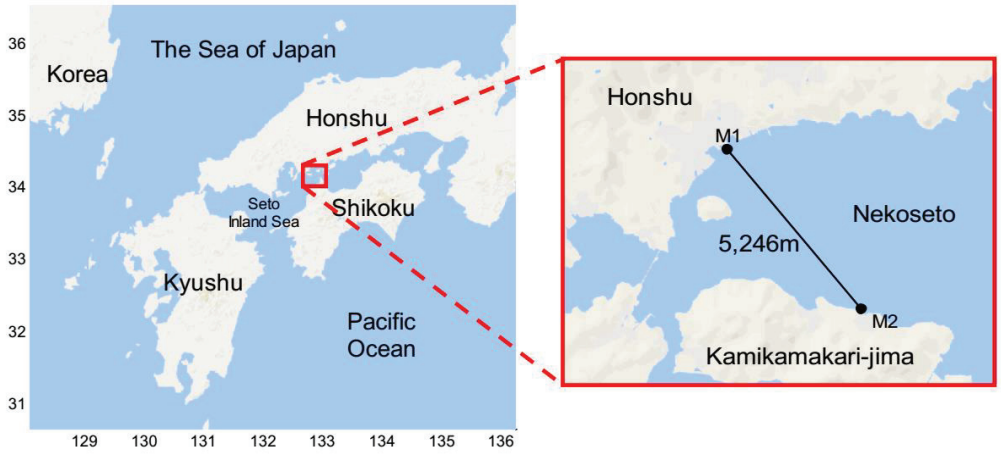


Fig.5.3.1. Location map of the feasibility experiments with a magnified scale at the right of the figure. M1 and M2 are the land and key stations, respectively, placed on both sides of the strait at a distance of 5,246 m.

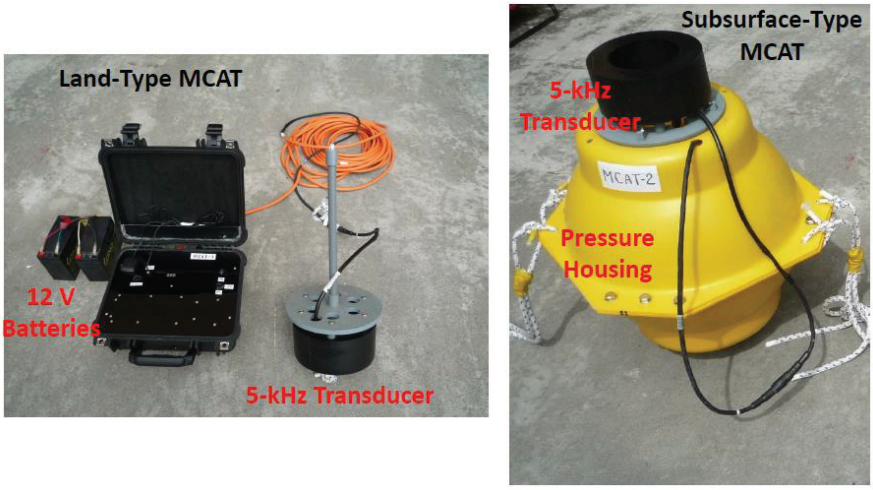


Fig. 5.3.2. Photo pictures of the land-type (left) and the subsurface-type (right) MCATs deployed at M1 and M2, respectively.

## 5.4 Methods

### 5.4.1 Ray simulation

Ray simulations were performed using a range independent reference sound speed profile, calculated from the CTD data on April 4, 2017, provided by the Hiroshima Prefecture Technology Research Institute (HPTRI). The bathymetric data were provided by the Japan Oceanographic Data Center (JODC). Simulated rays are shown in Fig. 5.4.1. Rays launched from source S with angles ranging from -10° to +10° with an increment of 0.2°, resulting in travel times between 3.511 s and 3.526 s. The reference sound-speed profile shows a surface duct, centered at depth 5 m, forming rays that concentrate in the upper 20 m. The three arrival rays propagating different depths are identified as rays with travel times of 3.5110 s, 3.5166 s and 3.5201 s. These travel times are well compared with

the observed ones described later.

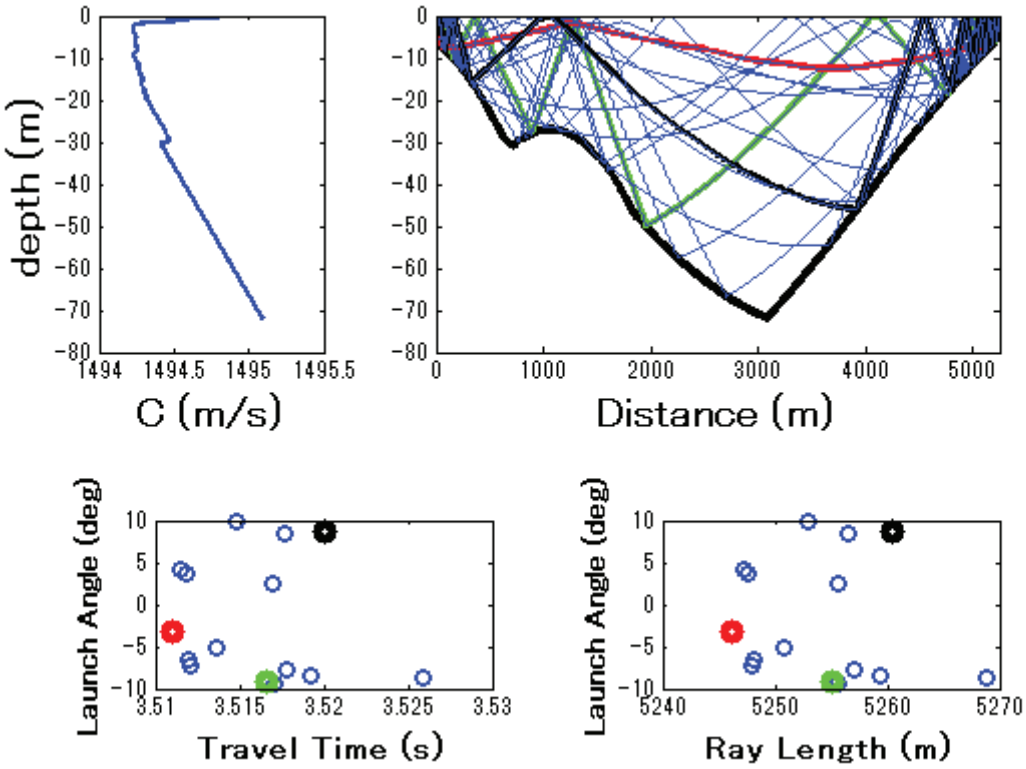


Fig. 5.4.1 Results of the range-independent ray simulation with (upper-right) ray pattern and (upper-left) reference sound speed. Rays corresponding to the first three observed arrival rays are colored with red, green and black. The travel times and ray lengths are indicated at the lower-left and lower-right of the figure, respectively. The red, green and black circles are data corresponding to the three arrival rays, respectively.

### 5.4.2 Arrival-Peak Identification

Correlation patterns for the regular and first-mirror data obtained at M1 and M2 in the first experiment are shown in Fig. 5.4.2 with the stack diagrams. The largest arrival peaks

were identified as peaks with SNR>10 in the correlation patterns. Noise level is determined, using data obtained in the range from the start time of receiving window to 5 ms before the expected travel time. SNR for the largest arrival peaks is defined as the ratio of the peak height to the noise level. There were a several arrival groups in the regular and mirror data. Ranges of the arrival groups spread wider in the mirror data than in the regular data, reflecting the two-way sound transmission (10,492 m in distance) due to mirror transmission. Travel times $t_{12}$ and $t_{21}$ for the first-mirror data obtained at M1 and M2 were converted to two-way travel-time sums, using $[t_{12}+t_{21}] = t_{12}+t_{s1}$ and $[t_{21}+t_{12}]=t_{21}+t_{s1}$, where $t_{s1}=3.116$ s.

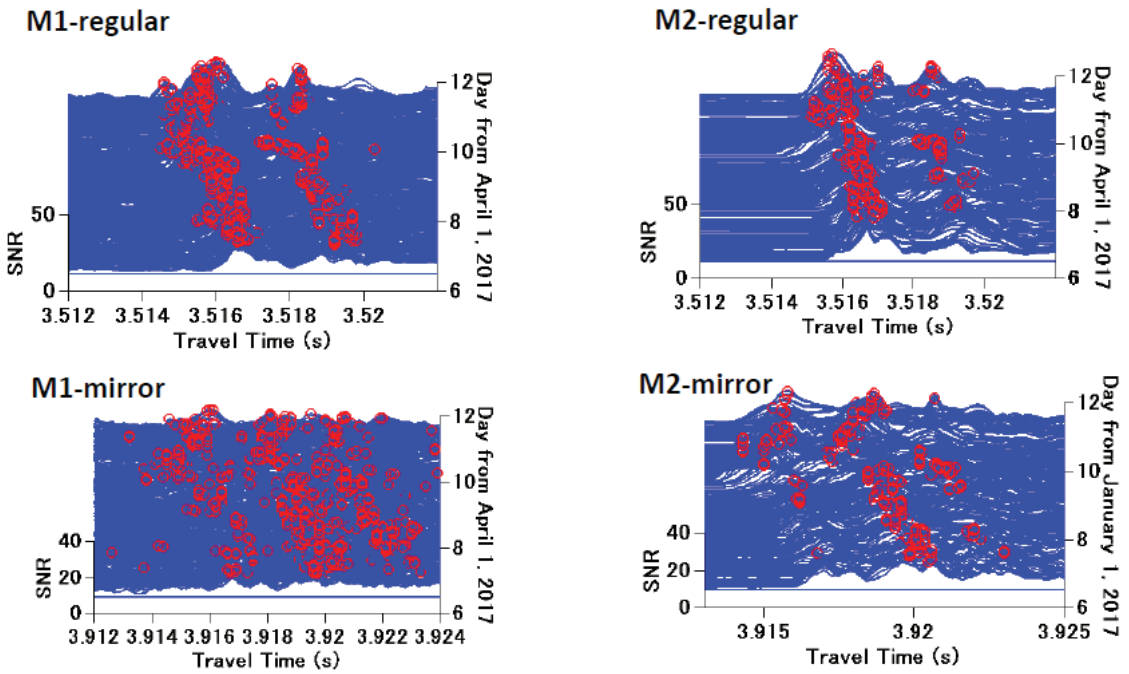


Fig. 5.4.2 Stack diagram of the correlation patterns for regular and mirror data obtained at M1 (left) and M2 (right). The red cicles indicate the largest arrival peaks with SNR>10 in the received data. Tme is proceeded upward. SNR is scaled for the vertical axis in the

3D plots.

The largest arival peaks scattered largely over the received period because multi-arrival groups existed in the first experiment as seen in Fig. 5.4.2. Thus, it was difficult to identify the largest arrival peak within each arrival group by the present method in which all received data are taken into consideration. A new method is here proposed to identify the first arrival peaks in the received data. The method consists of two steps. First, all received data are segmented into time spans of width 1.5 ms. The largest arrival peak with SNR >10 is determined in each time span and circled with different colors as shown in Fig. 5.4.3. When no arrival peak exists within a certain time span, the nearest arrival peak in the neighboring time spans is devised to cooperate the time span of non-arrival peaks with a color different from the corresponding time span. Different colors are assigned for the arrival peaks in individual time spans. Second, the assigned colors are rearranged, considering a smooth time-wise sequence of arrival peaks. Namely, the same color is assigned when arrival peaks in the next transmission time exist in the range of -0.75 ms to +0.75 ms before and after the peak position for the present transmission time. Finally, the first arrival peaks with smooth sequences are identified for three cases of regular, M1-mirror and M2-mirror (Fig. 5.4.4). This new method for multi-arrival-peak identification is adopted to the second experiment as well.

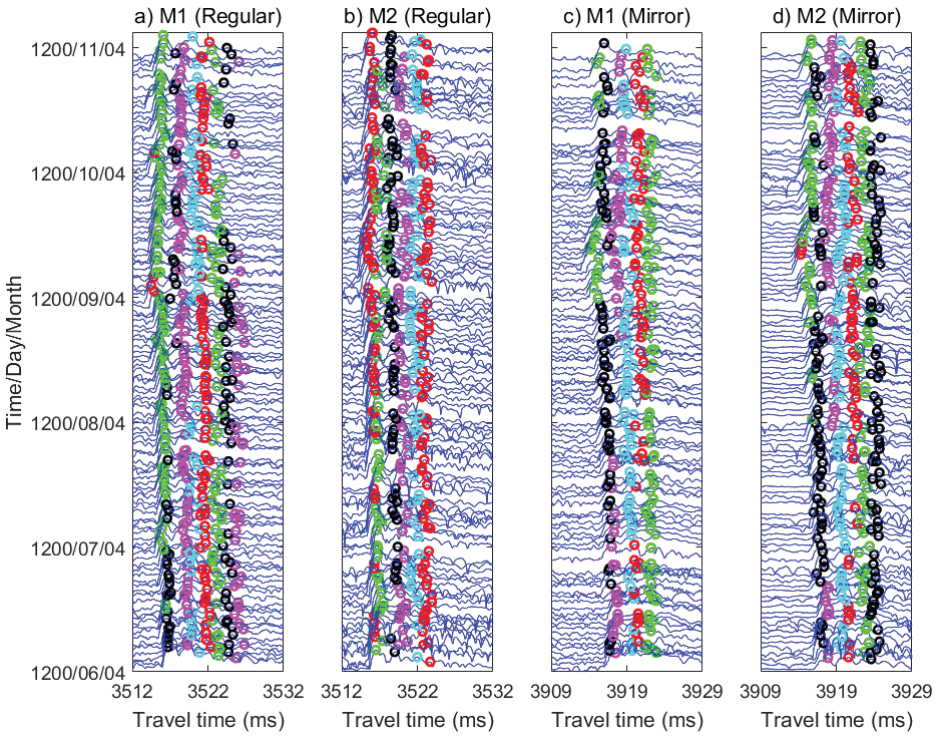


Fig. 5.4.3 Stack diagrams with the largest arrival peaks identified in each time span of width 1.5 ms. Different colors are assigned for individual time spans; a) M1-regular, b) M2-regular, c) M1-mirror and d) M2-mirror

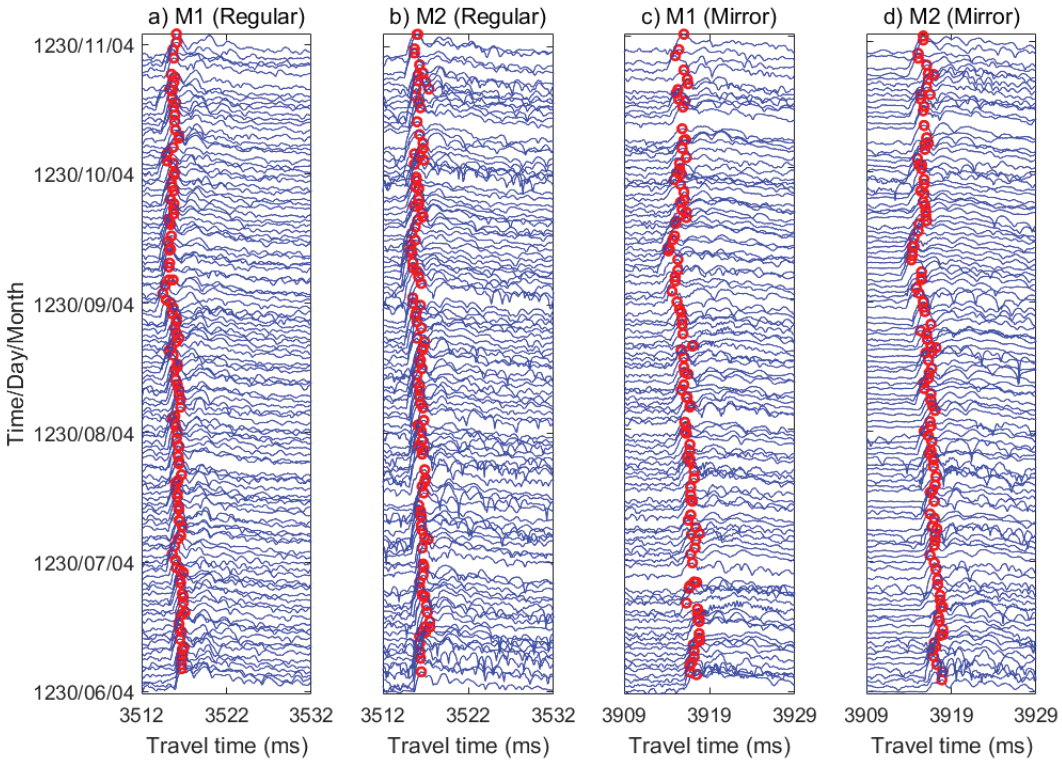


Fig. 5.4.4 Stack diagrams with the first arrival peaks identified by the new method. Red circles are assigned for the 1st peaks; a) M1-regular, b) M2-regular, c) M1-mirror and d) M2-mirror

For the second experiment, the first arrival peaks are identified for the regular, first mirror and second mirror data while the second mirror data are much noisy owing to the three-way sound transmission distance (15,738 m) (Fig. 5.4.5). Travel time $t_{21}$ for the second-mirror data obtained at M1 was converted to three-way travel-time sum, using $[t_{21}+t_{12}+t_{21}]=t_{21}+t_{s1}+t_{s2}$, where $t_{s1}=2.516$ s and $t_{s2}=4.457$ s.

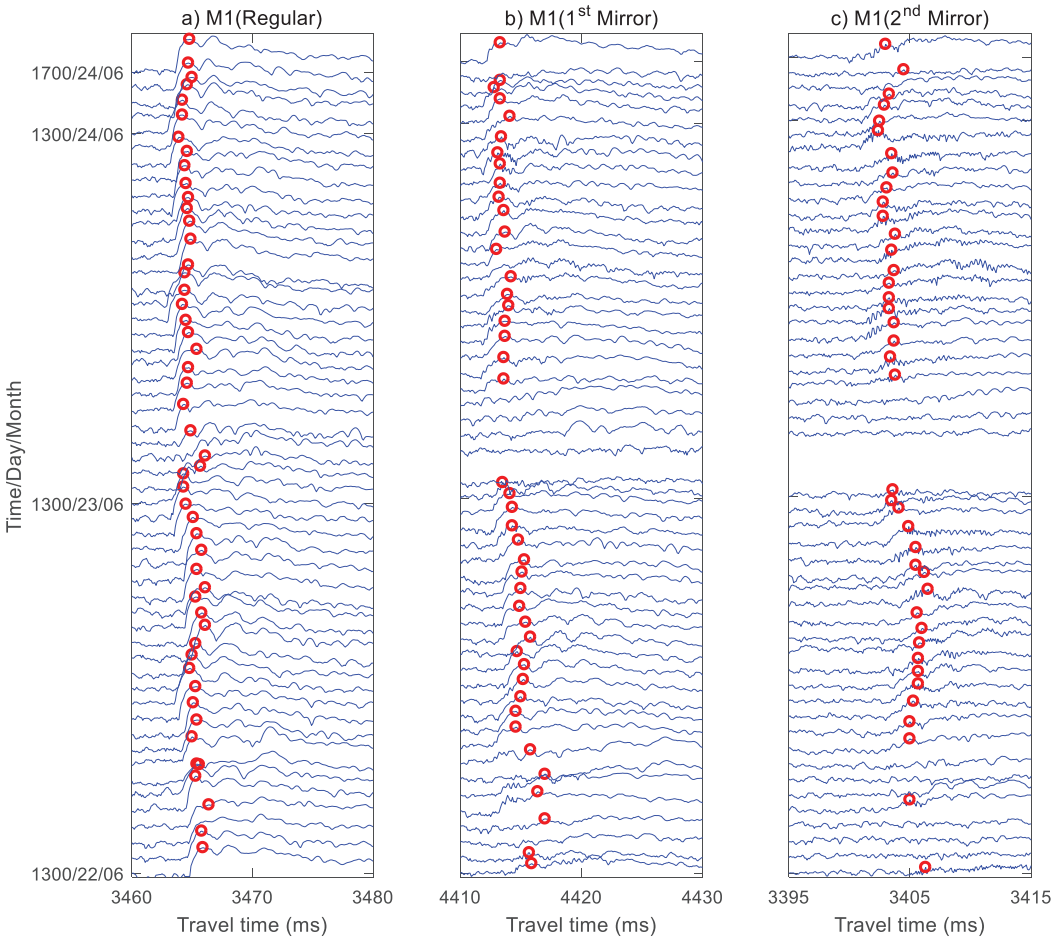


Fig. 5.4.5 Stack diagrams for the correlation pattern obtained at M1; the regular data (left), the first mirror data (middle) and the second mirror data (right). Red circles show the 1st arrival peaks.

## 5.5 Path-Average Currents

The first experiment data are described first here. Hourly-mean path-average currents calculated from the regular-regular data pair, M1 regular-first mirror data pair and M2 regular-first mirror data pair are compared in Figs. 5.5.1 for the 1st arrival peaks,

respectively. Temporal variations were dominated by semi-diurnal tides with amplitude (0.2-0.3) $ms^{-1}$ and accompanied by nonlinear tides with a spectral peak at several hours although spectral diagrams are not shown here. Curent magnitudes scattered significantly around the minimum current at the end of April 6 and the maximum current on April 8-10 while phases were in good agreement among the three data. Residual currents were significantly minus. Root mean squares errors (RMSEs) of the regular-mirror data pair with the regular-reguler data pair were 0.07 $ms^{-1}$ for both cases as shown in Table 5.5.1.

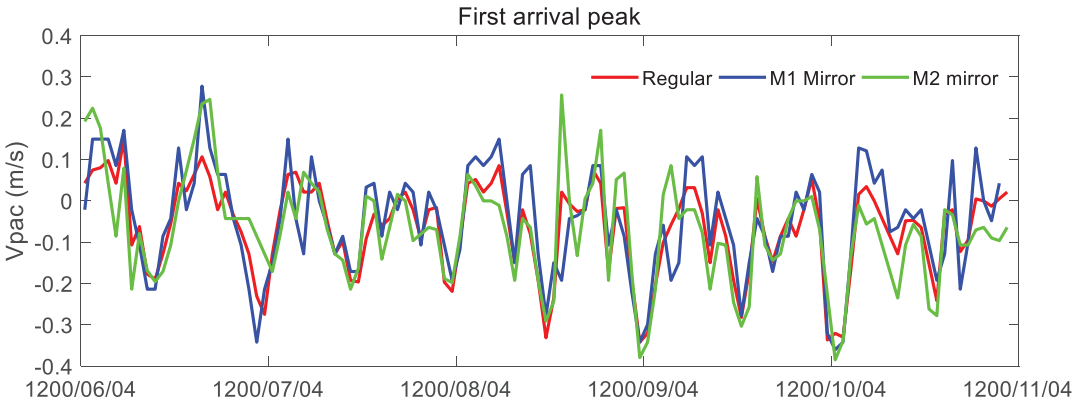


Fig. 5.5.1 Comparison of the hourly-mean currents, calculated from the regular-regular data pair (red), the M1 regular-mirror data pair (blue) and the M2 regular-mirror data pair (green) in the first experiment.

Two-day low pass filtered (LPF) currents are shown in Fig. 5.5.2 with the time plots. Three kinds of 2-day LPF currents varied slowly in the ranges of 0 to -0.1 $ms^{-1}$ . Mean of the 2-day LPF current currents were -0.08, -0.06 and -0.08 $ms^{-1}$ for the regular—regular data, M1 regular-first mirror data and M2 regular-first mirror data, respectively. RMSEs

were as small as 0.02 $ms^{-1}$ (Table 5.5.1).

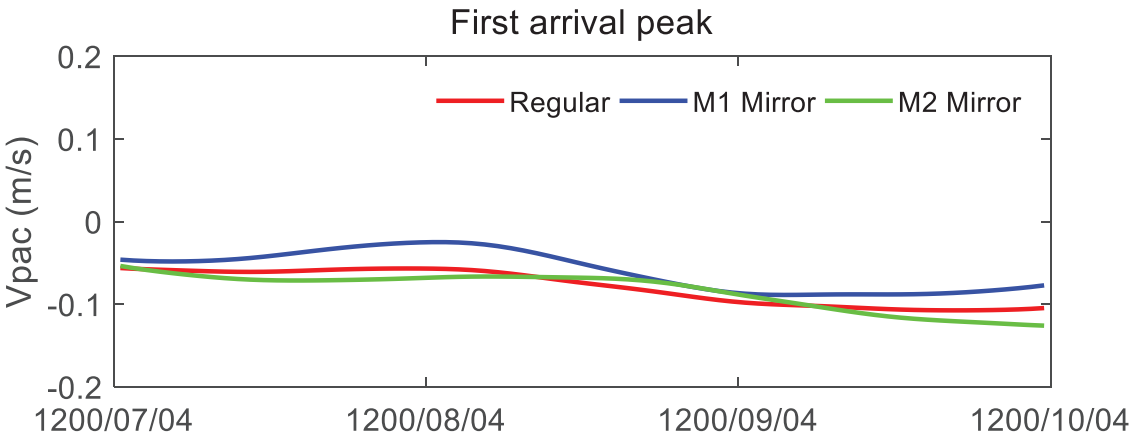


Fig. 5.5.2 Comparison of the 2-day LPF currents, calculated for the regular-regular data pair (red), N1 regular-first mirror data pair (blue) and N2 regular-first mirror data pair (green) in the first experiment.

Table 5.5.1 Root mean squares errors (RMSEs) for the first experiment and the 2-day mean current for the second experiment

| | First Experiment | | | Second Experiment | |
|---|---|---|---|---|---|
| | All-day mean of 2-day LPF current ($ms^{-1}$) | RMSE ($ms^{-1}$) | | | |
| | | Hourly mean | 2-day LPF | 2-day mean current ($ms^{-1}$) | |
| Regular-M1 mirror | -0.06 | 0.07 | 0.02 | Regular-1st mirror | -0.12 |
| Regular-M2 mirror | -0.08 | 0.07 | 0.02 | Regular-2nd mirror | -0.12 |

The second experiment data is described here. Hourly-mean path-average currents calculated from the regular-first mirror data pair and the regular-second mirror data pair for the first arrival peaks are shown in Figs. 5.5.3. Temporal variations of hourly-mean current were analogous to those in the first experiment. Two-day mean currents during 13:00 June 22 to 13:00 June 24 were calculated from the regular-first mirror data pair for the first three arrival peaks and the first arrival peak for the regular-second mirror data. The two-day mean currents, corresponding roughly to residual currents, were almost the same for both the cases with about -0.12 $ms^{-1}$ (Table 5.5.1).


Fig. 5.5.3 Comparison of the hourly-mean path-average currents calculated from the regular-first mirror data pair (left) and the regular-second mirror data pair (right).

## 5.6 Summary

To validate the performance of the newly developed MCAT systems, two feasibility experiments were carried out between land station (M1) and key station (M2) in the

Nekoseto Strait of the Seto Inland Sea, Japan. Various path-average currents along the sound transmission line, crossing the vortex-embedded tidal currents, were successfully calculated from the regular and mirror data. For the first experiment, the quality of first mirror data was significantly worse than that of the regular data, owing to the 2-way sound-transmission distance (10,492 m). For the second experiment, the second mirror data became further worse, owing to the 3-way sound-transmission distance (15,738 m). In the first and second experimental data, the hourly-mean path-average currents were dominated by semi-diurnal tides that oscillated with amplitude (0.2-0.3) $ms^{-1}$.

RMSEs for two different path-average currents provided indices of observation error. In the first experiment with the first mirror data alone, errors were evaluated in comparison of the first mirror data with the regular data. RMSEs of the hourly-mean regular-mirror current with the regular-regular current were 0.07 $ms^{-1}$ for the $1^{st}$ arrival peak. Errors derived from RMSEs for the $1^{st}$ arrival peak were significantly smaller than the hourly-mean currents. RMSEs for 2-day LPF current reduced to 0.02 $ms^{-1}$ for the $1^{st}$ arrival peak. In the second experiment with the first and second mirror data, two-day mean currents for the first arrival peak in the regular-first mirror data pair were nearly equal to -0.12 $ms^{-1}$ the same as 2-day mean current from the regular-second mirror data pair for the $1^{st}$ peak, implying accurate measurement for 2-day mean current.

The overall performance of compact MCAT array was roughly validated in the feasibility experiments although normal stations were not included in this study. Further study is required to improve the quality of mirror data by optimizing mirror functions

such as amplification gains and AD conversion rates.

**Acknowledgements**

The Hiroshima Prefecture Technology Research Institute (HPTRI) and the Japan Oceanographic Data Center (JODC) are acknowledged for providing the CTD data and the bottom topography data, respectively. This study has been supported by the United States Office of Naval Research-Global (ONR-Global/NICOP Grant N62909-15-1-N055), the National Natural Science Foundation of China (41776107, 41606113, 41476020, 41576001, 41621064), and the National Program on Global Change and Air-Sea Interaction (GASI-IPOVAI-01-02).

**References**

Asada, A. and Ura, T. (2009). Navigation system using seafloor geodetic mirror transponders and full-swath mapping system with synthetic aperture and triangle-arrayed interferometry techniques for autonomous underwater vehicle, Proc. CD-ROM of Oceans'09 Biloxi.

Asada, A. and Yabuki, T. (2001). Centimeter-level positioning on the seafloor, Proc. the Japan Academy, vol. 77, Ser. B, pp. 7-12.

Munk, W., Worceser, P. F. and Wunsch, C. (1995). Ocean acoustic tomography, 433pp,

Cambridge Univ. Press, Cambridge.

Munk, W. and Wunsch, C. (1979). Ocean acoustic tomography: a scheme for large scale monitoring, Deep-Sea Res., 26A, 123-161.

Ocean Tomography Group. (1982). A demonstration of ocean acoustic tomography, Nature, 299, 121-125.

Park, J. H., and Kaneko, A. (2000). Assimilation of coastal acoustic tomography data into a barotropic ocean model, Geophys. Res. Lett., 27, 3373-3376.

Yamaoka H., Kaneko, A., Park, J.-H., Zheng, H., Gohda, N., Takano, T., Zhu, X.-H. and Takasugi, Y. (2002). Coastal acoustic tomography system and its field application, IEEE Journal of Oceanic Engineering, 27, 283-295.

Zhang, C.-Z., Kaneko, A., Zhu, X.-H. and Gohda, N. (2015). Tomographic mapping of a coastal upwelling and the associated diurnal internal tides in Hiroshima Bay, Japan, J. Geophys. Res., 120(6), doi:10.1002/2014JC010676, 4288-4305.

Zheng, H., Gohda, N., Noguchi, H., Ito, T., Yamaoko, H., Tamura, T., Takasugi, Y. and Kaneko, A. (1997a). Reciprocal Sound Transmission Experiment for Current Measurement in the Seto Inland Sea, Japan, J. Oceanogr., 53, 117-127.

# CHAPTER Ⅵ FORTHCOMING ISSUES

## 6.1 High-frequency Phenomena in the Bali Strait

Further investigation is presented for higher-frequencies phenomena occurring in the Bali Strait in association with semidiurnal tides.

For the first experiment, the time plots (upper panel) and the power spectral density diagram (lower panel) of the path-average current V23 along B2B3, processed by 6-hour HPF are shown in Fig. 6.1.1. Current dominated by semi-diurnal wave packets (envelopes) was beaten by oscillation of period 3-4 hours. The crest of the envelope occurred at 18:00 on 10 June, at 14:00 on 11 June and 18:00 on 12 June. A narrow wave packet also existed around 03:00 on 12 June. The largest amplitude of the envelope was about 0.8 $ms^{-1}$ and corresponded roughly to the mean tides (see the sea level data in Fig. 6.1.1). The oscillation of 3-4 hours period immersed in the envelope and visible in the spectral diagrams may be higher-frequency phenomena which occur at strong current around the mean tides, implying a standing-wave type.

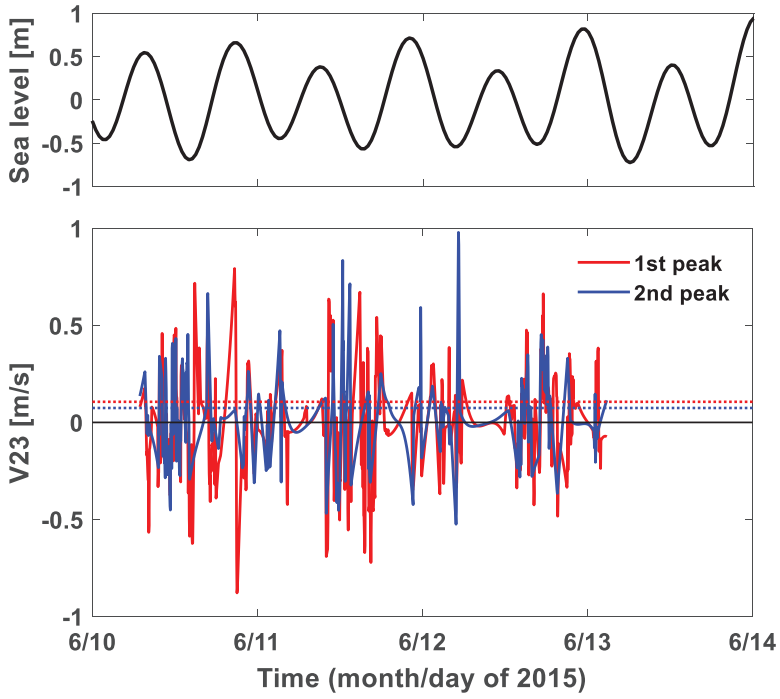


(a) Time plots

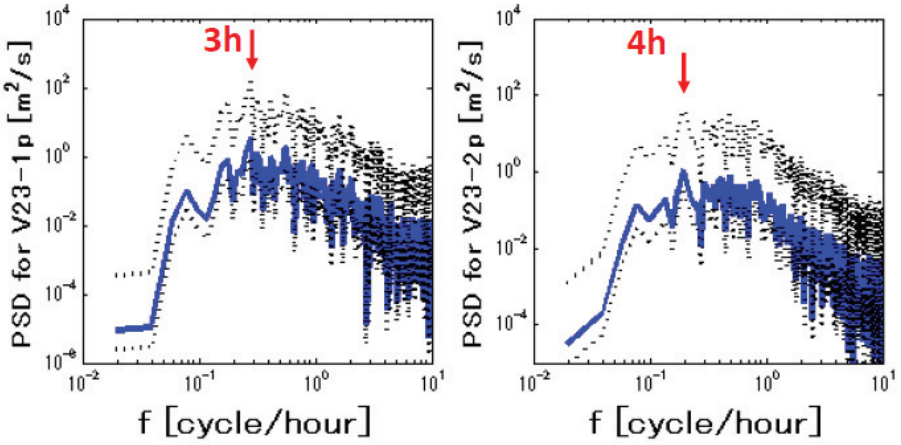


(b) Power spectral density diagrams

Fig. 6.1.1 (a) time plots and (b) power spectral density diagrams for the path-average current V23 along B2B3, processed by 6-h HPF. In the upper figures, the red and blue broken lines are the solution uncertainty for 1st and 2nd peaks. In the lower figure, the largest spectral peaks are pointed out by the red downward arrows. The broken lines show

the 95% confidence limit.

The second experiment data also showed the generation of 3-hour oscillation with amplitudes larger than 0.5 $ms^{-1}$ in the 6-h LPF current, mainly composed of semi-diurnal. It is likely that resonated phenomena occurred because energy levels are higher in the 3-hour oscillation than in the semi-diurnal tides. The amplitudes of 3-h oscillation were large especially at the mean tide on 2 June, implying the same phenomenon of a standing-wave type as found in the first experiment.

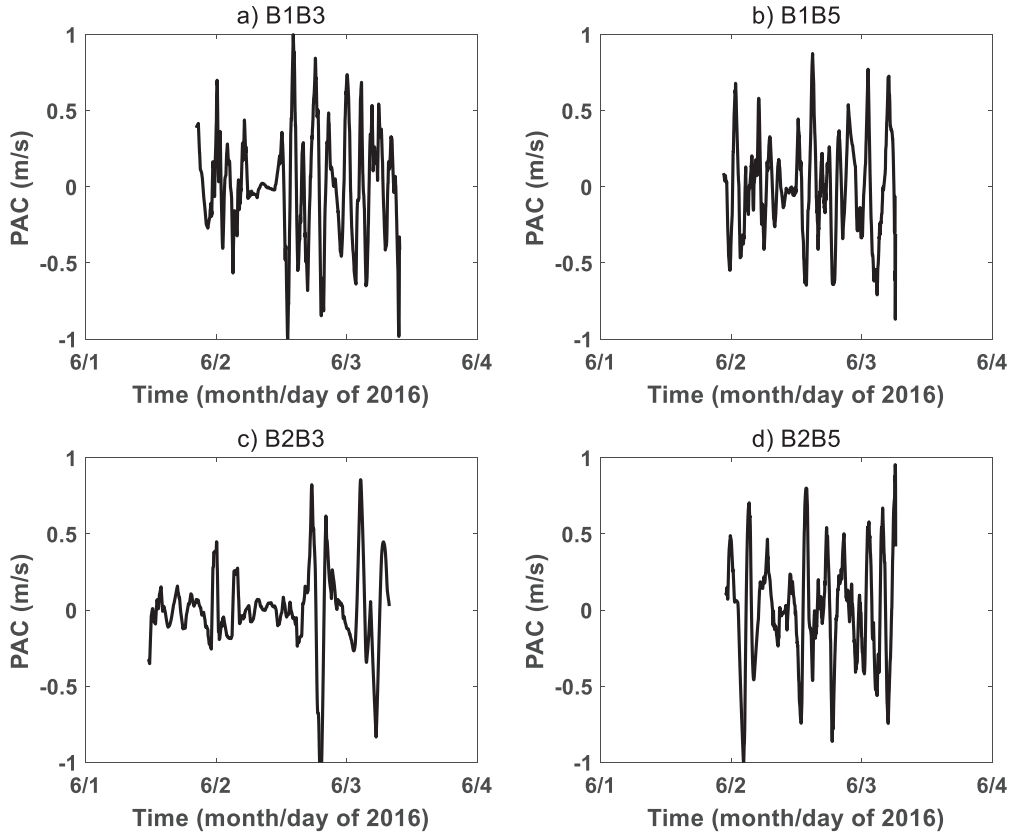


(a) Time plots

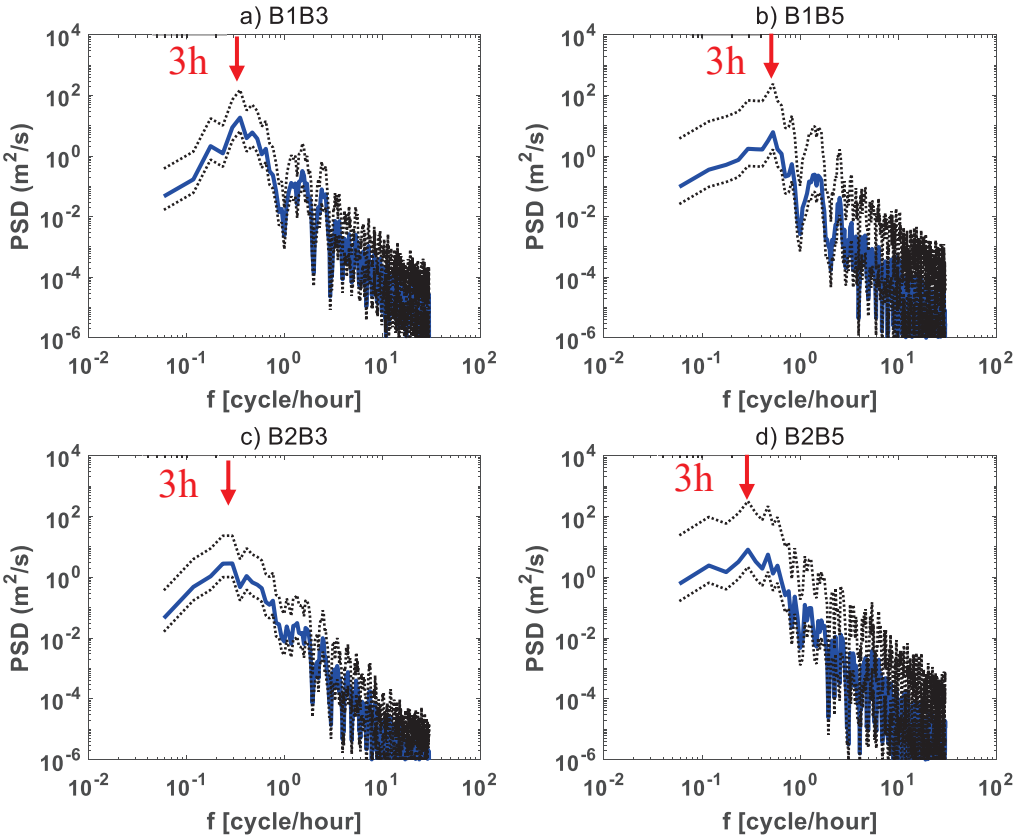


(b) Power spectral density diagrams

Fig. 6.1.2 (a) time plots (upper) and (b) power spectral density diagrams for the path-average currents V13, V15, V23 and V25, processed by 6-h high pass filter. In the lower figure, the largest spectral peaks are pointed out by the red downward arrows. The broken lines show the 95% confidence limit.

## 6.2 Compact MCAT Array for Field Deployment

Compact MCAT array which means a minimum set necessary for realtime current measurement from the shore in field deployment is composed of one-land (M1), one-key (M2) and two-normal stations (M3 and M4) as sketched in Fig. 6.2.1. The key and normal

stations are subsurface types. Between two subsequent regular transmissions, all stations execute regular-mirror transmission and reception as scheduled in Table 6.2.1. There are two advantages in the compact MCAT array. Observation data may be stored safely in all subsurface stations even when acoustic connection between the land (M1) and key (M2) stations fails. Conversely, all data are already transferred to land station (M1) when the recovery of subsurface stations fails.

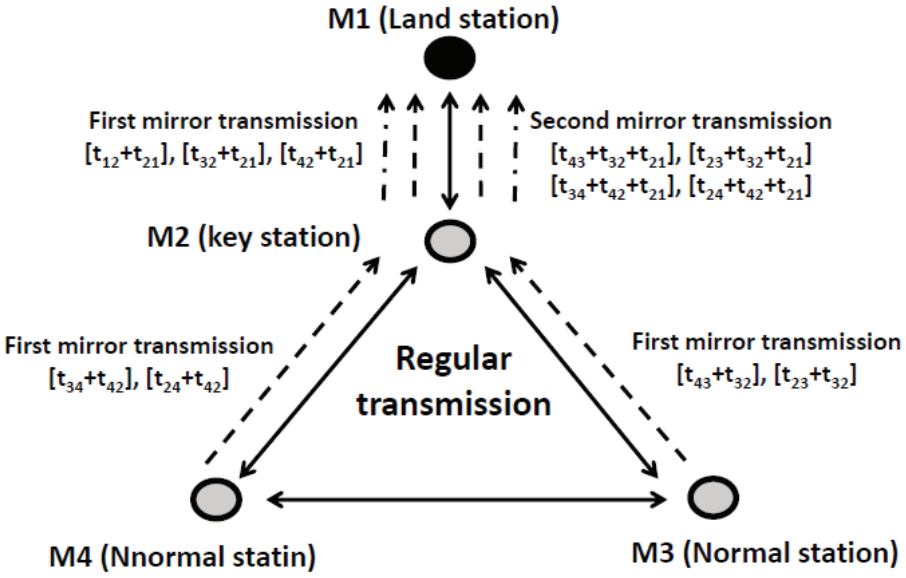


Fig. 6.2.1 Compact MCAT array in field deployment composed of one land station (M1), one key station (M2) and two normal stations (M3 and M4).

Table 6.2.1 Functionality of land, key and normal stations in MCAT compact array

| station | Regular | | First Mirror | | Second Mirror | |
|---|---|---|---|---|---|---|
| | transmission | reception | transmission | reception | transmission | reception |
| Land | ○ | ○ | ○ | ○ | × | ○ |
| Key | ○ | ○ | ○ | ○ | ○ | × |
| Normal | ○ | ○ | ○ | ○ | × | × |

All regular transmission data received at M1, M3 and M4 gather at M2 through the first－mirror transmissions and then transferred to M1 through the second-mirror transmission. Finally, M1 receives the three travel time sums $[t_{12}+t_{21}]$, $[t_{32}+t_{21}]$ and $[t_{42}+t_{21}]$ by first-mirror transmission from M2 and the four travel time sums $[t_{23}+t_{32}+t_{21}]$, $[t_{24}+t_{42}+t_{21}]$, $[t_{34}+t_{42}+t_{21}]$ and $[t_{43}+t_{32}+t_{21}]$ by second-mirror transmission from M2. Furthermore, one regular-transmission data from M2 is received at M1 with travel time $t_{21}$. Three one-way travel times $t_{12}$, $t_{32}$ and $t_{42}$ are calculated by subtracting $t_{21}$ from the three first-mirror data $[t_{12}+t_{21}]$, $[t_{32}+t_{21}]$ and $[t_{42}+t_{21}]$ received at M1. The four one-way travel times $t_{23}$, $t_{24}$, $t_{34}$ and $t_{43}$ are calculated by subtracting the first-mirror data $[t_{32}+t_{21}]$ and $[t_{42}+t_{21}]$ from the second-mirror data $[t_{23}+t_{32}+t_{21}]$, $[t_{24}+t_{42}+t_{21}]$, $[t_{34}+t_{42}+t_{21}]$ and $[t_{43}+t_{32}+t_{21}]$ received at M1. Finally, all the raw received data obtained at M1 are transferred to the data center via telemetry. Then, path-average current and sound speed (mainly temperature) along the four transmission lines M1M2, M2M3, M3M4 and M4M1 are calculated in realtime by correlation calculation in data center, using only raw received

data obtained at M1.

Compact MCAT array with potential ability of monitoring deep-sea subsurface environments in realtime from the shore is sketched in Fig. 6.2.2. All subsurface systems (M2, M3 and M4) composed of controller, transducer and battery packs are moored at the sound channel axis or near the seafloor for floor depths shallower than the axis. The realtime data gather at land-station M1 on the shore via key station M2 and are transferred to data center via telemetry. It is expected that compact MCAT array can contribute to the world climate change research through the monitoring of the Indonesian Through Flow (ITF) when it is deployed systematically in deep Indonesian straits.

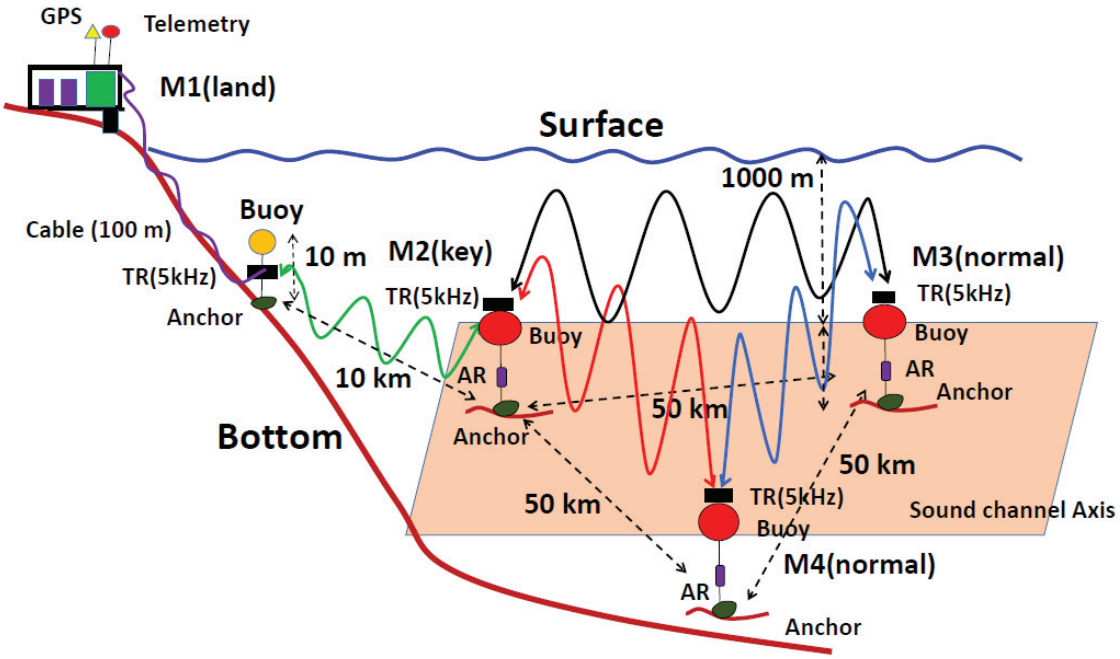


Fig. 6.2.2 Compact MCAT array applicable to deep Indonesian straits where ITF passes through.

# CHAPTER Ⅶ Conclusions

Major results are here summarized for each from chapter 2 to 6.

In chapter 2, a time-efficient data assimilation scheme based on Ensemble Kalman filter was newly proposed. In this method, model error covariance is determined from the perturbed model state vectors at each DA time without forecasting the ensemble model state vectors using a N-ensemble of pseudorandom noises. The sub-vectors of pseudorandom noises have a zero mean and adjustable variance. Furthermore, their covariance is determined from the decorrelation length. A smooth correlation function is also introduced to model error covariance to localize the data assimilation effect on tomography domain. Barotropic and baroclinic assimilation are specified based on the two-layer information sampled from CAT 2-peak data. The data assimilation equations for current and salinity are formulated using travel time difference and travel time summation. The vertical-slice inversion utilizing regularization method is formulated in the final section of the chapter together with solution uncertainty and inversion error.

In chapter 3, the newly proposed method was applied to assimilate the 2013 Hiroshima Bay CAT data into POM. The target was to map the coastal upwelling, generated along the northern shore of Hiroshima Bay by a northerly wind from a typhoon. The coastal upwelling was well structured in a two-layer system of current and salinity. The major results obtained in chapter 3 are summarized as follows:

(1) The 3D process of coastal upwelling and the associated reverse flow, generated in

the northern part of Hiroshima Bay, was well reconstructed by assimilating the barotropic and the baroclinic data from CAT. The upwelling was generated near the northern shore of Hiroshima Bay from 00:00 to 12:00 on September 17. During this period, a subtidal southward-flowing current formed in the upper layer and a northward-flowing current formed in the lower layer. The salinity in the upper layer increased up to values equal to the lower-layer salinity. As time proceeded, the upwelling was followed by a period of reverse flow with a northward subtidal current in the upper layer and a southward subtidal current in the lower layer. The upper-layer saline water gradually retreated northeastward with the northward subtidal current.

(2) During the upwelling, the total transported volume was balanced between the upper and lower layers, demonstrating this continuity of the upper- and lower-layer currents and the reliability of data assimilation. The total northward transported volume for the upper layer in the reverse-flow period was significantly smaller than the total southward transported volume for the upper layer in the upwelling period. Furthermore, the total northward transported volume for the upper layer was significantly larger than the total southward one for the lower layer in the reverse-flow period. These transported volume imbalances implied the existence of two types of water mixing: offshore mixing during the upwelling and nearshore mixing during the reverse-flow period. The mixing fractions, estimated from the volume imbalances were 24% for the offshore mixing and 30% for the nearshore mixing.

(3) The assimilation results were compared to CAT and CTD results. The average RMSEs

for the DA and CAT currents in the subtidal data were 0.018 $ms^{-1}$ and 0.014 $ms^{-1}$ for the SBR and SR rays, respectively. The average RMSEs for the hourly-mean salinity were 0.539 for the SBR rays and 0.455 for the SR rays. The depth-average salinity errors for the DA and CTD data were 0.680 for the upper layer and 0.881 for the lower layer. The DA errors were significantly smaller than the variation ranges of current and salinity associated with the upwelling.

In chapter 4, two CAT experiments were performed in 2015 and 2016 to study environmental variations in the Bali Strait. Vertical-slice inversion based on regularization method was applied to CAT data from the first experiment. CAT data from the second experiment were assimilated into POM to map the horizontal structure of current. The major results obtained in chapter 4 are summarize as follows:

(1) In the first experiment, the internal tides were measured at a 3-min interval by reciprocal sound transmission between B2 and B3, and 5-layer structures in a vertical slice along the sound transmission line were reconstructed by the regularized inversion of the travel time data for 2 rays. The hourly-mean current and temperature showed the generation of nonlinear internal tides with frequencies higher than semi-diurnal tides. The 2-day-mean current varied from -0.7 $ms^{-1}$ in the upper layer to -0.1 $ms^{-1}$ in the lower layer, showing a strong vertical shear. The 2-day-mean temperature remained nearly constant with time and showed strong thermal stratification, decreasing from 28.0 ℃ in the shallowest layer to 23.8 ℃ in the deepest layer. The vertical profile of the temperature,

obtained through the all-data average of the 2-day-mean data, traced the 2015 CTD data better than the 2014 data. The five-layer current and temperature significantly exceeded the inversion errors.

(2) In the second experiment, barotropic current in the Bali Strait was well assimilated with the 6-h LPF data rather than the hourly mean data. Strong northward currents which occurred with about 2 $ms^{-1}$ at the high tide around 07:00 on 2 June did not occur at the next high tide around 19:00 on 2 June and current fields were replaced by a counter-clockwise vortex of size 3 km in front of B1. On the other hand, southward currents around low tides were relatively weak at 03:00 and 15:00 on 2 June. The counter-clockwise vortex generated at the low tide around 15:00 on 2 June off B1 was replaced by the clockwise vortex at the low tide around 01:00 on 3 June. The maximum northward volume transport across B1B3 was about 2.0 x $10^5$ $m^3s^{-1}$ at the high tide around 07:00 on 2 June and half the maximum northward transportation at the low tide around 02:00 on 2 June. The volume transport at the next low tide around 01:00 on 3 June was reversed to the southward.

In chapter 5, the newly developed MCAT system was proposed was well validated by two feasibility experiments which were carried out in the Nekoseto Strait of the Seto Inland Sea. Major results are summarized as follows:

(1) The various path-average currents along the sound transmission line, crossing the vortex-embedded tidal currents, were successfully calculated from the regular and mirror

data. The hourly-mean path-average currents obtained from mirror and regular data, were dominated by semi-diurnal tides which have amplitude of 0.2-0.3 $ms^{-1}$ in both two experiments.

(2) The indices of observation error were estimated using RMSEs for two kinds of path-average current. In first experiment, RMSEs of the hourly-mean regular-mirror current with the regular-regular current were 0.07 $ms^{-1}$ for the 1$^{st}$ arrival peak. Errors derived from RMSEs for the 1$^{st}$ arrival peak were significantly smaller than the hourly-mean currents. RMSEs for 2-day LPF current reduced to 0.02 $ms^{-1}$ for the 1$^{st}$ arrival peak. In the second experiment with the first and second mirror data, 2-day mean currents for the first arrival peak in the regular-first mirror data pair were nearly equal to -0.12 $ms^{-1}$ the same as two-day mean current from the regular-second mirror data pair for the 1$^{st}$ peak, implying accurate measurement for 2-day mean current.

In chapter 6, further consideration on Bali Strait study and MCAT field deployment design is provided. The major results obtained here are summarized as follows:

(1) High-frequency phenomena occurring in the Bali Strait were studied, focusing on current variations in the range of 1 to 6 hours. Oscillation of periods 3-4 hours with semi-diurnal envelopes was found in both the time plots and power spectral density diagrams. The maximum of the envelope corresponded to the mean tides, implying the generation of standing-wave type phenomena.

(2) Compact MCAT array composed of one-land (M1), one-key (M2) and two-normal

stations (M3 and M4) is proposed as a minimum set necessary for realtime offshore current measurement from the shore in field deployment. It is concluded that the MCAT compact array proposed here finds a place as a new technology to transfer shoreward subsurface tomography data obtained with offshore stations.

## Acknowledgements

I would like to express my gratitude to my thesis advisor, Prof. Arata Kaneko. This study was carried out under the overall guidance of Prof. Kaneko. I am very grateful to him for providing me the opportunity to study in Hiroshima University, for his patient guidance and continuous encouragement during my thesis works. His proficiency in oceanography, editorial and field experiment were critical to complete this dissertation and has taught me valuable experiences and insights on the working of academic research. I am also grateful to his kindest support for my living and study in this beautiful city.

Special thanks are directed to Dr. Noriaki Gohda for his great support to MCAT system development and the feasibility experiments.

I wish to express my deepest appreciation to my master-course supervisor, Associate Professor Ju Lin in the Ocean University of China, for giving me helpful advices in data assimilation study. I also appreciate Dr. Zhang for helping me settle down when I first came here and giving me kind support in Hiroshima Bay study.

My sincere appreciation is provided to the rest of my thesis committee members, Profs. Yasuhiro Doi, Hironori Yasukawa and Hidemi Mutsuda for careful reading of this dissertation and providing valuable comments that improved greatly the presentation and quality of this dissertation.

My thanks are provided to Dr. Fadli Syamsudim and his staffs in BPPT for giving tremendous support in Bali Strait experiments.

Last, but no least, I would like to thank my fiancée, Min Liu for taking care of my living in Japan and let me focus on my PhD study. I especially owe much to my parents, my brother for their long-term support and dedication. Without them, this work cannot be completed.